The Dissertation Committee for Zizhuo Zhang Certifies that this is the approved version of the following Dissertation:

Area-Selective Deposition of Ferromagnetic Cobalt Films

Committee:

John G. Ekerdt, Supervisor

Gyeong S. Hwang

Nathaniel Lynd

Edward T. Yu

Area-Selective Deposition of Ferromagnetic Cobalt Films

by

Zizhuo Zhang

Dissertation

Presented to the Faculty of the Graduate School of

The University of Texas at Austin

in Partial Fulfillment

of the Requirements

for the Degree of

Doctor of Philosophy

The University of Texas at Austin

August 2018

Dedication

To my beloved family

Acknowledgements

With five years of my life doing PhD study at Ekerdt group at the University of Texas at Austin, I have not only learned how to do scientific research, but also known how to be a better man. It is the most unique five year I have experienced. I will never forget all the fun with my friends and my colleagues here, and all the difficulties that make me strong. I want to say thanks to all the people helping me through the journey.

Firstly, I want to express my most sincere gratitude to my advisor Dr. John G. Ekerdt. Without his continuous encouragement and support, I can hardly complete my PhD study. I made very slow progress in research during my first two years, but he never criticized me and questioned my efforts. Instead, he helped me find solutions or resources to solve problems every time. His jokes make every group meeting enjoyable. Although he is very busy as both a professor and the associate dean of engineering college, he always replies my emails very soon and sets up a meeting even at his lunch time when I want to discuss something with him. He tries to meet my every reasonable request, giving me opportunities to present work at conferences, giving me vacation to visit my families and friends in China, giving me highly-rated recommendations to internship and job opportunities, etc. I would like to give my best wishes to Dr. Ekerdt and his families.

Besides, I want to express my special thanks to my committee members, Dr. Gyeong S. Hwang, Dr. Edward T. Yu, Dr. Nathaniel Lynd, for their guidelines and suggestions on my research. I also want to say thanks to my collaborators, Dr. Steve

Sirard at Lam Research, Tanmoy Pramanik at Banerjee group, Austin Lane at Wilson group, Meghali Chopra at Bonnecaze group, for their support on my work. With a research focus on metal film deposition and characterization, I learned lots of knowledge about etching, electrical device, polymer and modelling from them.

In addition, I want to say thanks to my colleagues. Sonali Chopra, who acts like my mentor, helped me start my research project. Wen Liao, who recruited me into the group, treated me with her delicious desserts at every party. Himmi Nallan, a genius on tools, helped me solve many difficulties with equipment building and repairing. I would also like to thank Joe M. McCrate, Tyler Elko-Hansen, Thong Ngo, Brad Leonhardt, Edward Lin, Bryce Edmondson, Brennan M. Coffey, Pei-Yu Chen, Di Li and Xin Yang for their help with my daily lab work and suggestions on my research.

Moreover, I want to say thanks to my dear friends, Shen Hu, Li Ji, and Ye Yuan. There are countless favors they did for me and fun they brought to me. Without them, my PhD life cannot be so colorful.

Additionally, I want to say thanks to the Department of Chemical Engineering at UT-Austin. Without the valuable opportunity the department offers me, I cannot come here, learning new knowledge, meeting interesting people, and experiencing different cultures. I also want to thank the NASCENT center for giving me a good platform to find collaborations and meet talented researchers.

Finally, I want to express my gratitude to my families. Although they are not here with me, they give me encouragement and courage to overcome all the difficulties. In particular, I want to express my special thanks to my girlfriend, Songjing Yan. Long-

distance relationship is so hard, but she seldom complains. The everyday care from her on cellphone and the monthly reunions with her are the biggest encouragement to me. I would like to accompany her at the rest of my life to repay her patience, support and love through the five years.

Abstract

Area-Selective Deposition of Ferromagnetic Cobalt Films

Zizhuo Zhang, Ph.D.

The University of Texas at Austin, 2018

Supervisor: John G. Ekerdt

Cobalt is a classic ferromagnetic material and finds applications in magnetic random access memory devices. As an emerging patterning technique, area-selective atomic layer deposition (AS-ALD) of cobalt films has the advantages of low cost and low film damage compared with the current patterning approach of photolithography followed by etching of cobalt films. This research explores the routes to realize the AS-ALD of ferromagnetic cobalt films.

Carbon-free Co films have been deposited on MgO(001) and SiO_2/Si substrates by low temperature thermal ALD of CoO and subsequent low temperature atomic deuterium reduction of CoO. While high temperature D_2 reduction of CoO results in rough and disconnected Co islands, low temperature D reduction of CoO produces smooth and continuous Co films. The Co films produced by low temperature D reduction exhibit a smaller coercivity than the Co films produced by high temperature D_2 reduction.

Reduction conditions affect the microstructure and the magnetic properties of the reduced Co films. The process-structure-property relationship has been elucidated. The

increase of reduction temperature, partial pressure of deuterium, and reaction time increases the average grain size and coercivity of the reduced Co films. Co films that are grown on substrates with lower dewetting tendency, such as MgO and Al_2O_3, show smaller average grain size and smaller coercivity.

Polystyrene (PS) has been proposed to work as a passivation material to realize the AS-ALD of cobalt films. PS is effective in inhibiting the nucleation and film growth of CoO on oxide substrates. Micro-patterns and nano-patterns of CoO have been grown by AS-ALD through PS templates produced by photolithography and PS templates created by directed self-assembly of diblock copolymer, respectively. CoO patterns can be further reduced to form Co patterns without deformation.

Table of Contents

List of Tables

List of Figures

List of Illustrations

Chapter 1: Introduction

1.1 MOTIVATION

As device dimensions for integrated circuits approach the physical limits, it is increasingly difficult to improve the performance of current memory chip designs, including dynamic random access memory (DRAM), static random access memory (SRAM) and flash, by scaling-down.[1] This pushes the need for development of next generation memories, in which spin-transfer torque random access memory (STT-RAM) is considered as one of the most promising candidates.[2–4] STT-RAM is a magnetic memory utilizing spin-polarized current to write magnetic bits. It is non-volatile and can be scaled down below 10 nm. STT-RAM combines the high performance of DRAM and SRAM, and the low power consumption of flash. The most important part in a STT-RAM device is the magnetic tunnel junction (MTJ) stack where the spin transfer torque happens and where the data are stored, as shown in Figure 1.1a.[4–7] There are mainly two ultra-thin (2-3 nm) ferromagnetic layers isolated by a dielectric barrier layer (1-2 nm) in the stack. The film purity and film structure integrity of the stack affect the performance of the STT-RAM device and so the patterning of MTJ stack (including film deposition and feature sculpture) has attracted considerable attention.[8,9]

The different approaches to patterning are generally classified as either top-down or bottom-up.[10] Top-down approaches utilize lithography and subsequent etching steps to sculpt nanoscale features, while bottom-up approaches assemble nanostructures through the thermodynamic interactions between molecules. The current dominant technology for

patterning the MTJ stack is the top-down approach. After the film stack is deposited, lithography is utilized to define the pattern and then the pattern is transferred into the stack by etching. This approach has been extensively studied, but there are still several limitations with it. First, there is always feature loss associated the etching process, which results in poor control of the final stack nanoshape.[11] Figure 1.1b shows a MTJ stack patterned by lithography and etch, from which non-vertical sidewalls can be seen.[11] The etching process also causes potential physical or chemical damage to the film quality and structure integrity, and this degrades the device performance.[12] Additionally, both lithography and etching are very expensive and this leads to high production costs.[10] This research explores bottom-up process steps to enable feature fidelity retention.

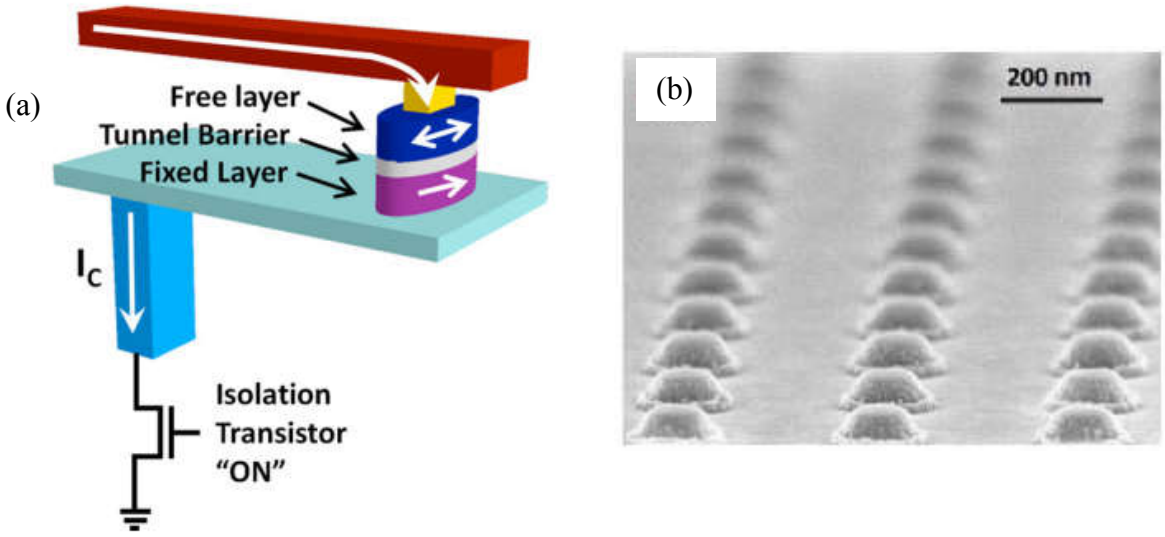

Figure 1.1. (a) Schematic of a MTJ memory cell.[4] (b) SEM image of a MTJ stack.[11]

1.2 BACKGROUND

1.2.1 Area-Selective Atomic Layer Deposition

As the critical dimension of electronics approaches sub-10 nm scales, current patterning techniques enabled by lithographic and etch processes are experiencing more and more challenges.[13–16] The development of advanced lithographic processes, such as extreme ultraviolet lithography, and advanced etch processes, such as multiple patterning, are progressing the further scale-down of chip.[17–22] A huge challenge with these advanced technologies is their high cost.[23] At the same time the development of alternate pattering techniques, such as bottom-up patterning, are drawing increased attention. Bottom-up patterning utilizes interactions between molecules to assemble nanostructures, which imparts the low-cost advantage.[24–26] A typical example of bottom-up patterning that is being explored extensively is area-selective deposition (ASD).[27–31] Based on the principle that film nucleation and growth only happen at reactive sites rather than inert sites, ASD employs specific surface chemistries to deposit material on desired regions of a substrate selectively.[32] The selectivity offers ASD the potential of self-alignment and the reduction of lithography and post-deposition etch steps.[28]

Atomic layer deposition (ALD) is a self-limiting chemical vapor phase deposition technique.[33] In a typical ALD cycle, precursor A is first introduced into the reactor to saturate the reactive sites on the surface. After excess precursor A is purged out, precursor B flows into the reactor and reacts with the reactive sites associated with chemisorbed precursor A on the surface. After purging out the byproducts and excess precursor B, up to one layer of the film is grown. The cycles are carried out until the

desired film thickness is achieved, as shown in Figure 1.2.[34] Due to the self-limiting behavior, ALD can produce highly uniform and conformal films over three-dimensional structures with precise thickness control, which meets well the demands of sub-10 nm node fabrication.[33] Therefore, ALD is an excellent approach to achieve ASD and there have been increasing reports working on area-selective atomic layer deposition (AS-ALD).[27–29,31,35] In the practice of AS-ALD, there are regions of different reactivities toward ALD precursors on pre-patterned substrates. ALD precursors absorb on the reactive regions and films grow there. Area-activation and area-deactivation are two common ways to create regions of different reactivities toward ALD precursors on a substrate, as shown in Figure 1.3.[36] Area-activation means desired regions of non-reactive substrates are functionalized by reactive groups while area-deactivation means desired regions of reactive substrates are passivated by non-reactive groups.[37,38]

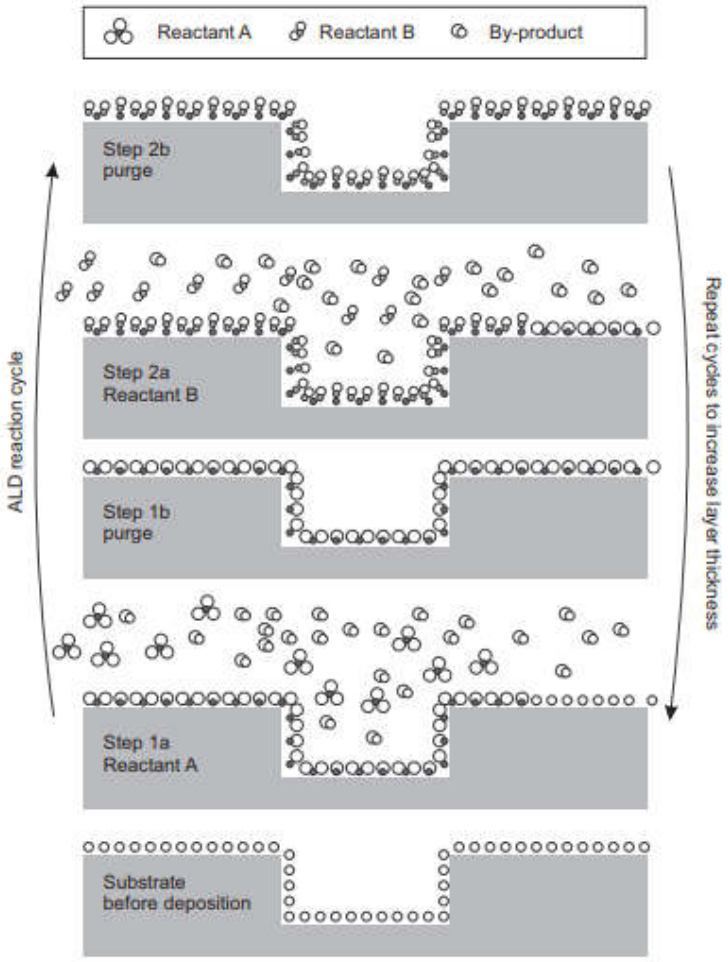

Figure 1.2. Schematic of ALD reaction process.[34]

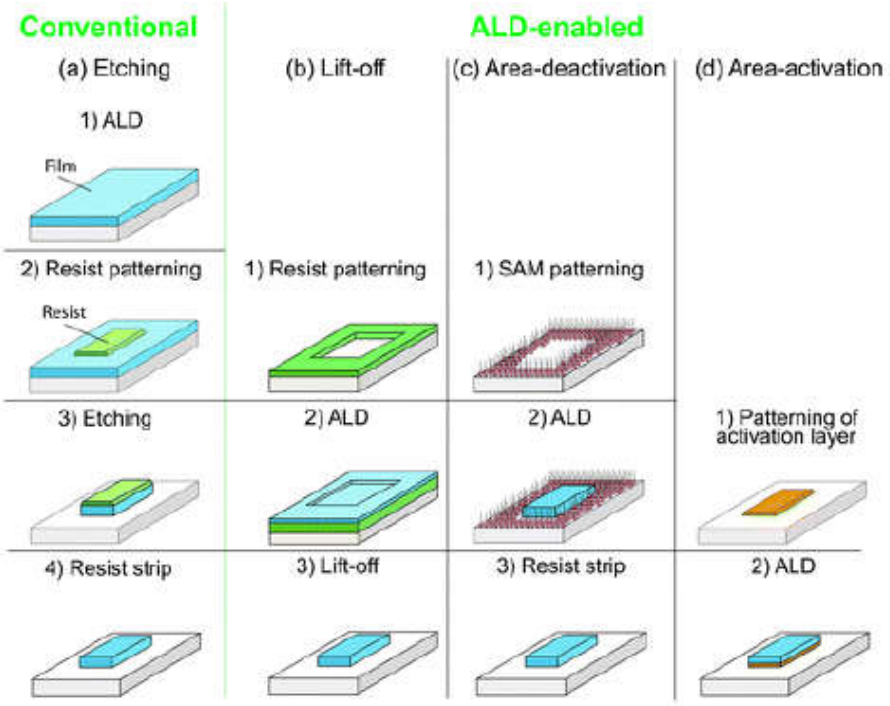

Figure 1.3. Schematic of area-selective ALD.[36]

1.2.2 Passivation Materials for AS-ALD

The selection and patterning of passivation materials is the key to AS-ALD enabled by area-deactivation.[36] Self-assembled monolayers, such as octadecyltrichlorosilane, are the most-widely used passivation materials in current ASD studies due to their excellent passivation effects and self-alignment behavior to certain surface sites.[39–44] But SAMs have their limitations. First, to produce a defect-free SAM layer that can block nucleation and growth well, extended SAM deposition time as long as 24 h is required for many SAMs.[42,45] Besides, SAMs are just monolayers and if a thick ALD film is grown, it can grow up and beyond the feature boundary. SAMs have the potential to be degraded or even damaged and so lose their passivation capabilities after a

long deposition time, which leads to SAM failure in ASD of thick films.[46,47] Additionally, SAM patterning approaches have not been fully developed. While micro-patterns can be generated by methods like microcontact printing, nano-patterning of SAMs is still difficult.[37,40]

To overcome these limitations of SAMs and target the applications that SAMs cannot meet, considerable research attention has focused on another group of passivation materials—polymer films.[31,48–52] Defect-free polymer films can be coated onto a substrate within a few minutes and polymer film thickness can be easily tuned from nanometers to micrometers. So using polymer films as passivation materials can work in ASD of thick films. Another important advantage is that there have been many developed patterning approaches for polymer films to produce both micro-patterns and nano-patterns, such as photolithography and directed self-assembly.[53] A number of polymers have been identified as effective growth inhibitors to certain materials, such as polyimide and polymethacrylamide to platinum deposition,[38,52] poly(vinyl pyrrolidone) to noble metal deposition,[51] and poly(methylmethacrylate) to TiO_2 deposition.[31] However, there is no report exploring the feasibility of using polystyrene (PS) as a passivation material. There are only C and H elements in PS as shown in Figure 1.4, so the materials whose nucleation and growth rely on hydroxyl groups cannot grow on PS film in principle. PS films possess no glass transition temperature after UV-induced crosslinking,[54] which means PS film can work over a wide temperature window (< 240 °C). Besides, as a photo-sensitive polymer and a common component of copolymers, PS can be patterned easily by photolithography or direct self-assembly. A diblock copolymer is a polymer

consisting two different kinds of monomers whose chains are grafted together. Tuned by molecular interaction and component fraction, monomer segments can segregate and form regular and periodic structures, and this process is called directed self-assembly, as shown in Figure 1.5.[55] Polystyrene-block-poly(methylmethacrylate) is the most common diblock copolymer and its self-assembly has been studied extensively, which can offer nanoscale PS patterns after removing PMMA component.[56–58] These advantages make PS film a promising passivation material candidate.

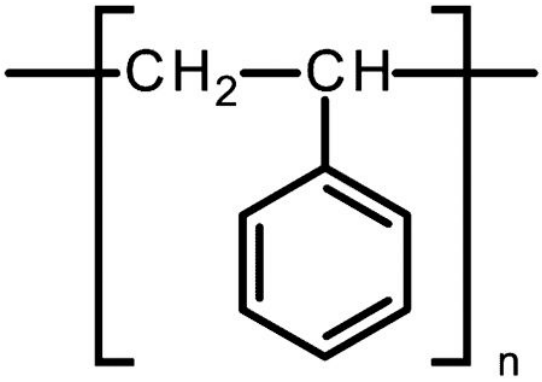

Figure 1.4. Schematic of repeat unit of polystyrene.

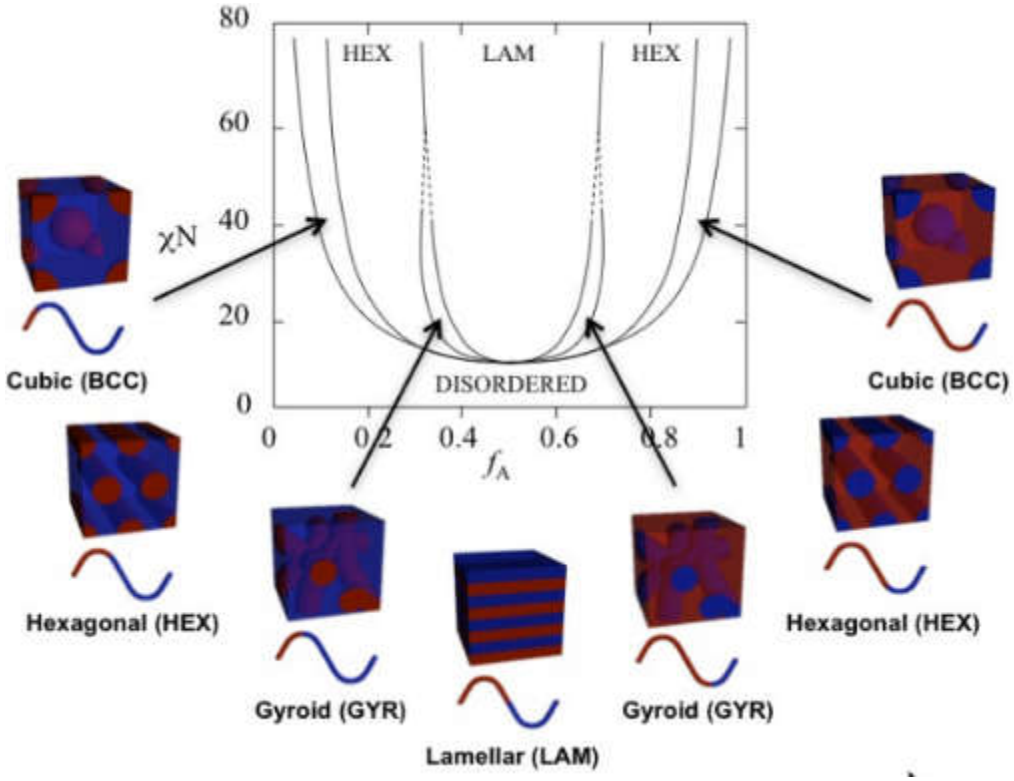

Figure 1.5. Schematic of directed self-assembly of diblock copolymers.[55]

1.2.3 ALD of Cobalt Metal

Cobalt (Co) and magnesium oxide (MgO) are typical ferromagnetic and tunnel barrier layers, respectively, in a MTJ stack. The ALD of MgO is well-explored while the ALD of Co remains sparse. While most cobalt ALD precursors are organometallic compounds, relatively high energy is needed to convert the Co^{2+} or Co^{3+} to Co^0, and the relatively high energy normally comes from either plasma enhancement or high temperature. Plasma-enhanced ALD of cobalt metal has been reported by using precursors like $Co_2(CO)_8$, $CoCp_2$, and $Co(MeCp)_2$ and plasmas like H_2 and NH_3. But plasma may damage the substrate surface and the anisotropy of plasma bombardment

compromises the excellent conformality of ALD. [59–61] Themal ALD of cobalt metal has been achieved at a temperature above 260 °C by using bis(N,N'-di-i-propylacetamidinato)cobalt(II) and bis(N-t-butyl-N'-ethylpropanimidamidato)cobalt(II) precursors and H_2, but there is incorporation of C and N impurities in the Co film due to the decomposition of precursor ligands at high temperature.[62–64] Besides, both plasma and high temperature may damage passivation materials and so are not compatible with area-selective deposition using SAMs and possibly PS. Recently, with the development of new cobalt precursors and new coreactants, thermal ALD of cobalt metal has been demonstrated at a relatively low temperature below 200 °C by the Chabal and Winter groups, but these processes cannot grow Co on oxide substrates due to the selective nucleation behavior of their precursors toward metal substrates.[65–67] This means these processes cannot apply to deposition of cobalt metal on a tunnel barrier oxide for MTJ fabrication.

Another strategy to produce metal films is reducing metal oxides by using reducing agents. A common problem for this strategy is dewetting phenomenon during high temperature processing of metals on oxide substrates, especially for ultrathin metal films.[68–71] Figure 1.6 shows a schematic of dewetting. The driving force of dewetting is the minimization of the total energy of the film-substrate interface, film surface and substrate surface.[68] The edges of metastable films have the tendency to shrink and form islands when enough atom mobility is offered by thermal energy. Dewetting normally starts at the edges of voids which can be as small as nanometer size. During reduction the loss of oxygen atoms creates voids within the films, which facilitates the onset of

dewetting. Common solutions to suppress dewetting include lowering heat input and using an adsorbate layer or a capping layer to restrain surface diffusion.[68]

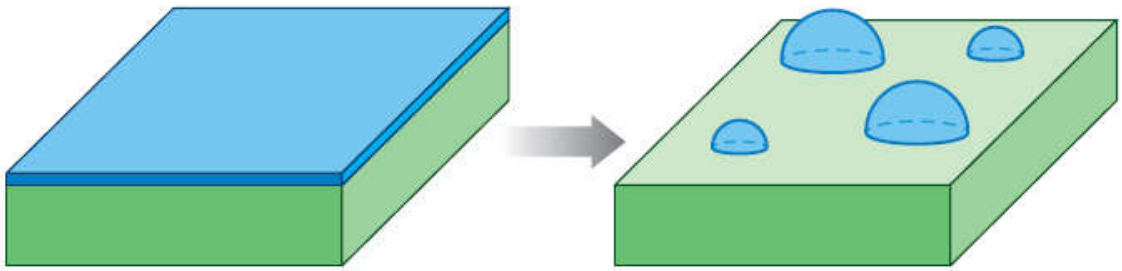

Figure 1.6. Schematic of dewetting.[68]

1.3 RESEARCH OBJECTIVES AND CHAPTER OVERVIEW

The goal of this research project is to achieve area-selective atomic layer deposition of cobalt metal films on an MgO tunnel barrier as a step toward fabrication of a magnetic tunnel junction. The route of depositing CoO by an AS-ALD process and then reducing CoO to Co metal is selected. To realize this goal, a fabrication process that leads to impurity-free and continuous cobalt metal films on MgO and that is well compatible with area-selective deposition process needs to be developed. Moreover, the reduction process determines the microstructure and the magnetic properties of the resulting cobalt metal film. Therefore a study elucidating the process-structure-property relationship is very useful to produce cobalt metal films with the desired magnetic properties for the MTJ application. Besides, exploration of the proper passivation materials that block cobalt oxide growth on the MgO surface and the demonstration of this AS-ALD process are in demand.

Chapter 2 introduces the research facilities, characterization methods, and experimental details of the work.

In Chapter 3, we report the deposition of 4.5-nm thick cobalt (II) oxide on SiO_2/Si and MgO(001) substrates at a temperature of 170–180 °C by ALD using bis(N-*tert* butyl, N'-ethylpropionamidinato) cobalt (II) and deionized water as co-reactants. The resulting CoO film is smooth and carbon-free. Two low temperature (around 200 °C) reduction methods are discussed including deuterium atom reduction and use of an O scavenger layer (Al metal). The low temperature methods can attenuate dewetting to a large extent and the resulting metallic cobalt is smooth and continuous film.

Chapter 4 analyzes how the parameters of the deuterium atom reduction of CoO affect the structure and magnetic properties of the resulting Co film. The increase of reduction temperature, partial pressure of deuterium, and reaction time increases the average grain size and the roughness of the Co film. Co films with larger average grain size show higher coercivity in magnetic measurements. The film structure and coercivity also depend on the substrate choice. Co films that are grown on substrates with lower dewetting tendency, such as MgO and Al_2O_3, show smaller average grain size and smaller coercivity.

In Chapter 5, we explore the passivation effects of polystyrene and demonstrate the area-selective deposition of cobalt (II) oxide on polystyrene-patterned SiO_2/Si and MgO(001) substrates. The CoO patterns can be further reduced to produce Co metal patterns without deformation by using atomic deuterium reduction at 220 °C. Polystyrene is very effective in blocking atomic layer deposition of CoO. The polystyrene is patterned

using UV-crosslinked 40-nm PS films or using self-assembled 40-nm polystyrene-polymethylmethacrylate (PS-PMMA) films.

Finally, Chapter 6 summarizes this work and proposes some suggestions for potential future directions of this research project.

1.4 REFERENCES

1. Waldrop, M. M. The chips are down for Moore's law. *Nat. News* **530,** 144 (2016).
2. Kawahara, T., Ito, K., Takemura, R. & Ohno, H. Spin-transfer torque RAM technology: Review and prospect. *Microelectron. Reliab.* **52,** 613–627 (2012).
3. Chen, E. *et al.* Advances and Future Prospects of Spin-Transfer Torque Random Access Memory. *IEEE Trans. Magn.* **46,** 1873–1878 (2010).
4. Wang, K. L., Alzate, J. G. & Amiri, P. K. Low-power non-volatile spintronic memory: STT-RAM and beyond. *J. Phys. Appl. Phys.* **46,** 74003 (2013).
5. Zhang, Y., Zhang, L., Wen, W., Sun, G. & Chen, Y. Multi-level cell STT-RAM: Is it realistic or just a dream? in *2012 IEEE/ACM International Conference on Computer-Aided Design (ICCAD)* 526–532 (2012).
6. Ikeda, S. *et al.* Magnetic Tunnel Junctions for Spintronic Memories and Beyond. *IEEE Trans. Electron Devices* **54,** 991–1002 (2007).
7. Driskill-Smith, A. *et al.* Latest Advances and Roadmap for In-Plane and Perpendicular STT-RAM. in *2011 3rd IEEE International Memory Workshop (IMW)* 1–3 (2011). doi:10.1109/IMW.2011.5873205
8. Telepinsky, Y. *et al.* Towards a six-state magnetic memory element. *Appl. Phys. Lett.* **108,** 182401 (2016).
9. Pramanik, T., Roy, U., Register, L. F. & Banerjee, S. K. Proposal of a Multistate Memory Using Voltage Controlled Magnetic Anisotropy of a Cross-Shaped Ferromagnet. *IEEE Trans. Nanotechnol.* **14,** 883–888 (2015).
10. Gates, B. D. *et al.* New Approaches to Nanofabrication: Molding, Printing, and Other Techniques. *Chem. Rev.* **105,** 1171–1196 (2005).
11. Xue, L. *et al.* A Self-Aligned Two-Step Reactive Ion Etching Process for Nanopatterning Magnetic Tunnel Junctions on 300 mm Wafers. *IEEE Trans. Magn.* **50,** 1–3 (2014).
12. Gajek, M. *et al.* Spin torque switching of 20 nm magnetic tunnel junctions with perpendicular anisotropy. *Appl. Phys. Lett.* **100,** 132408 (2012).

13. Neisser, M. & Wurm, S. ITRS lithography roadmap: 2015 challenges. *Adv. Opt. Technol.* **4,** 235–240 (2015).

14. Boullart, W. *et al.* STT MRAM patterning challenges. in *Advanced Etch Technology for Nanopatterning II* **8685,** 86850F (International Society for Optics and Photonics, 2013).

15. Chawla, J. S. *et al.* Patterning challenges in the fabrication of 12 nm half-pitch dual damascene copper ultra low-k interconnects. in *Advanced Etch Technology for Nanopatterning III* **9054,** 905404 (International Society for Optics and Photonics, 2014).

16. Eom, T.-S. *et al.* Patterning challenges of EUV lithography for 1X-nm node DRAM and beyond. in *Extreme Ultraviolet (EUV) Lithography IV* **8679,** 86791J (International Society for Optics and Photonics, 2013).

17. Hontake, K. *et al.* Coater/developer based techniques to improve high-resolution EUV patterning defectivity. in *International Conference on Extreme Ultraviolet Lithography 2017* **10450,** 104501U (International Society for Optics and Photonics, 2017).

18. Burkhardt, M. Investigation of alternate mask absorbers in EUV lithography. in *Extreme Ultraviolet (EUV) Lithography VIII* **10143,** 1014312 (International Society for Optics and Photonics, 2017).

19. Bakshi, V., Mizoguchi, H., Liang, T., Grenville, A. & Benschop, J. P. Special Section Guest Editorial: EUV Lithography for the 3-nm Node and Beyond. *J. MicroNanolithography MEMS MOEMS* **16,** 41001 (2017).

20. Metz, A. W. *et al.* Overcoming etch challenges related to EUV based patterning. in *Advanced Etch Technology for Nanopatterning VI* **10149,** 1014906 (International Society for Optics and Photonics, 2017).

21. M. F. Shieh, C. M Lai, K. H Hsieh, R. G. Liu & S. M. Chang. Self aligned patterning with multiple resist layers. (2017).

22. C. W. Lu, C. J. Lee & S. L. Shue. Method of forming multiple patterning spacer structures. (2017).

23. Mallik, A. *et al.* The need for EUV lithography at advanced technology for sustainable wafer cost. in *Extreme Ultraviolet (EUV) Lithography IV* **8679,** 86792Y (International Society for Optics and Photonics, 2013).

24. Lu, W. & Lieber, C. M. Nanoelectronics from the bottom up. *Nat. Mater.* **6,** 841–850 (2007).

25. Xia, Y., Rogers, J. A., Paul, K. E. & Whitesides, G. M. Unconventional Methods for Fabricating and Patterning Nanostructures. *Chem. Rev.* **99,** 1823–1848 (1999).

26. Ozin, G. A. *et al.* Nanofabrication by self-assembly. *Mater. Today* **12,** 12–23 (2009).

27. Dong, W. *et al.* Application of three-dimensionally area-selective atomic layer deposition for selectively coating the vertical surfaces of standing nanopillars. *Sci. Rep.* **4,** 4458 (2014).

28. Fang, M. & Ho, J. C. Area-Selective Atomic Layer Deposition: Conformal Coating, Subnanometer Thickness Control, and Smart Positioning. *ACS Nano* **9,** 8651–8654 (2015).

29. Thissen, N. F. W. *et al.* Graphene devices with bottom-up contacts by area-selective atomic layer deposition. *2D Mater.* **4,** 25046 (2017).

30. Yan, K. *et al.* Selective deposition and stable encapsulation of lithium through heterogeneous seeded growth. *Nat. Energy* **1,** 16010 (2016).

31. Haider, A., Yilmaz, M., Deminskyi, P., Eren, H. & Biyikli, N. Nanoscale selective area atomic layer deposition of TiO 2 using e-beam patterned polymers. *RSC Adv.* **6,** 106109–106119 (2016).

32. Mameli, A. *et al.* Area-Selective Atomic Layer Deposition: Role of Surface Chemistry. *ECS Trans.* **80,** 39–48 (2017).

33. George, S. M. Atomic Layer Deposition: An Overview. *Chem. Rev.* **110,** 111–131 (2010).

34. Miikkulainen, V., Leskelä, M., Ritala, M. & Puurunen, R. L. Crystallinity of inorganic films grown by atomic layer deposition: Overview and general trends. *J. Appl. Phys.* **113,** 21301 (2013).

35. Kim, W.-H. *et al.* Atomic Layer Deposition of Ni Thin Films and Application to Area-Selective Deposition. *J. Electrochem. Soc.* **158,** D1–D5 (2011).

36. Mackus, A. J. M., Bol, A. A. & Kessels, W. M. M. The use of atomic layer deposition in advanced nanopatterning. *Nanoscale* **6,** 10941–10960 (2014).

37. Mameli, A. *et al.* Area-Selective Atomic Layer Deposition of In2O3:H Using a μ-Plasma Printer for Local Area Activation. *Chem. Mater.* **29,** 921–925 (2017).

38. Vervuurt, R. H. J., Sharma, A., Jiao, Y., Kessels, W. (Erwin) M. M. & Bol, A. A. Area-selective atomic layer deposition of platinum using photosensitive polyimide. *Nanotechnology* **27,** 405302 (2016).

39. Hoeppener, S. *et al.* Metal Nanoparticles, Nanowires, and Contact Electrodes Self-Assembled on Patterned Monolayer Templates—A Bottom-up Chemical Approach. *Adv. Mater.* **14,** 1036–1041 (2002).

40. Park, M. H., Jang, Y. J., Sung-Suh, H. M. & Sung, M. M. Selective Atomic Layer Deposition of Titanium Oxide on Patterned Self-Assembled Monolayers Formed by Microcontact Printing. *Langmuir* **20,** 2257–2260 (2004).

41. Chen, R., Kim, H., McIntyre, P. C., Porter, D. W. & Bent, S. F. Achieving area-selective atomic layer deposition on patterned substrates by selective surface modification. *Appl. Phys. Lett.* **86,** 191910 (2005).

42. Chen, R., Kim, H., McIntyre, P. C. & Bent, S. F. Self-assembled monolayer resist for atomic layer deposition of HfO2 and ZrO2 high-κ gate dielectrics. *Appl. Phys. Lett.* **84,** 4017–4019 (2004).

43. Jiang, X. & Bent, S. F. Area-Selective Atomic Layer Deposition of Platinum on YSZ Substrates Using Microcontact Printed SAMs. *J. Electrochem. Soc.* **154,** D648–D656 (2007).

44. Minaye Hashemi, F. S., Prasittichai, C. & Bent, S. F. Self-Correcting Process for High Quality Patterning by Atomic Layer Deposition. *ACS Nano* **9,** 8710–8717 (2015).

45. Hashemi, F. S. M., Prasittichai, C. & Bent, S. F. A New Resist for Area Selective Atomic and Molecular Layer Deposition on Metal–Dielectric Patterns. *J. Phys. Chem. C* **118,** 10957–10962 (2014).

46. Chopra, S. N., Zhang, Z., Kaihlanen, C. & Ekerdt, J. G. Selective Growth of Titanium Nitride on HfO2 across Nanolines and Nanopillars. *Chem. Mater.* **28,** 4928–4934 (2016).

47. Hashemi, F. S. M. & Bent, S. F. Sequential Regeneration of Self-Assembled Monolayers for Highly Selective Atomic Layer Deposition. *Adv. Mater. Interfaces* **3,** 1600464 (2016).

48. Sinha, A., Hess, D. W. & Henderson, C. L. Area selective atomic layer deposition of titanium dioxide: Effect of precursor chemistry. *J. Vac. Sci. Technol. B Microelectron. Nanometer Struct. Process. Meas. Phenom.* **24,** 2523–2532 (2006).

49. Hua, Y., King, W. P. & Henderson, C. L. Nanopatterning materials using area selective atomic layer deposition in conjunction with thermochemical surface modification via heated AFM cantilever probe lithography. *Microelectron. Eng.* **85,** 934–936 (2008).

50. Ellinger, C. R. & Nelson, S. F. Selective Area Spatial Atomic Layer Deposition of ZnO, Al2O3, and Aluminum-Doped ZnO Using Poly(vinyl pyrrolidone). *Chem. Mater.* **26,** 1514–1522 (2014).

51. Färm, E., Kemell, M., Santala, E., Ritala, M. & Leskelä, M. Selective-Area Atomic Layer Deposition Using Poly(vinyl pyrrolidone) as a Passivation Layer. *J. Electrochem. Soc.* **157,** K10–K14 (2010).

52. Mullings, M. N. *et al.* Area Selective Atomic Layer Deposition by Microcontact Printing with a Water-Soluble Polymer. *J. Electrochem. Soc.* **157,** D600–D604 (2010).

53. Nie, Z. & Kumacheva, E. Patterning surfaces with functional polymers. *Nat. Mater.* **7,** 277–290 (2008).

54. Bui, V.-T., Lee, H. S., Choi, J.-H. & Choi, H.-S. Data from crosslinked PS honeycomb thin film by deep UV irradiation. *Data Brief* **5,** 990–994 (2015).

55. Swann, J. M. G. & Topham, P. D. Design and Application of Nanoscale Actuators Using Block-Copolymers. *Polymers* **2,** 454–469 (2010).

56. Ruiz, R. *et al.* Density Multiplication and Improved Lithography by Directed Block Copolymer Assembly. *Science* **321,** 936–939 (2008).

57. Thurn-Albrecht, T. *et al.* Nanoscopic Templates from Oriented Block Copolymer Films. *Adv. Mater.* **12,** 787–791

58. Xu, T. *et al.* The influence of molecular weight on nanoporous polymer films. *Polymer* **42,** 9091–9095 (2001).

59. Kim, K. *et al.* Comparison of Co Films Deposited by Remote Plasma Atomic Layer Deposition Method with Cyclopentadienylcobalt Dicarbonyl [CpCo(CO)2] and Dicobalt Octacarbonyl [Co2(CO)8]. *Jpn. J. Appl. Phys.* **46,** L173 (2007).

60. Yoon, J. *et al.* Atomic Layer Deposition of Co Using N2/H2 Plasma as a Reactant. *J. Electrochem. Soc.* **158,** H1179–H1182 (2011).

61. Park, J. *et al.* Plasma-enhanced atomic layer deposition of Co using Co(MeCp)2 precursor. *J. Energy Chem.* **22,** 403–407 (2013).

62. Lee, H.-B.-R. *et al.* High Quality Area-Selective Atomic Layer Deposition Co Using Ammonia Gas as a Reactant. *J. Electrochem. Soc.* **157,** D10–D15 (2010).

63. Elko-Hansen, T. D.-M., Dolocan, A. & Ekerdt, J. G. Atomic Interdiffusion and Diffusive Stabilization of Cobalt by Copper During Atomic Layer Deposition from Bis(N-tert-butyl-N′-ethylpropionamidinato) Cobalt(II). *J. Phys. Chem. Lett.* **5,** 1091–1095 (2014).

64. Elko-Hansen, T. D.-M. & Ekerdt, J. G. XPS Investigation of the Atomic Layer Deposition Half Reactions of Bis(N-tert-butyl-N′-ethylpropionamidinato) Cobalt(II). *Chem. Mater.* **26,** 2642–2646 (2014).

65. Kwon, J., Saly, M., Halls, M. D., Kanjolia, R. K. & Chabal, Y. J. Substrate Selectivity of (tBu-Allyl)Co(CO)3 during Thermal Atomic Layer Deposition of Cobalt. *Chem. Mater.* **24,** 1025–1030 (2012).

66. Kalutarage, L. C., Martin, P. D., Heeg, M. J. & Winter, C. H. Volatile and Thermally Stable Mid to Late Transition Metal Complexes Containing α-Imino Alkoxide Ligands, a New Strongly Reducing Coreagent, and Thermal Atomic Layer Deposition of Ni, Co, Fe, and Cr Metal Films. *J. Am. Chem. Soc.* **135,** 12588–12591 (2013).

67. Klesko, J. P., Kerrigan, M. M. & Winter, C. H. Low Temperature Thermal Atomic Layer Deposition of Cobalt Metal Films. *Chem. Mater.* **28,** 700–703 (2016).

68. Thompson, C. V. Solid-State Dewetting of Thin Films. *Annu. Rev. Mater. Res.* **42,** 399–434 (2012).

69. Lee, J.-M. & Kim, B.-I. Thermal dewetting of Pt thin film: Etch-masks for the fabrication of semiconductor nanostructures. *Mater. Sci. Eng. A* **449–451,** 769–773 (2007).

70. Müller, C. M. & Spolenak, R. Microstructure evolution during dewetting in thin Au films. *Acta Mater.* **58,** 6035–6045 (2010).

71. Ye, J. & Thompson, C. V. Mechanisms of complex morphological evolution during solid-state dewetting of single-crystal nickel thin films. *Appl. Phys. Lett.* **97,** 71904 (2010).

Chapter 2: Research Methodology

2.1 RESEARCH FACILITIES

Figure 2.1 shows the ultra-high vacuum (UHV) system in Materials Physics Laboratory where most of our experiments were conducted. There is an atomic layer deposition (ALD) chamber, a reduction chamber, an X-ray photoelectron spectroscopy (XPS) analysis chamber and a molecular beam epitaxy (MBE) chamber in the UHV system.

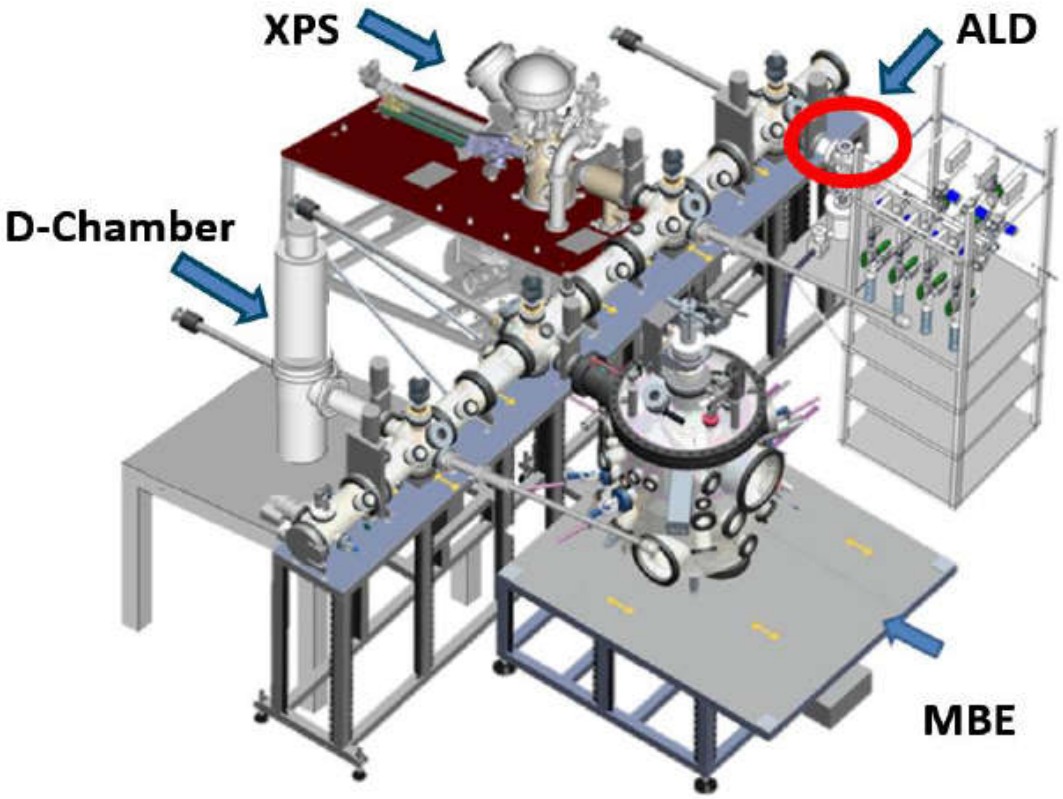

Figure 2.1. Schematic of the UHV system used in this work.[1]

The ALD chamber is custom-built as shown in Figure 2.2. It is a hot wall stainless steel rectangular chamber with the length of 20 cm and the volume of 460 cm^3. Ultrahigh purity argon is used as a purge/carrier gas and the flow rate is regulated by mass flow controllers. The substrate temperature is monitored with a reference thermocouple in the ALD chamber that was previously calibrated against an instrumented wafer.

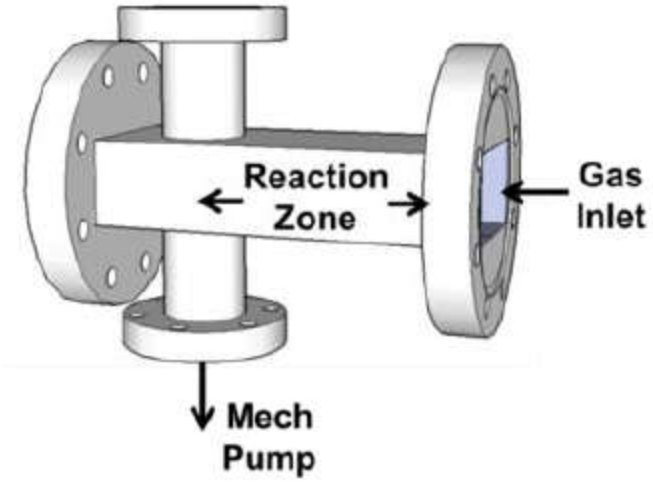

Figure 2.2. Schematic of the ALD chamber used in this work.[1]

The reduction chamber is shown in Figure 2.3. The components from top to bottom in Figure 2.3b are a pyrolytic boron nitride heater, a sample stage, and a tungsten filament, respectively. Deuterium gas (Matheson, 99.999%) flows into the chamber from the top and its partial pressure is controlled by a leak valve. The pyrolytic boron nitride heater is 2 cm above the sample stage. The sample stage is positioned approximately 4 cm above and faced toward the tungsten filament. The sample temperature is monitored

with a reference thermocouple in the vacuum chamber that was previously calibrated against an instrumented wafer. The tungsten filament is a 400-W Osram Xenophot bulb, which has part of the glass enclosure removed to expose the filament. A current of 5.2 A can be supplied by a DC power supply (KEPCO, MSK10-10M) to the tungsten filament and produce a temperature above 1800 K, which was calibrated by a thermal pyrometer. At this temperature, the tungsten filament can crack deuterium molecule to generate atomic deuterium.[2] The flux of atomic deuterium is estimated around 2×10^{13} D/cm^2·s based on previous work.[3] When the tungsten filament is not powered on, the sample on the stage is processed by D_2 gas. When the tungsten filament is powered on, the sample on the stage is processed by a combination of D_2 gas and D atoms.

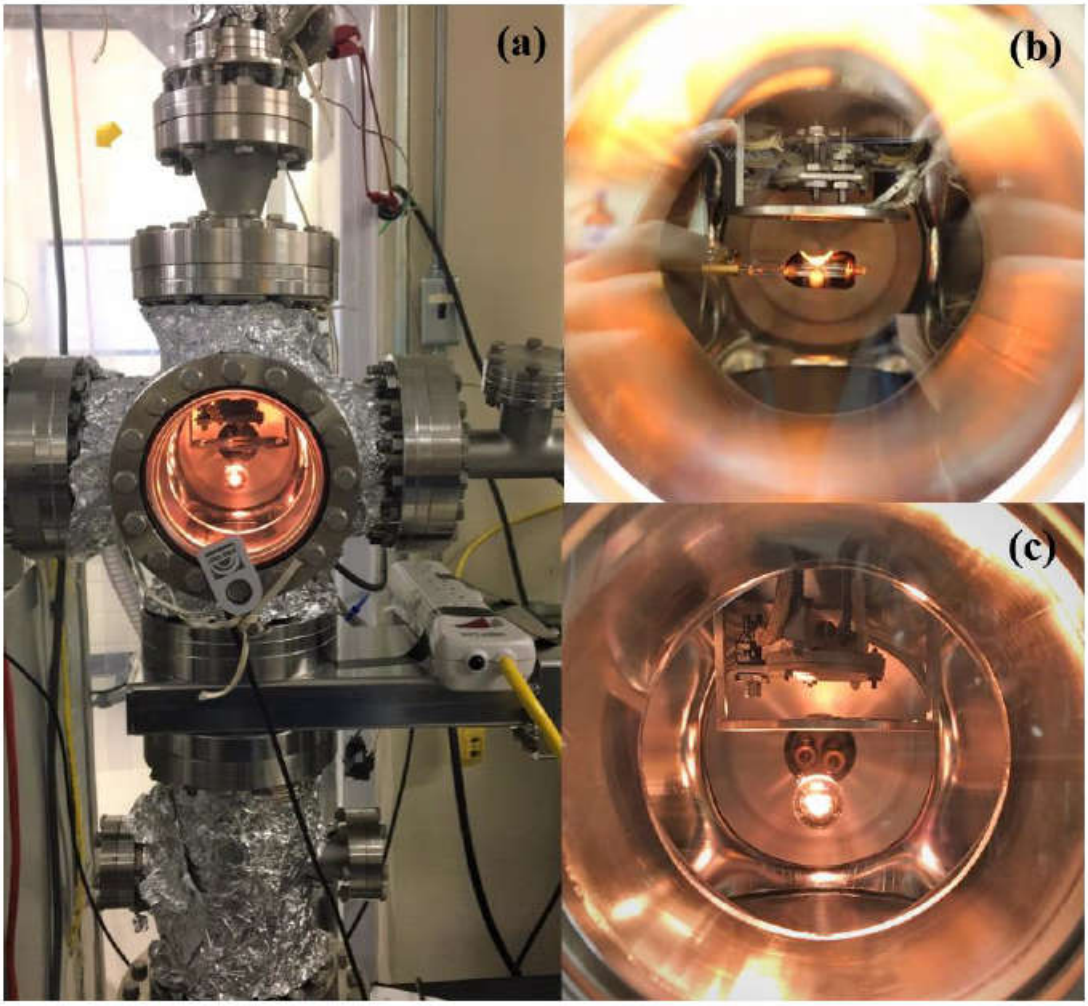

Figure 2.3. (a) Image of the reduction chamber. (b) and (c) are inside side view and inside front view of the chamber, respectively.[4]

An *in-situ* VG Scienta R3000 XPS system with a monochromated Al Kα source at 1486.6 eV was used to determine film stoichiometry and composition, and the oxidation states of substrates and films. The absolute energy scale of the analyzer of the XPS system was calibrated using a two-point measurement such that the Ag $3d_{5/2}$ core level is at 368.26 eV and the Fermi edge of Ag is at 0.0 eV. A reference Co 2*p* XP spectrum for

cobalt-based materials is shown in Figure 2.4.[5] The DCA-MBE is equipped with six effusion cells (four standard and two high-temperature), a four-pocket electron beam evaporator, a quartz crystal microbalance (QCM), a reflective high energy electron diffraction system (RHEED, Staib Instruments operating at 21 keV) and a radio frequency plasma source of both oxygen and nitrogen. Film crystallinity was observed *in-situ* by RHEED.

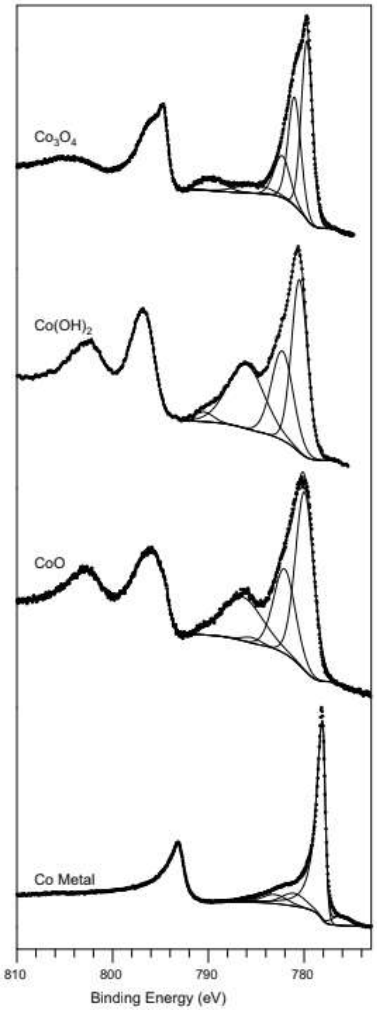

Figure 2.4. Co 2*p* XP spectrum for Co metal, CoO, $Co(OH)_2$ and Co_3O_4.[5]

2.2 *EX-SITU* CHARACTERIZATIONS

X-ray reflectivity (XRR) was used to determine the film thicknesses and growth rate. XRR was conducted by a Panalytical X'PERT Pro diffractometer using a sealed tube Cu Kα radiation source (λ ~ 1.5406 Å) operating at 40 kV and 30 mA. For continuous films with a thickness over 4 nm, oscillation is observable from XRR, and the thickness is estimated by using the Kiessig fringe period.[6] The film thickness is calculated by Bragg's Law $d = \lambda/(2\sin\Delta\theta)$, while λ (1.5406 Å) is the wavelength of incident wave. Figure 2.5 shows an XRR example of 300-cycle CoO film grown on MgO(001) substrate by ALD. From this graph it is seen that 2θ = 0.98 degree, so the thickness d is 89.8 Å and the grow rate is about 0.3 Å/cycle.

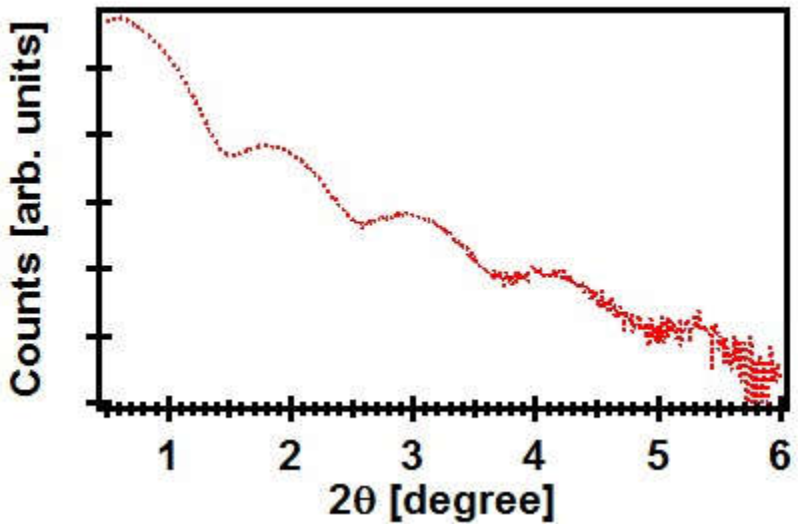

Figure 2.5. XRR result of a 300-cycle CoO film grown on MgO(001) substrate by ALD.

Scanning electron microscopy (SEM) and atomic force microscopy (AFM) were used to characterize the film morphology and the structure of the patterns. SEM was

conducted by a ZEISS Neon 40 SEM equipped with Bruker energy dispersive spectroscopy (EDS). AFM was conducted by a Veeco Icon AFM system with tapping mode with Bruker TESPA AFM tips.

Magnetic property measurements were carried out with a Quantum Design physical property measurement system (PPMS) combined with the vibrating sample magnetometry (VSM) option. Magnetization hysteresis loops were measured with the magnetic field applied parallel to the plane of the thin films. For all the measurements, the samples were at room temperature (25 °C).

2.3 EXPERIMENTAL METHODS

2.3.1 Sample Preparation, Film Growth and Reduction

Four-inch wafers of SiO_2/Si(001) were prepared by a thermal oxidation method, which produce an amorphous 300 nm-thick SiO_2 layer on Si substrates. The 0.5 mm-thick wafers were then cut into 20 × 20 mm^2 pieces. MgO(001) substrates of 10 mm × 10 mm × 0.5 mm are purchased from MTI corporation. The substrates were ultrasonically cleaned with acetone, isopropyl alcohol, and deionized (DI) water for 5 min each, followed by UV/ozone treatment for 15 min to remove residual carbon contamination.

Bis(N-tert butyl, N'-ethylpropionamidinato) cobalt (II) (Strem, 98%) and deionized water were used as co-reactants for the ALD growth of CoO. During CoO growth, the Co precursor and water were held at 80 °C and room temperature (25 °C), respectively, while the substrate was maintained at a temperature range of 170–180 °C. The water dosing was regulated using an in-line needle valve. Each cycle of CoO growth

consisted of a 2-sec dose of Co, a 20-sec purge of Ar, a 1-sec dose of H_2O, and a 20-sec purge of Ar. The deposition of Al metal was performed in a MBE chamber at 200 °C with a base pressure of 5×10^{-9} Torr. The deuterium gas and deuterium atom reduction were conducted in a custom-built vacuum chamber. The deuterium gas partial pressure was controlled by a leak valve. The sample temperature was monitored with a reference thermocouple in the vacuum chamber that was previously calibrated against an instrumented wafer.

2.3.2 Preparation of Polystyrene Templates for Area-Selective Deposition

Polystyrene (Aldrich, with average Mw = 200000) was dissolved in propylene glycol methyl ether acetate (Sigma-Aldrich, 99.5%) to prepare a 2 wt% polystyrene solution. The 2 wt% polystyrene solution was spincoated onto cleaned SiO_2/Si or MgO(001) substrates to form a 40 nm-thick polystyrene film on the substrates. The PS/SiO_2/Si or PS/MgO(001) samples were then exposed by 185 nm and 254 nm ultraviolet light in an ambient or N_2 environment with a shadow mask on the top of samples. The shadow mask used in this work was a slim-bar 1000 mesh copper TEM grid with pitch of 25 μm, bar width of 6 μm and hole width of 19 μm. The PS regions that were not shadowed by the mask were exposed to deep UV light and crosslinked while the PS regions that were shadowed by the mask were not exposed to deep UV light and not crosslinked. After UV light exposure, the samples were rinsed by toluene (Fisher Chemical, 99.9%) and cleaned by DI water. The PS regions that were not crosslinked were removed and PS micro-patterns formed on substrates.

PS nano-patterns were formed by using self-assembled PMMA-PS diblock copolymers. Random copolymer poly(styrene-co-methyl methacrylate) with α-hydroxyl-ω-tempo moiety terminated was purchased from Polymer Source. The Mn of the random copolymer was 6400 with 59.5 mol% styrene. The random copolymer was dissolved in toluene to prepare a 1 wt% random copolymer solution. Poly(styrene-b-methyl methacrylate) diblock copolymer was also purchased from Polymer Source. The Mn of styrene was 55000 and the Mn of methyl methacrylate was 22000. The diblock copolymer was dissolved in toluene to prepare a 1 wt% diblock copolymer solution. The 1 wt% random copolymer solution was first spincoated onto cleaned SiO_2/Si or MgO(001) substrates to form a 50 nm-thick polymer layer. Then the samples were heated on a hot plate at 230 °C for 10 min, in which about 3 nm-thick brush layer was end-grafted onto substrates. After rinsing the samples by toluene, the bulk non-grafted random copolymer was removed and only the 3 nm-thick end-grafted brush layer remained on substrates. The 1 wt% diblock copolymer solution was then spincoated onto the brush layer-coated substrates to form a 50 nm-thick polymer layer. The samples were heated on a hot plate at 230 °C for 5 min during which PMMA formed cylinders aligned perpendicular to the substrate and PS formed a matrix. The PMMA cylinders and underlying brush layer were removed by plasma etching to generate nano-patterns of PS with 20-30 nm holes and 40-50 nm pitch on the substrates.

2.4 REFERENCES

1. McDaniel, M. D., Posadas, A., Wang, T., Demkov, A. A. & Ekerdt, J. G. Growth and characterization of epitaxial anatase TiO2(001) on SrTiO3-buffered Si(001) using atomic layer deposition. *Thin Solid Films* **520,** 6525–6530 (2012).
2. Bischler, U. & Bertel, E. Simple source of atomic hydrogen for ultrahigh vacuum applications. *J. Vac. Sci. Technol. A* **11,** 458–460 (1993).
3. McCrate, J. M. & Ekerdt, J. G. Detection of Low-Density Surface Sites on Silica: Experimental Evidence of Intrinsic Oxygen-Vacancy Defects. *Chem. Mater.* **26,** 2166–2171 (2014).
4. Shen Hu. PhD dissertation. (2017).
5. Biesinger, M. C. *et al.* Resolving surface chemical states in XPS analysis of first row transition metals, oxides and hydroxides: Cr, Mn, Fe, Co and Ni. *Appl. Surf. Sci.* **257,** 2717–2730 (2011).
6. Pietsch, U., Holy, V. & Baumbach, T. *High-Resolution X-Ray Scattering: From Thin Films to Lateral Nanostructures*. (Springer Science & Business Media, 2013).

Chapter 3: Atomic Layer Deposition of Cobalt Oxide and Low Temperature Reduction to Form Smooth and Continuous Cobalt Metal Thin Film

3.1 INTRODUCTION

Cobalt oxides have a wide range of applications, such as photocatalysts, electrodes, optical sensors, magnetic detectors, and catalysts, etc.[1–7] Thin films of cobalt oxides have been grown on different substrates exhibiting a variety of properties.[2–6] Cobalt (II) oxide has a band gap of 2.4 eV, which has been used for visible light driven photoelectrochemical water oxidation.[2] Cobalt spinel, Co_3O_4, a semiconductor with a band gap of 1.6 eV has been used for sensing, spintronics, and catalysis applications.[3–6] The growth of CoO and Co_3O_4 have been performed using different growth techniques, such as molecular beam epitaxy (MBE),[8–10] pulsed laser deposition,[11,12] chemical vapor deposition (CVD),[13–15] and atomic layer deposition (ALD).[2,16–18] Among them, ALD offers great film uniformity and conformality over large substrates, which are desired for most of applications. There have been a number of reports on the growth and characterization of cobalt oxides using ALD.[2,17–19]

Compared to cobalt oxides, cobalt metal is a widely-studied material for microelectronics and memory applications.[20–28] Co is well-known to have a good adhesion on the Cu surface. So Co and Co alloys thin films have been studied as a Cu electromigration barrier and as a next-generation liner material in the back end of line (BEOL) interconnects.[20–23] Besides, Co and Co alloys, such as CoFe and CoFeB, have been proposed as potential magnetic materials for the magnetic tunnel junction (MTJ).[24–28] A basic MTJ is composed of two ferromagnetic layers (known as the fixed and free

layers) separated by an ultra-thin insulating tunneling barrier.[26] While magnetic moment orientation of the fixed layer remains unchanged, the magnetic moment orientation of free layer can be switched during device-functioning. Crystallographic structure, particle size, and texture deeply effect magnetic properties, such as anisotropy, coercivity, and the magnetization reversal process. Therefore, the study of magnetic behavior of Co and Co alloys has attracted considerable attention.[29–32] Co metal can be used as either the fixed or free layer depending on its structure and particle size.[30–35]

The deposition of Co and Co alloys thin films has been performed by both physical vapor deposition and CVD techniques.[27–35]. With down-scaling of feature sizes of electronic devices, thin film uniformity and conformality become increasingly important, and this makes ALD a very attractive technique for cobalt metal film deposition, especially ultrathin cobalt metal films in interconnects or the MTJ stack. One advantage of ALD is precise thickness control at the monolayer level. The precursors will adsorb and subsequently desorb from the surface areas where reaction has reached completion to form a monolayer.[36] The self-limiting behavior of ALD produces very smooth and conformal films to the underlying substrates. When compared to sputtered Co-based magnetic films, a promising advantage of ALD films is that patterned films can be directly grown by area-selective ALD with reduction of alignment and post-deposition etching steps.[37–39] This has the potential to minimize the film quality degradation coming from structural or compositional damages caused by etching.

There are limited reports of ALD of cobalt metal.[39–47] While most cobalt ALD precursors are organometallic compounds, relatively high energy is needed to convert the

Co^{2+} or Co^{3+} to Co^0, and the relatively high energy normally comes from either plasma enhancement or high temperature. Plasma-enhanced ALD of cobalt metal has been reported by using precursors like $Co_2(CO)_8$, $CoCp_2$, and $Co(MeCp)_2$ and plasmas like H_2 and NH_3, but a plasma may damage the substrate surface and the anisotropy of plasma bombardment compromises the excellent conformality of ALD. [40–42] Thermal ALD of cobalt metal has been achieved at a temperature above 260 °C by using bis(N,N'-di-i-propylacetamidinato)cobalt(II) and bis(N-t-butyl-N'-ethylpropanimidamidato)cobalt(II) precursors and H_2, but there is incorportaion of C and N in the Co film due to the decomposition of precursors at high temperature.[39,43,44] Recently, thermal ALD of cobalt metal has been demonstrated at a relatively low temperature below 200 °C by Chabal and Winter groups, but these processes cannot grow Co on oxide substrates due to the selective nucleation behavior of their precursors toward metal substrates.[45–47]

Another strategy to produce metal films is reducing metal oxides by using reducing agents. In this study, we investigate the feasibility of producing cobalt films by reducing cobalt oxide. The reduction of CoO on oxide substrates by using hydrogen or deuterium gas at 400-500 °C reported herein results in discontinuous cobalt islands instead of continuous cobalt films. This dewetting phenomenon is common during high temperature processing of metals on oxide substrates, especially for ultrathin metal films.[48–51] Driven by minimization of the total energy of the film-substrate interface, film surface and substrate surface, the edges of metastable films have the tendency to shrink and form islands when enough atom mobility is offered by thermal energy.[48] Dewetting normally starts at the edges of voids which can be as small as nanometer size. During

reduction the loss of oxygen atoms creates voids within the films, which facilitates the onset of dewetting. In this work, we report a method combining low temperature (~180 °C) ALD process and low temperature (~200 °C) reduction process to growing impurity-free and continuous cobalt metal films on oxide substrates.

3.2 EXPERIMENTAL DETAILS

Four-inch wafers of SiO_2/Si(001) were prepared by a thermal oxidation method, which produce an amorphous 300 nm-thick SiO_2 layer on Si(001) substrates. The 0.5 mm-thick wafers were then cut into 20 × 20 mm^2 pieces. MgO(001) substrates of 10 mm × 10 mm × 0.5 mm were purchased from MTI corporation. The substrates were ultrasonically cleaned with acetone, isopropyl alcohol, and deionized water for 5 min each, followed by UV/ozone treatment for 15 min to remove residual carbon contamination. The substrates were loaded into the UHV system and then *in-situ* transferred to the ALD chamber for CoO deposition. The ALD system is a custom-built, hot-wall stainless steel rectangular 20 cm long chamber, with a reactor volume of 460 cm^3. Ultrahigh purity argon was used as a purge/carrier gas. The substrate temperature was monitored with a reference thermocouple in the ALD chamber that was previously calibrated against an instrumented wafer.

Bis(N-tert butyl, N'-ethylpropionamidinato) cobalt (II) (Strem, 98%) and deionized water were used as co-reactants for the ALD growth of CoO. During CoO growth, the Co precursor and water were held at 80 °C and room temperature (25 °C), respectively, while the substrate was maintained at a temperature range of 170–180 °C.

The water dosing was regulated using an in-line needle valve. Each cycle of CoO growth consisted of a 2-sec dose of Co, a 20-sec purge of Ar, a 1-sec dose of H_2O, and a 20-sec purge of Ar. The deposition of Al metal was performed in a customized DCA 600 MBE system with a base pressure of 5×10^{-9} Torr.[52] The deuterium gas and deuterium atom reduction were conducted in a custom-built vacuum chamber. Atomic D was generated by a 400-W Osram Xenophot bulb, which had part of the glass enclosure removed to expose the tungsten filament. A current of 5.2 A was supplied by a DC power supply (KEPCO, MSK10-10M) to the tungsten filament and the filament temperature was ~1800 K, as measured by a pyrometer. At this temperature, the tungsten filament can crack molecular deuterium to generate atomic deuterium.[53] The deuterium gas (Matheson, 99.999%) pressure was controlled by a leak valve. The sample was positioned approximately 4 cm above, and faced toward the tungsten filament. A pyrolytic boron nitride heater from Momentive was 2 cm above the sample. The sample temperature was monitored with a reference thermocouple in the vacuum chamber that was previously calibrated against an instrumented wafer.

X-ray reflectivity (XRR) and scanning electron microscopy (SEM) were used to determine the CoO film thicknesses and growth rate. XRR was conducted by a Panalytical X'PERT Pro diffractometer using a sealed tube Cu Kα radiation source (λ ~ 1.5406 Å) operating at 40 kV and 30 mA. SEM was conducted by a ZEISS Neon 40 SEM equipped with Bruker energy dispersive spectroscopy (EDS). The CoO film crystallinity and orientation were determined by *in-situ* reflection high energy electron diffraction (RHEED). RHEED was performed using a Staib Instruments RHEED gun

operated at 18 keV energy and 3° grazing incidence. An *in-situ* VG Scienta R3000 X-ray photoelectron spectroscopy (XPS) system with a monochromated Al Kα source at 1486.6 eV was used to determine film stoichiometry and composition, and the oxidation states of cobalt. The absolute energy scale of the analyzer on the XPS system is calibrated using a two-point measurement such that the Ag $3d_{5/2}$ core level at 368.26 eV and the Fermi edge of Ag at 0.0 eV. An *ex-situ* Veeco Icon atomic force microscopy (AFM) system is used to characterize the film morphology with tapping mode with Bruker TESPA AFM tips.

Magnetic property measurements were carried out with a Quantum Design physical property measurement system (PPMS) combined with vibrating sample magnetometry (VSM) option. Magnetization hysteresis loops were measured with the magnetic field applied parallel to the plane of the thin films. For all the measurements, the samples were at room temperature (25 °C).

3.3 RESULTS AND DISCUSSION

3.3.1 Growth of CoO on Amorphous SiO_2/Si and Single Crystal MgO(001) Substrates

Figure 3.1a shows the Co 2*p* X-ray photoelectron (XP) spectrum of 4.5 nm-thick CoO films grown on SiO_2/Si (red color) and on MgO(001) (blue color) at a temperature of 180 °C. All XPS peak positions were shifted by taking the CoO O 1*s* elemental peak to be at 530 eV. The binding energies of the main peaks are at 780.5 eV and 796.5 eV for Co $2p_{3/2}$ and Co $2p_{1/2}$ levels, respectively, and at 786.4 eV and 803.0 eV for the Co $2p_{3/2}$ and Co $2p_{1/2}$ for satellite peaks, respectively. The 2*p* binding energy position in conjunction with the very strong satellite at ~ 6 eV higher binding energy is consistent

with Co being in the +2 valence state with high spin.[54] Figures 3.1b and 3.1c show RHEED images of CoO thin films grown on SiO_2/Si and MgO(001) substrates, respectively. The centered-ring patterns (as shown in Figure 3.1b) indicate that the CoO thin films grown on SiO_2/Si have polycrystalline microstructure. The RHEED images in Figure 3.1c show clear dotted streaks, which means that the CoO films grown on single crystal MgO(001) are epitaxial with the underlying substrate and have some surface roughness. The growth rate of CoO was found to be ~ 0.3 Å/cycle on both SiO_2/Si and MgO(001) substrates.

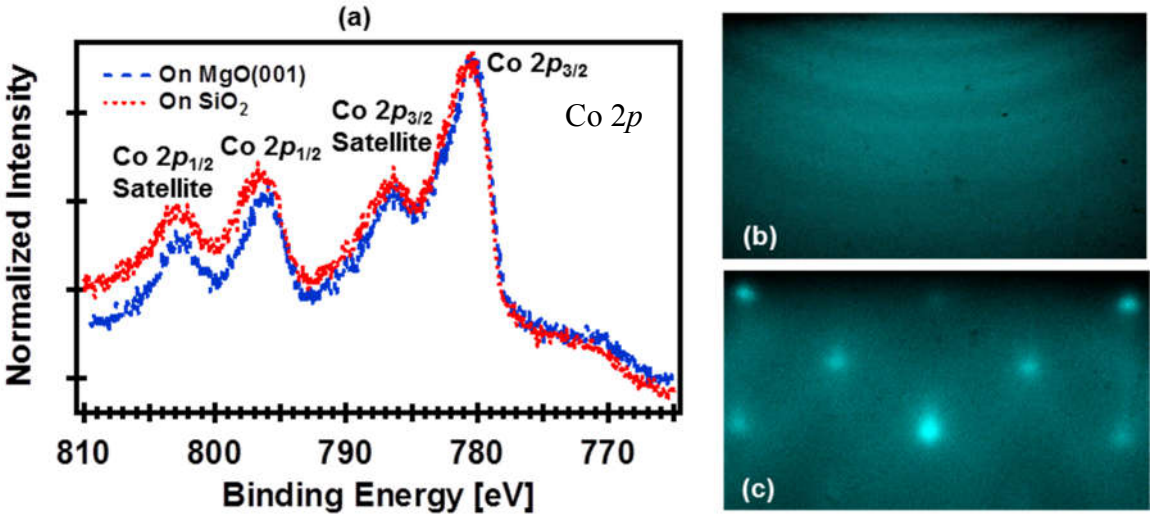

Figure 3.1. Co 2*p* XP spectrum of 4.5 nm-thick CoO films on SiO_2/Si and MgO(001) substrates grown by ALD at ~ 180 °C [Figure 3.1a (red color) and Figure 3.1a (blue color), respectively]. RHEED images of a 4.5 nm-thick CoO film grown on SiO_2/Si (Figure 3.1b) and a 4.5 nm-thick CoO film grown on MgO(001) (Figure 3.1c).

The formation of CoO films on SiO_2/Si and MgO(001) is observed over the 170–270 °C temperature range. At temperature higher than 305 °C, cobalt metal formation

was observed instead of CoO. Figure 3.2a displays Co 2*p* XP spectrum of 200-cycle CoO films grown at temperatures of 270 °C (black color), 305 °C (red color), and 345 °C (blue color). While the film grown at 270 °C still shows the presence of CoO, the films grown at 305 °C and 345 °C show the presence of Co metal. However, there is ~ 31 % carbon incorporated into the 305 °C and 345 °C cobalt films as estimated using XPS (Figure 3.3). The C 1*s* XPS intensity remains the same after a 15 min vacuum anneal at 500 °C (as shown in Figure 3.3b). This is different from the residual C (<2%) detected on the surface of as-deposited CoO films, which disappears after a slight vacuum anneal, as shown in Figure 3.3a. Carbon incorporation into Co films has also been reported using the same precursor [bis(N-tert butyl, N'-ethylpropionamidinato) cobalt (II)] and hydrogen as a reducing agent.[43,44] Figure 3.2b and 3.2c represent RHEED images of Co metal grown on the MgO(001) substrate at 345 °C and 305 °C, respectively. The ring-centered patterns shown in Figure 3.2b and 3.2c indicate that the thin Co films grown at 305 °C and 345 °C are polycrystalline on MgO(001). However, the spotted patterns are well-ordered meaning that the Co films have a certain orientation preference.

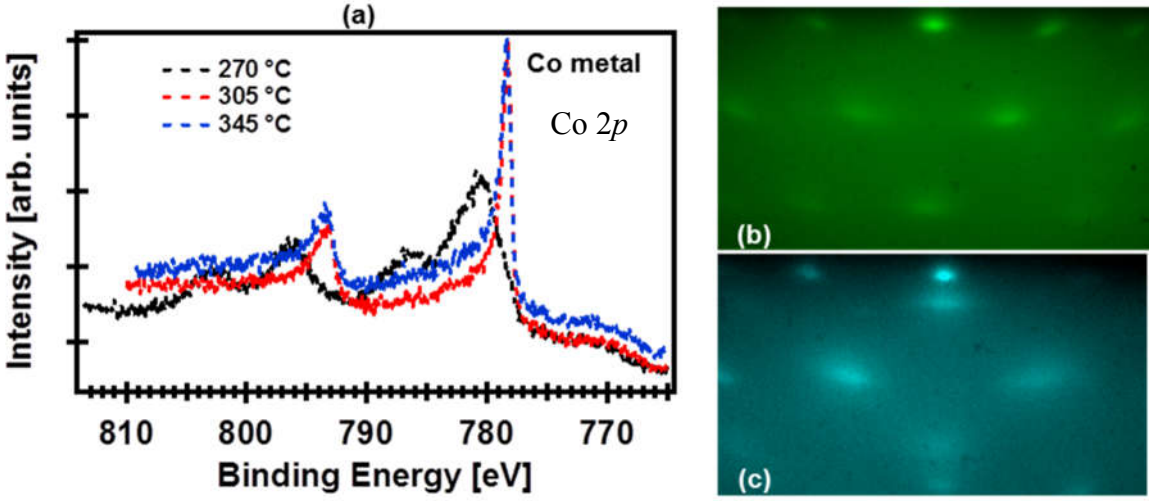

Figure 3.2. (a) Co 2*p* XP spectrum of 200-cycle CoO films grown on single crystal MgO(001) substrates by ALD at ~ 270 °C (black color), 305 °C (red color), and 345 °C (blue color). (b) and (c) are RHEED images of 200-cycle CoO films grown on MgO(001) by ALD at 345 °C and 305 °C, respectively.

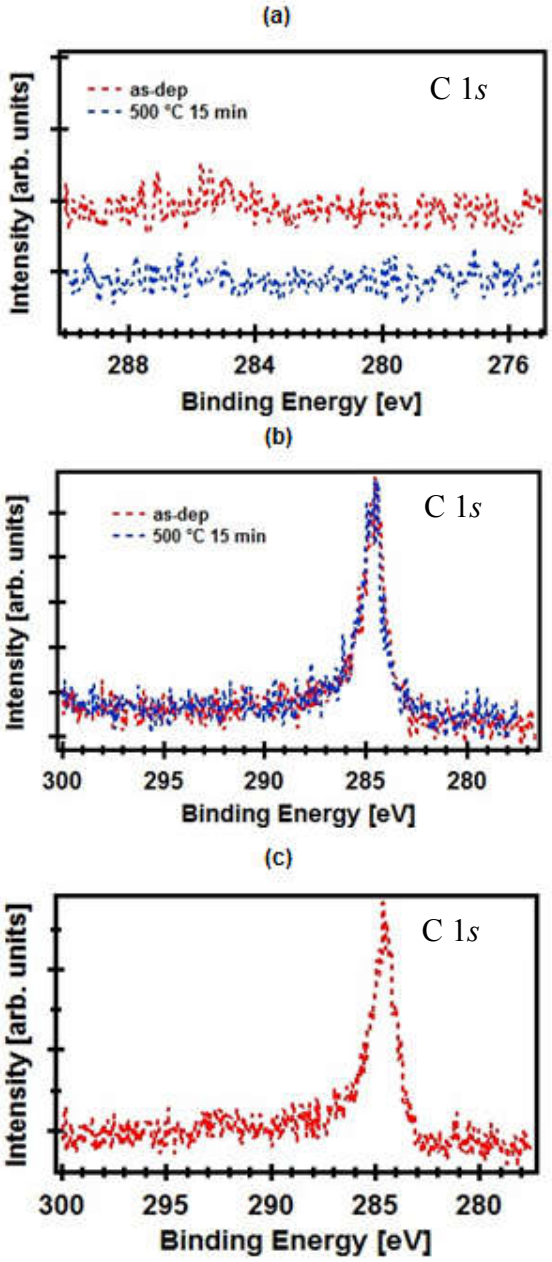

Figure 3.3. (a) C 1*s* XP spectrum of a 200-cycle CoO film grown on MgO(001) by ALD at 270 °C as-deposited (red color) and after a 15 min vacuum anneal at 500 °C (blue color). (b) C 1*s* XP spectrum of a 200-cycle CoO film grown on MgO(001) by ALD at 305 °C as-deposited (red color) and after a 15 min vacuum anneal at 500 °C (blue color). (c) C 1*s* XP spectrum of an as-deposited 200-cycle CoO film grown on MgO(001) by ALD at 345 °C.

3.3.2 Transformation of CoO to Co Spinel, Co_3O_4

The CoO oxidized to form Co_3O_4 in air upon being exposed to mercury ultraviolet (Hg UV) light with a wavelength of ~ 200 nm for 30 min. Figure 3.4a presents the Co 2*p* XP spectrum of a 4.5 nm-thick CoO film grown on an MgO(001) substrate at 180 °C. The as-deposited CoO film was removed from the ultra-high vacuum system and exposed to Hg UV light for 30 min at room temperature. The film was then reloaded into the analysis system and characterized by XPS and RHEED. The blue color in Figure 3.4a represents the Co 2*p* XP spectrum of the film after Hg UV light exposure, which shows strongly suppressed shake-up satellite peaks at 786.4 eV and 803.0 eV indicating the formation of Co_3O_4.[55] Figure 3.4b confirms the crystalline quality of the 4.5 nm-thick CoO film grown on MgO(001) with bright streaks along with clear Kikuchi lines. After exposing the CoO film to Hg UV light, extra streaks appear in between the original CoO streaks (Figure 3.4c) indicating that the in-plane lattice constant of the new cobalt oxide structure is twice as that of the CoO in-plane lattice constant. This is consistent with the cobalt spinel XPS data and consistent with the lattice constant of both CoO and Co_3O_4.[56,57] The formation of epitaxial Co_3O_4 from epitaxial CoO films may motivate further studies on Co_3O_4 for catalytic applications.

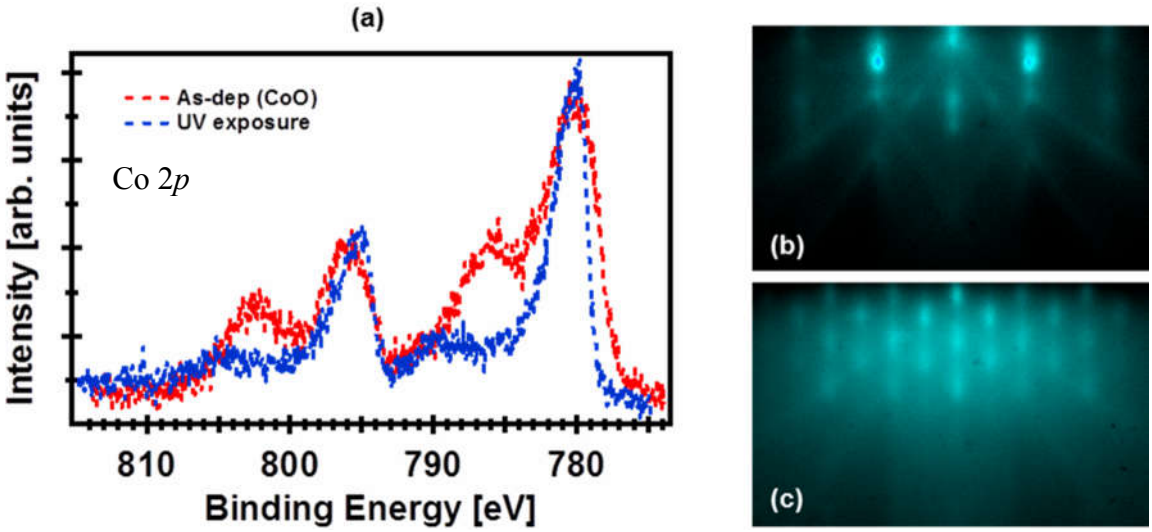

Figure 3.4. (a) Co 2*p* XP spectrum of a 4.5 nm-thick as-deposited CoO film on MgO(001) substrate grown by ALD at 180 °C (red color) and the CoO film after exposed to Hg UV light for 30 min at room temperature (blue color). (b) and (c) are RHEED images of the as-deposited CoO and the film after 30 min Hg UV light exposure at room temperature, respectively.

3.3.3 Transformation of CoO to Co Metal

Figure 3.5a shows the Co 2*p* XP spectrum of a Co film after deuterium gas reduction on 4.5 nm-thick CoO grown on SiO_2/Si. The D_2 reduction was conducted at 420 °C with $P_{D_2} = 1 \times 10^{-3}$ torr for 30 min. 420 °C is approximately the threshold temperature at which the reduction occurs in our experimental apparatus. After reduction, the binding energies of the main peaks are 778.1 eV and 793.2 eV for Co $2p_{3/2}$ and Co $2p_{1/2}$ levels, respectively, which agrees with the peaks of Co metal.[58] There is a shoulder peak at 780.5 eV, which means there is still some CoO in the film. Based on peak fitting of the Co $2p_{3/2}$ peak against that of CoO and metallic Co, it is concluded that the film contains 98% Co and 2% CoO. Figure 3.5b and 3.5c present AFM images of the CoO

film before reduction and the Co film after the D_2 reduction, respectively. Based on the comparison of the two AFM images, we can clearly see that the continuous before-reduction film (R_{rms} = 0.42 nm) became rough and discontinuous after reduction (R_{rms} = 3.66 nm) (The R_{rms} of SiO_2/Si substrate is 0.351 nm as a reference). This dewetting phenomenon is common in high temperature processing of metals,[48–51] but it is undesired when continuous Co films are required. Due to the absence of capping layer, Co film reoxidized after exposure to ambient environment, as shown in Figure 3.6a. There was mainly metallic cobalt in the film before taking out the film from UHV system (red color). Most of the cobalt reoxidized after 4 h air exposure confirmed by the shift of Co $2p_{3/2}$ main peak from 778.1 eV to 780.5 eV (blue color), which means the bare Co film in the ambient environment present for AFM measurement was in CoO status actually.

As a reference, we deposited a 2-nm MBE Al capping layer on a D_2 gas-reduced 4.5 nm-thick CoO sample, and characterized the film morphology. This metallic Al layer (~73 eV in red color) oxidized to Al_2O_3 capping layer (~75 eV in blue color) upon exposure to the ambient environment, as shown in Figure 3.6b. This capping layer is effective in protecting Co film from reoxidizing. The film was still mainly of metallic cobalt after 48 h air exposure (blue color), as shown in Figure 3.6c. This assures the capped Co film was indeed in Co status during AFM measurement. Figure 3.7a is the AFM image of the Al_2O_3 (2 nm Al)/Co (reduced by D_2 gas)/SiO_2/Si sample. Figure 3.5c shows the Co film produced by D_2 gas reduction has the R_{rms} of 3.66 nm before depositing 2-nm MBE Al, while Figure 3.7a shows its R_{rms} becomes 3.50 nm after

depositing 2-nm MBE Al. This comparison indicates that the morphology of the reoxidized CoO film (Figure 3.5c) is similar to reduced Co film.

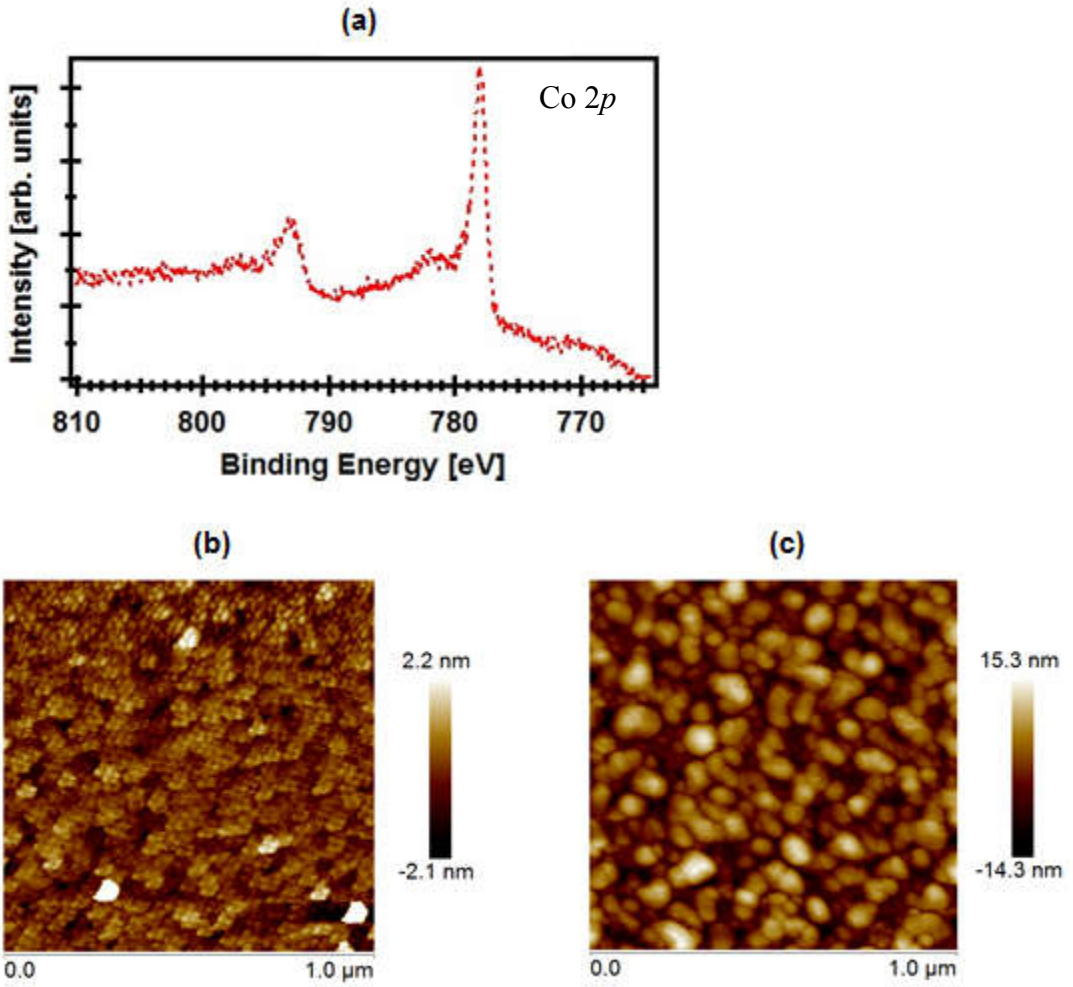

Figure 3.5. (a) Co 2*p* XP spectrum of a Co film after a 30 min deuterium gas reduction at 420 °C on 4.5 nm-thick CoO on SiO_2/Si substrate. (b) and (c) are AFM images of the as-deposited CoO film (R_{rms} = 0.42 nm) and the Co film after 30 min deuterium gas reduction at 420 °C (R_{rms} = 3.66 nm), respectively.

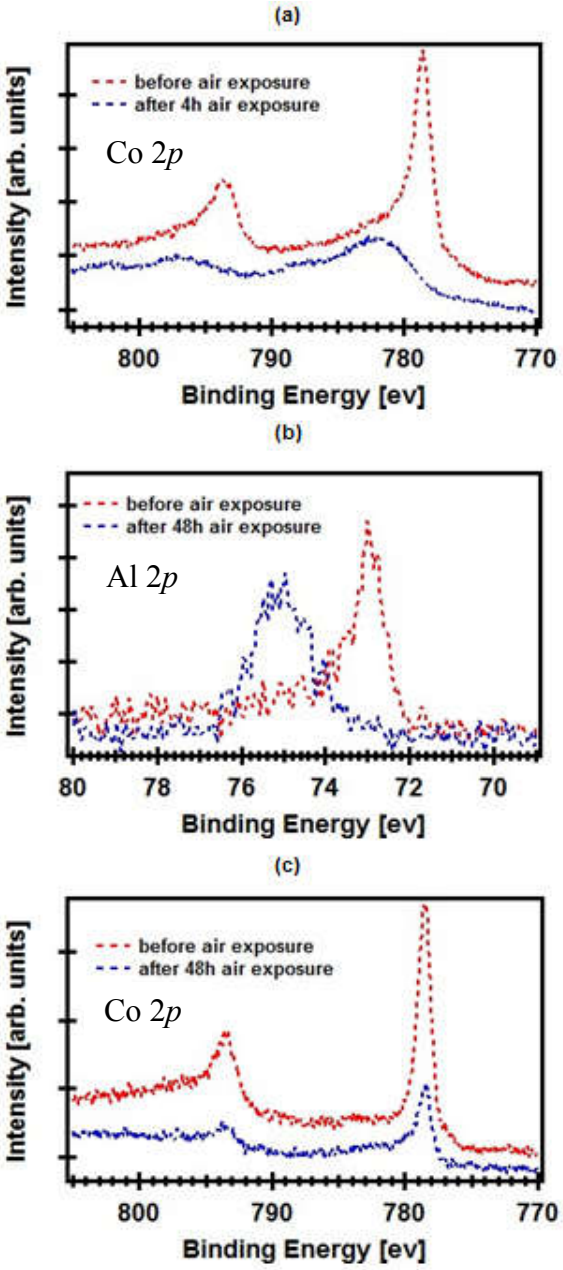

Figure 3.6. (a) Co 2*p* XP spectrum of a D_2 gas-reduced Co sample before air exposure (red color) and after 4 h air exposure (blue color). (b) Al 2*p* XP spectrum of a D_2 gas-reduced Co sample with 2 nm MBE Al capping layer before air exposure (red color) and after 48 h air exposure (blue color). (c) Co 2*p* XP spectrum of a D_2 gas-reduced Co sample with 2 nm MBE Al capping layer before air exposure (red color) and after 48 h air exposure (blue color).

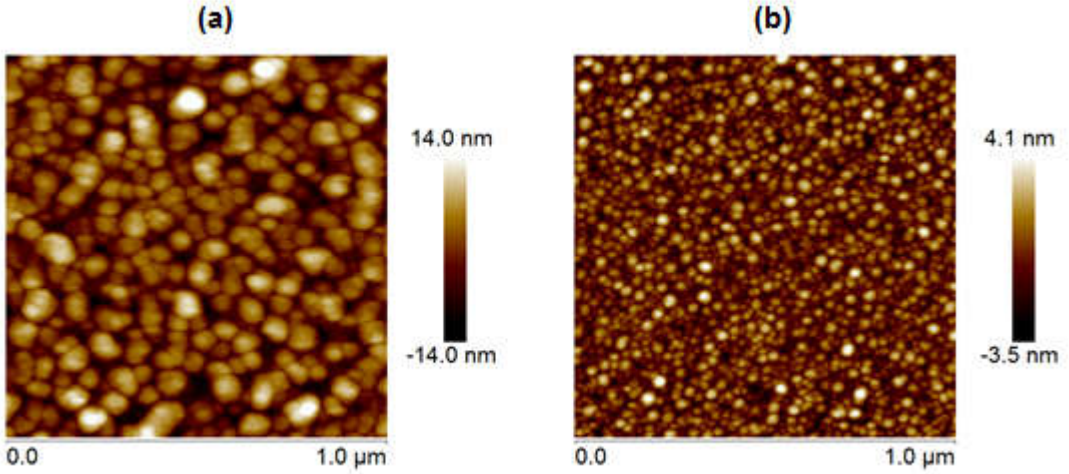

Figure 3.7. (a) and (b) are AFM images of the Al_2O_3 (2 nm Al)/Co (reduced by D_2 gas at 420 °C)/SiO_2/Si heterostructure (R_{rms} = 3.50 nm), and the Al_2O_3 (2 nm Al)/Co (reduced by D atom at 220°C)/SiO_2/Si heterostructure (R_{rms} = 0.86 nm), respectively.

To attenuate dewetting and produce smooth and continuous Co metal films we studied two low temperature reduction processes, D atom reduction and use of an O scavenger layer. D atom is more reactive than D_2 gas, therefore in principle the threshold temperature for CoO reduction by D atom should be lower than that by D_2 gas.[59] We did a series of CoO reduction studies with D atom exposure at different temperatures with $P_{D_2} = 1 \times 10^{-5}$ torr for 30 min and found that the threshold temperature is about 220 °C in our experimental apparatus. Figure 3.8a shows the Co 2*p* XP spectrum of the Co film after D atom reduction of 4.5 nm-thick CoO film grown on SiO_2/Si. The D atom reduction step was conducted at 220 °C with $P_{D_2} = 1 \times 10^{-5}$ torr for 30 min. The binding energies of the main peaks are 778.1 eV and 793.2 eV for the Co $2p_{3/2}$ and Co $2p_{1/2}$ levels, and

there is no shoulder peak at 780.5 eV, which means 100% of CoO has been reduced to Co metal. Figure 3.8b shows the C 1*s* XP spectrum of the Co metal film produced by D atom reduction, from which we can conclude there is no carbon incorporation in the film. Figure 3.8c is the AFM image of the Co metal film produced by D atom reduction. The R_{rms} of the film after reduction is 0.70 nm, which is in the same order of the R_{rms} (0.42 nm) of the CoO film before reduction. Besides, it can be seen that the Co metal film is continuous. We also deposited a 2-nm MBE Al capping layer on a D atom-reduced 4.5 nm-thick CoO sample, and characterize the film morphology. Figure 3.7b is the AFM image of the Al_2O_3 (2 nm Al)/Co (reduced by D atom)/SiO_2/Si sample. Figure 3.8c shows the Co film produced by D atom reduction has the R_{rms} of 0.7 nm before depositing 2-nm MBE Al, while Figure 3.7b shows its R_{rms} becomes 0.86 nm after depositing 2-nm MBE Al. This comparison further confirms that the morphology of reoxidized CoO film is similar to reduced Co film.

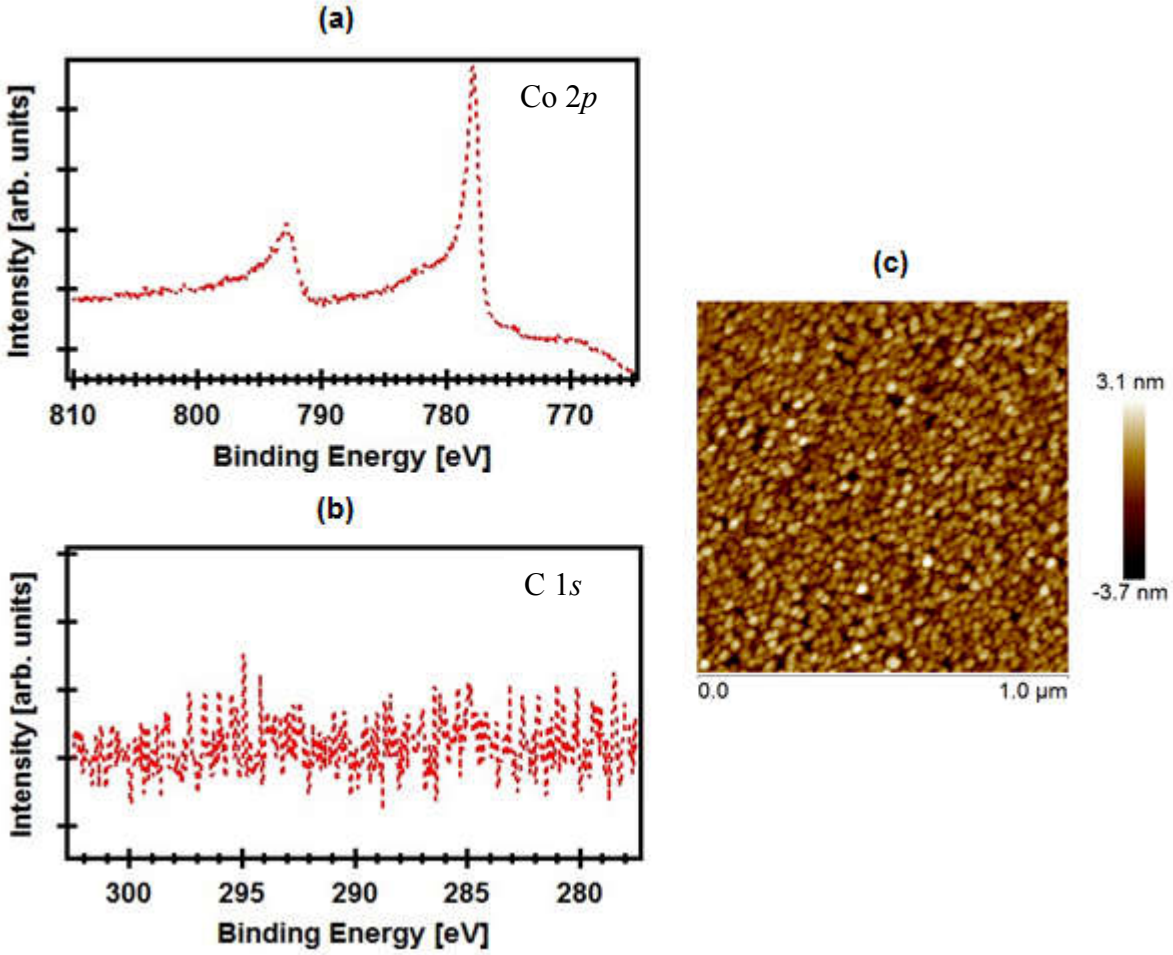

Figure 3.8. (a) and (b) are Co 2*p* XP spectrum and C 1*s* XP spectrum of the Co film after a 30 min deuterium atom reduction at 220 °C on 4.5 nm-thick CoO on SiO_2/Si substrate, respectively. (c) AFM image of the Co film after 30 min deuterium atom reduction at 220 °C on 4.5 nm-thick CoO on SiO_2/Si substrate (R_{rms} = 0.70 nm).

This observation is further confirmed by the similar results of the reductions of CoO on MgO(001) substrates (R_{rms} is 0.18 nm). Figure 3.9a represent the morphology of as-deposited 4.5 nm-thick CoO films on MgO(001) and the film roughness is 0.52 nm. After a 30 min D_2 gas reduction at 500 °C with $P_{D_2} = 1 \times 10^{-3}$ torr, the resulting Co

film reveals the serious dewetting problem and CoO film become disconnected islands, as shown in Figure 3.9b. While after a 30 min D atom reduction of CoO at 250 °C with $P_{D_2} = 1 \times 10^{-5}$ torr, the resulting Co films are still continuous with roughness at 0.90 nm, as shown in Figure 3.9c.

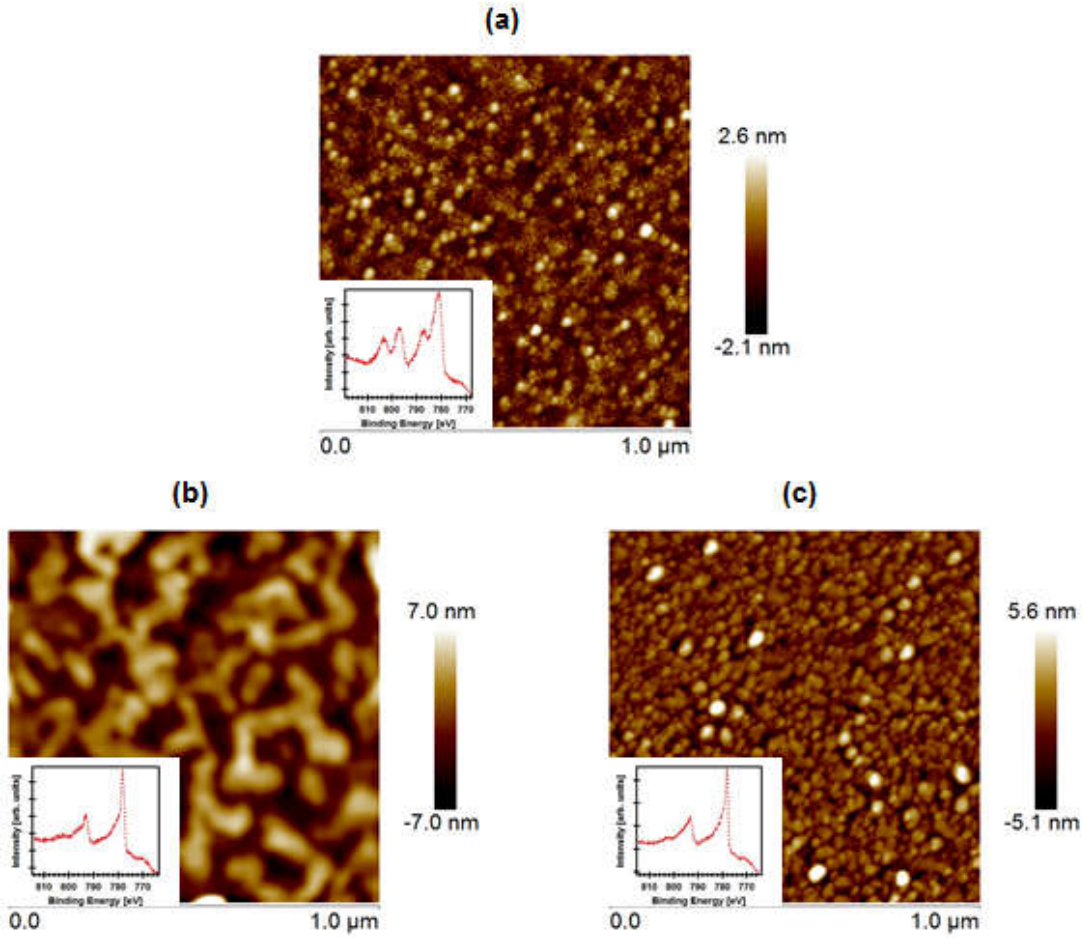

Figure 3.9. (a) AFM image of an as-deposited 4.5 nm-thick CoO film grown on MgO(001) by ALD at 180 °C (R_{rms} = 0.52 nm). (b) AFM image of the Co film after a 30 min deuterium gas reduction at 500 °C on 4.5 nm-thick CoO on MgO(001) (R_{rms} = 2.03 nm). (c) AFM image of the Co film after a 30 min deuterium atom reduction at 250 °C on 4.5 nm-thick CoO on MgO(001) (R_{rms} = 0.90 nm). The inserts are the Co 2*p* XP spectra of the corresponding films in each figure.

Our previous study showed that CoO films grew epitaxially on $SrTiO_3$-buffered Si(001) at temperature of 170–190 °C using ALD.[2] The as-deposited CoO films had some residual carbon contamination (<2%), which disappeared after a slight vacuum anneal. During the vacuum anneal at 500 °C, the heterostructure CoO/$SrTiO_3$ (1.6 nm)/Si produced Co metal species due to the reaction between CoO and Sr.[2] Based on this observation, we explored a chemical method to form carbon-free Co films by reducing ALD-grown CoO films. We capped the CoO with metals that have a high affinity for oxidation, such as Al, which reacted with oxygen from CoO and formed a capping oxide on the Co metal film.

A 4.5 nm-thick CoO is grown on SiO_2/Si substrate by ALD at 180 °C and the sample was then *in-situ* transferred to the MBE chamber where a 3 nm-thick Al metal was deposited on it at the substrate temperature of 200 °C, of which Co 2*p* XP spectrum is shown in Figure 3.10a. The choice of 3 nm as the Al layer thickness is based on complete reduction of CoO and enough capping effects against air that are discussed above herein. The binding energies of the Co $2p_{3/2}$ peak at 778.1 eV and the Co $2p_{1/2}$ peak at 793.2 eV confirm the film is of metallic cobalt instead of cobalt oxide.[54] This suggests that the Al reacts with CoO to form Al_2O_3 and Co. The ΔG_r^0 (298 K) of the reaction between 3 mol CoO and 2 mol Al is -939.8 kJ/mol,[60] which means that the reaction is favored even at room temperature. The reaction between Al and CoO is also demonstrated by the Al 2*p* XP spectrum as shown in Figure 3.10b. The small peak at a binding energy of ~ 73 eV is for Al metal, while the larger peak at a binding energy of ~

75 eV is for Al_2O_3.[61] The existence of Al metal after reaction indicates the complete reduction of CoO. There is a minor peak at a binding energy of ~ 73.6 eV, which agrees with the Al 2*p* peak position of $CoAl_2O_4$.[62] This indicates the formation of $CoAl_2O_4$ inter-layer. The formation of $CoAl_2O_4$ inter-layer is also observed in literature when there is diffusion between Co and Al_2O_3.[63] Figure 3.10c shows the morphology of this Al_2O_3 (3 nm Al)/Co/SiO_2/Si sample, from which we can see the R_{rms} is 0.83 nm and the Co film is continuous.

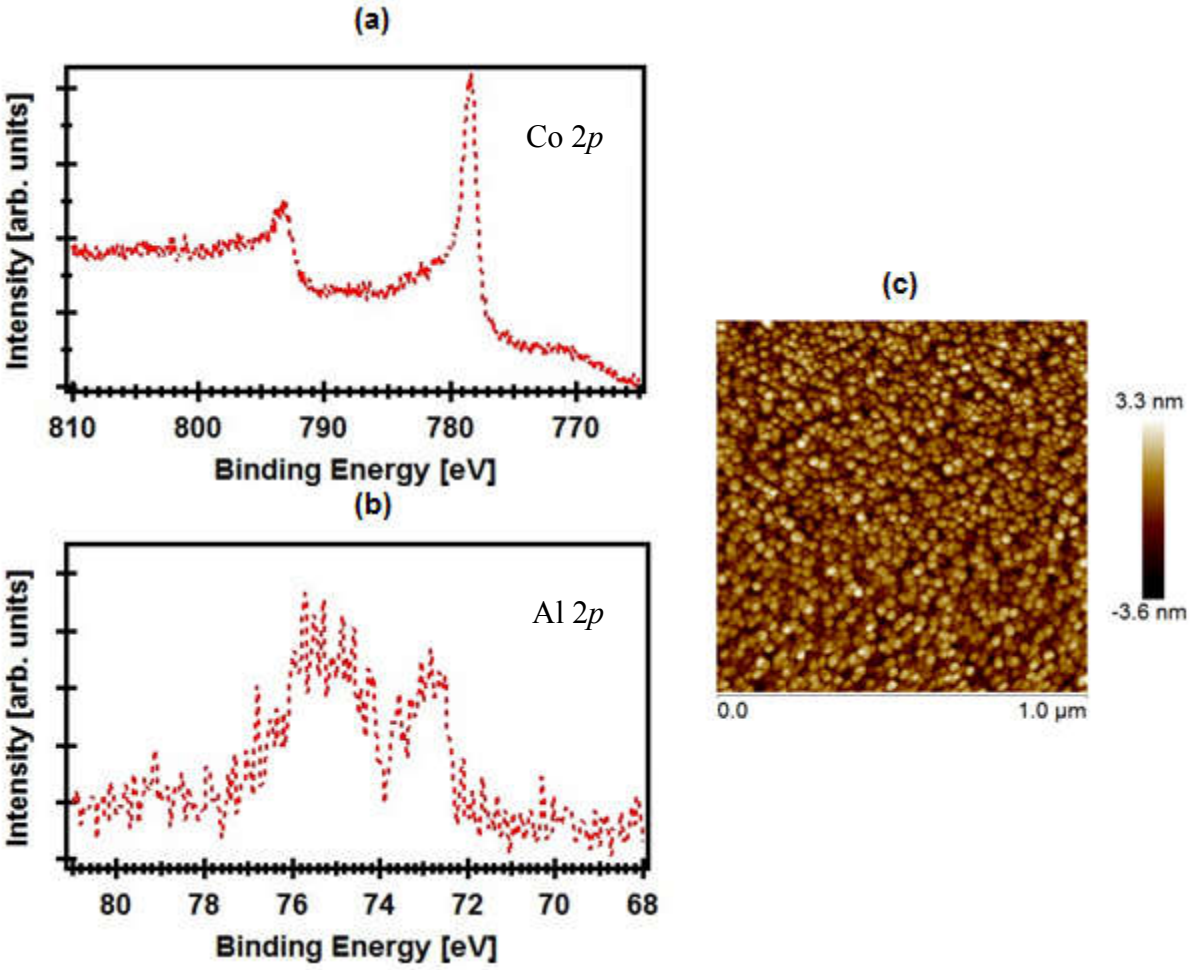

Figure 3.10. (a) Co 2*p* XP spectrum of an as-deposited 4.5 nm-thick CoO film on SiO_2/Si grown by ALD at 180 °C (red color) and the film after a deposition of 3 nm-thick MBE Al on the CoO/SiO_2/Si (blue color). (b) Al 2*p* XP spectrum of the film after a deposition of 3 nm-thick MBE Al on the CoO/SiO_2/Si. (c) AFM image of the Al_2O_3 (3nm Al)/Co/SiO_2/Si heterostructure (R_{rms} = 0.83 nm).

Figure 3.11a, 3.11b and 3.11c display the magnetization hysteresis loops of Samples A, B, and C, respectively, as a function of magnetic field applied parallel to the substrates. All the measurements were conducted within one day after the samples were removed from the UHV system and the Co films stayed reduced when they were

measured. Sample A is a 4.5 nm CoO grown on SiO_2/Si and then reduced by D_2 gas at 420 °C and finally covered by 2-nm MBE Al capping layer. Sample B is a 4.5 nm CoO grown on SiO_2/Si and then reduced by atomic D at 220 °C and finally covered by 2-nm MBE Al capping layer. Sample C is a 4.5 nm CoO grown on SiO_2/Si and then reduced by 3-nm MBE Al capping layer at 200 °C. The measured sample sizes and saturated moments of the three samples are listed in Table 3.1.

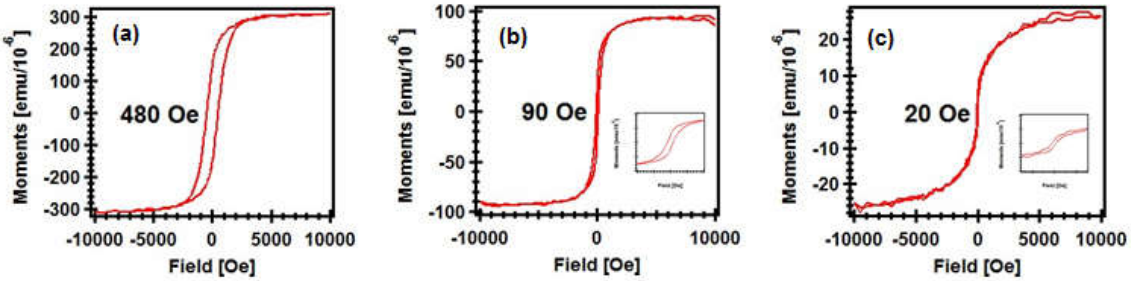

Figure 3.11. (a), (b), (c) are the magnetization hysteresis loops of Samples A, B, C measured by VSM, respectively. The magnetic field is applied parallel to the plane of the thin films. The inserted figures in (b) and (c) are enlarged corresponding loops around zero field. The x axis range of the inserted figure in (b) is from -1000 Oe to 1000 Oe. And the x axis range of the inserted figure in (c) is from -300 Oe to 300 Oe. All the data have been corrected with the cancellation of the base signal of substrates and capping layers.

	Production method	Sample size (mm)	Saturated moment (emu)	Saturation magnetization (emu/cm^3)	Coer-civity (Oe)
A	4.5 nm CoO grown on SiO_2/Si, then is reduced by D_2 gas at 420 °C, finally 2 nm MBE Al deposited as a capping layer.	10×5	3.05×10^{-4}	2033	480
B	4.5 nm CoO grown on SiO_2/Si, then is reduced by atomic D at 220 °C, finally 2 nm MBE Al deposited as a capping layer.	8×2.5	9.2×10^{-5}	1533	90
C	4.5 nm CoO grown on SiO_2/Si, then is reduced by a 3 nm MBE Al capping layer at 200 °C.	9×2.5	2.6×10^{-5}	385	20

Table 3.1. Descriptions of the three reduced Co samples measured by VSM.

Due to the existence of Al_2O_3 capping layer, almost all of the Co films stayed reduced when meaured by VSM. Based on comparison between Figure 3.1a and Figure 3.8a, there is about 31% peak area contraction of Co $2p_{3/2}$ from CoO to Co, which means there should be about 31% volume contraction. It is reasonable to assume the Co layer thickness after complete reduction of 4.5 nm-thick CoO film as 3 nm, and therefore the measured saturation magnetization of Sample A, B, C are 2033 emu/cm^3, 1533 emu/cm^3, 385 emu/cm^3, respectively. While the measured saturation magnetization of Sample A and B is close to the saturation magnetization of bulk cobalt at 1420 emu/cm^3,[64] Sample C has a much smaller value. One possible reason for the smaller saturation magnetization of the cobalt film produced by the 3-nm MBE Al layer reduction is that there is existence of $CoAl_2O_4$ inter-layer as we discussed above and therefore the Co layer thickness is greatly reduced.

The measured coercivity of Samples A, B and C is 480 Oe, 90 Oe and 20 Oe, respectively. The two samples, B and C, produced by low temperature reduction processes have much smaller coercivity than the sample A which is produced by high temperature D_2 gas reduction. This may be explained by potential fewer voids in the continuous cobalt films produced by low temperature reduction processes than that in the rough and discontinuous cobalt films produced by the high temperature reduction process.[65] The difference between the coercivity of the cobalt film produced by D atom reduction and the coercivity of the cobalt film produced by oxygen scavenger layer reduction may come from the presence of the potential diffusion induced $CoAl_2O_4$ inter-layer. The deterioration of the coercivity due to the diffusion induced interface layer is demonstrated in a hard/soft multilayer in literature.[66] Further studies are being conducted to explore the microstructure and the magnetic properties of the reduced Co films and the ability to tune them. It has been found that several parameters of the D atom reduction process affect the microstructure and the magnetic properties of the resulting Co films. Elucidation of the process-structure-magnetic property relationship will be reported in future work to realize specific properties for various applications.

3.4 CONCLUSIONS

We report the growth of carbon-free CoO on SiO_2/Si and MgO(001) substrates by ALD in a temperature range of 170–270 °C. While the CoO films grown on SiO_2/Si are polycrystalline, the CoO films grown on single crystal MgO(001) are crystalline and epitaxial. The transformation of crystalline CoO to crystalline Co_3O_4 is observed by

exposing CoO films to Hg UV light at room temperature. While high temperature thermal reduction of CoO causes dewetting problem, we demonstrate that the reduction of CoO forms smooth and continuous carbon-free Co metal film by two low temperature processes, using deuterium atom as reducing agent or using Al metal overlayer as oxygen scavenger. The cobalt films produced by the low temperature reduction processes have smaller coercivity than the cobalt films produced by high temperature thermal reduction.

3.5 REFERENCES

1. Ling, T. *et al.* Engineering surface atomic structure of single-crystal cobalt (II) oxide nanorods for superior electrocatalysis. *Nat. Commun.* **7,** 12876 (2016).
2. Ngo, T. Q. *et al.* Atomic layer deposition of photoactive CoO/SrTiO3 and CoO/TiO2 on Si(001) for visible light driven photoelectrochemical water oxidation. *J. Appl. Phys.* **114,** 84901 (2013).
3. Yang, J. *et al.* Efficient and Sustained Photoelectrochemical Water Oxidation by Cobalt Oxide/Silicon Photoanodes with Nanotextured Interfaces. *J. Am. Chem. Soc.* **136,** 6191–6194 (2014).
4. Li, W. Y., Xu, L. N. & Chen, J. Co3O4 Nanomaterials in Lithium-Ion Batteries and Gas Sensors. *Adv. Funct. Mater.* **15,** 851–857 (2005).
5. Yu, X.-Y. *et al.* Facet-dependent electrochemical properties of Co_3O_4 nanocrystals toward heavy metal ions. *Sci. Rep.* **3,** 2886 (2013).
6. Liang, Y. *et al.* Co_3O_4 nanocrystals on graphene as a synergistic catalyst for oxygen reduction reaction. *Nat. Mater.* **10,** 780–786 (2011).
7. Natile, M. M. & Glisenti, A. Study of Surface Reactivity of Cobalt Oxides: Interaction with Methanol. *Chem. Mater.* **14,** 3090–3099 (2002).
8. Kormondy, K. J. *et al.* Epitaxy of polar semiconductor Co3O4 (110): Growth, structure, and characterization. *J. Appl. Phys.* **115,** 243708 (2014).
9. Vaz, C. A. F. *et al.* Interface and electronic characterization of thin epitaxial Co3O4 films. *Surf. Sci.* **603,** 291–297 (2009).
10. Vaz, C. A. F., Altman, E. I. & Henrich, V. E. Exchange bias and interface electronic structure in Ni/Co3O4 (011). *Phys. Rev. B* **81,** 104428 (2010).

11. Qiao, L. *et al.* Nature of the band gap and origin of the electro-/photo-activity of Co3O4. *J. Mater. Chem. C* **1,** 4628–4633 (2013).

12. Kennedy, R. J. The growth of iron oxide, nickel oxide and cobalt oxide thin films by laser ablation from metal targets. *IEEE Trans. Magn.* **31,** 3829–3831 (1995).

13. Shalini, K., Mane, A. U., Shivashankar, S. A., Rajeswari, M. & Choopun, S. Epitaxial growth of Co3O4 films by low temperature, low pressure chemical vapour deposition. *J. Cryst. Growth* **231,** 242–247 (2001).

14. Fujii, E., Torii, H., Tomozawa, A., Takayama, R. & Hirao, T. Preparation of cobalt oxide films by plasma-enhanced metalorganic chemical vapour deposition. *J. Mater. Sci.* **30,** 6013–6018 (1995).

15. Mane, A. U., Shalini, K., Wohlfart, A., Devi, A. & Shivashankar, S. A. Strongly oriented thin films of Co3O4 deposited on single-crystal MgO(100) by low-pressure, low-temperature MOCVD. *J. Cryst. Growth* **240,** 157–163 (2002).

16. Klepper, K. B., Nilsen, O. & Fjellvåg, H. Growth of thin films of Co3O4 by atomic layer deposition. *Thin Solid Films* **515,** 7772–7781 (2007).

17. Donders, M. E., Knoops, H. C. M., Van, M. C. M., Kessels, W. M. M. & Notten, P. H. L. Remote Plasma Atomic Layer Deposition of Co3O4 Thin Films. *J. Electrochem. Soc.* **158,** G92–G96 (2011).

18. Klepper, K. B., Nilsen, O. & Fjellvåg, H. Epitaxial growth of cobalt oxide by atomic layer deposition. *J. Cryst. Growth* **307,** 457–465 (2007).

19. Diskus, M., Nilsen, O. & Fjellvåg, H. Thin Films of Cobalt Oxide Deposited on High Aspect Ratio Supports by Atomic Layer Deposition. *Chem. Vap. Depos.* **17,** 135–140 (2011).

20. Kokaze, Y. *et al.* Performance of Integrated Cu Gap-Filling Process with Chemical Vapor Deposition Cobalt Liner. *Jpn. J. Appl. Phys.* **52,** 05FA01 (2013).

21. Kohn, A., Eizenberg, M. & Shacham-Diamand, Y. Copper grain boundary diffusion in electroless deposited cobalt based films and its influence on diffusion barrier integrity for copper metallization. *J. Appl. Phys.* **94,** 3015–3024 (2003).

22. R. G. Gordon, H. Kim & H. Bhandari. Cobalt nitride layers for copper interconnects and methods for forming them. (2011).

23. Aubel, O. *et al.* Backend-of-line reliability improvement options for 28nm node technologies and beyond. in *2011 IEEE International Interconnect Technology Conference* 1–3 (2011).

24. Barraud, C. *et al.* Unidirectional Spin-Dependent Molecule-Ferromagnet Hybridized States Anisotropy in Cobalt Phthalocyanine Based Magnetic Tunnel Junctions. *Phys. Rev. Lett.* **114,** 206603 (2015).

25. Kim, W., Kim, K., Parkin, S. S. P., Jeong, J. & Samant, M. G. Magnetic memory device having cobalt-iron-beryllium magnetic layers. (2017).

26. Yuasa, S. & Djayaprawira, D. D. Giant tunnel magnetoresistance in magnetic tunnel junctions with a crystalline MgO(0 0 1) barrier. *J. Phys. Appl. Phys.* **40,** R337 (2007).

27. Ikeda, S. *et al.* A perpendicular-anisotropy CoFeB–MgO magnetic tunnel junction. *Nat. Mater.* **9,** 721–724 (2010).

28. K. M. Wu, K. W. Cheng, C. Y. Tsai & C. S. Tsai. Magnetoresistive random access memory cell and fabricating the same. (2015).

29. Wang, Z. *et al.* Atomic-Scale Structure and Local Chemistry of CoFeB–MgO Magnetic Tunnel Junctions. *Nano Lett.* **16,** 1530–1536 (2016).

30. Schmidt, D. *et al.* Optical, structural, and magnetic properties of cobalt nanostructure thin films. *J. Appl. Phys.* **105,** 113508 (2009).

31. Bergenti, I. *et al.* Magnetic properties of Cobalt thin films deposited on soft organic layers. *J. Magn. Magn. Mater.* **316,** e987–e989 (2007).

32. Presa, B. *et al.* Morphological and magnetic properties of Co nanoparticle thin films grown on Si3N4. *J. Appl. Phys.* **102,** 53901 (2007).

33. Zimmermann, C. G. *et al.* Burrowing of Co Nanoparticles on Clean Cu and Ag Surfaces. *Phys. Rev. Lett.* **83,** 1163–1166 (1999).

34. Tang, F. *et al.* Magnetic properties of Co nanocolumns fabricated by oblique-angle deposition. *J. Appl. Phys.* **93,** 4194–4200 (2003).

35. Deo, N., Bain, M. F., Montgomery, J. H. & Gamble, H. S. Study of magnetic properties of thin cobalt films deposited by chemical vapour deposition. *J. Mater. Sci. Mater. Electron.* **16,** 387–392 (2005).

36. George, S. M. Atomic Layer Deposition: An Overview. *Chem. Rev.* **110,** 111–131 (2010).

37. Lee, H.-B.-R. & Kim, H. High-Quality Cobalt Thin Films by Plasma-Enhanced Atomic Layer Deposition. *Electrochem. Solid-State Lett.* **9,** G323–G325 (2006).

38. Lee, H.-B.-R. & Kim, H. Area Selective Atomic Layer Deposition of Cobalt Thin Films. *ECS Trans.* **16,** 219–225 (2008).

39. Lee, H.-B.-R. *et al.* High Quality Area-Selective Atomic Layer Deposition Co Using Ammonia Gas as a Reactant. *J. Electrochem. Soc.* **157,** D10–D15 (2010).

40. Kim, K. *et al.* Comparison of Co Films Deposited by Remote Plasma Atomic Layer Deposition Method with Cyclopentadienylcobalt Dicarbonyl [CpCo(CO)2] and Dicobalt Octacarbonyl [Co2(CO)8]. *Jpn. J. Appl. Phys.* **46,** L173 (2007).

41. Yoon, J. *et al.* Atomic Layer Deposition of Co Using N2/H2 Plasma as a Reactant. *J. Electrochem. Soc.* **158,** H1179–H1182 (2011).

42. Park, J. *et al.* Plasma-enhanced atomic layer deposition of Co using Co(MeCp)2 precursor. *J. Energy Chem.* **22,** 403–407 (2013).

43. Elko-Hansen, T. D.-M. & Ekerdt, J. G. XPS Investigation of the Atomic Layer Deposition Half Reactions of Bis(N-tert-butyl-N′-ethylpropionamidinato) Cobalt(II). *Chem. Mater.* **26,** 2642–2646 (2014).

44. Elko-Hansen, T. D.-M., Dolocan, A. & Ekerdt, J. G. Atomic Interdiffusion and Diffusive Stabilization of Cobalt by Copper During Atomic Layer Deposition from Bis(N-tert-butyl-N′-ethylpropionamidinato) Cobalt(II). *J. Phys. Chem. Lett.* **5,** 1091–1095 (2014).

45. Kwon, J., Saly, M., Halls, M. D., Kanjolia, R. K. & Chabal, Y. J. Substrate Selectivity of (tBu-Allyl)Co(CO)3 during Thermal Atomic Layer Deposition of Cobalt. *Chem. Mater.* **24,** 1025–1030 (2012).

46. Kalutarage, L. C., Martin, P. D., Heeg, M. J. & Winter, C. H. Volatile and Thermally Stable Mid to Late Transition Metal Complexes Containing α-Imino Alkoxide Ligands, a New Strongly Reducing Coreagent, and Thermal Atomic Layer Deposition of Ni, Co, Fe, and Cr Metal Films. *J. Am. Chem. Soc.* **135,** 12588–12591 (2013).

47. Klesko, J. P., Kerrigan, M. M. & Winter, C. H. Low Temperature Thermal Atomic Layer Deposition of Cobalt Metal Films. *Chem. Mater.* **28,** 700–703 (2016).

48. Thompson, C. V. Solid-State Dewetting of Thin Films. *Annu. Rev. Mater. Res.* **42,** 399–434 (2012).

49. Lee, J.-M. & Kim, B.-I. Thermal dewetting of Pt thin film: Etch-masks for the fabrication of semiconductor nanostructures. *Mater. Sci. Eng. A* **449–451,** 769–773 (2007).

50. Müller, C. M. & Spolenak, R. Microstructure evolution during dewetting in thin Au films. *Acta Mater.* **58,** 6035–6045 (2010).

51. Ye, J. & Thompson, C. V. Mechanisms of complex morphological evolution during solid-state dewetting of single-crystal nickel thin films. *Appl. Phys. Lett.* **97,** 71904 (2010).

52. McDaniel, M. D. *et al.* Growth of epitaxial oxides on silicon using atomic layer deposition: Crystallization and annealing of TiO2 on SrTiO3-buffered Si(001). *J. Vac. Sci. Technol. B* **30,** 04E111 (2012).

53. Bischler, U. & Bertel, E. Simple source of atomic hydrogen for ultrahigh vacuum applications. *J. Vac. Sci. Technol. A* **11,** 458–460 (1993).

54. Chuang, T. J., Brundle, C. R. & Rice, D. W. Interpretation of the x-ray photoemission spectra of cobalt oxides and cobalt oxide surfaces. *Surf. Sci.* **59,** 413–429 (1976).

55. Petitto, S. C. & Langell, M. A. Surface composition and structure of Co3O4(110) and the effect of impurity segregation. *J. Vac. Sci. Technol. Vac. Surf. Films* **22,** 1690–1696 (2004).

56. Bredow, T. & Gerson, A. R. Effect of exchange and correlation on bulk properties of MgO, NiO, and CoO. *Phys. Rev. B* **61,** 5194–5201 (2000).

57. Walsh, A. *et al.* Structural, magnetic, and electronic properties of the Co-Fe-Al oxide spinel system: Density-functional theory calculations. *Phys. Rev. B* **76,** 165119 (2007).

58. Biesinger, M. C. *et al.* Resolving surface chemical states in XPS analysis of first row transition metals, oxides and hydroxides: Cr, Mn, Fe, Co and Ni. *Appl. Surf. Sci.* **257,** 2717–2730 (2011).

59. Sabat, K. C., Paramguru, R. K., Pradhan, S. & Mishra, B. K. Reduction of Cobalt Oxide (Co3O4) by Low Temperature Hydrogen Plasma. *Plasma Chem. Plasma Process.* **35,** 387–399 (2015).

60. Lide, D. R. Standard thermodynamic properties of chemical substances. *CRC Handb. Chem. Phys.* (1992).

61. Verdier, S. *et al.* XPS Study on Al2O3- and AlPO4-Coated LiCoO2 Cathode Material for High-Capacity Li Ion Batteries. *J. Electrochem. Soc.* **154,** A1088–A1099 (2007).

62. Moulder, J. F. *Handbook of X-ray Photoelectron Spectroscopy: A Reference Book of Standard Spectra for Identification and Interpretation of XPS Data*. (Physical Electronics Division, Perkin-Elmer Corporation, 1992).

63. Raïssi, M. *et al.* Interfacial solid phase reactions in cobalt/aluminum oxide/silicon(001) system. *Thin Solid Films* **518,** 5992–5994 (2010).

64. D. Jiles. Introduction to Magnetism and Magnetic Materials, Third Edition. *CRC Press* (2015).

65. Glijer, P., Sin, K., Sivertsen, J. M. & Judy, J. H. Correlation of structural defects and magnetic properties in CoCrPt/Cr and CoCrTaPt/Cr thin films for ultra high density magnetic recording media. *Scr. Metall. Mater.* **33,** 1585–1592 (1995).

66. Si, W. *et al.* Deterioration of the coercivity due to the diffusion induced interface layer in hard/soft multilayers. *Sci. Rep.* **5,** 16212 (2015).

Chapter 4: Influence of Reduction Conditions on the Structure and Magnetic Properties of Cobalt Films

4.1 INTRODUCTION

Bearing the advantages of non-volatility, low power consumption and unlimited endurance, spin-transfer torque random access memory (STT-RAM) is considered as one of the most promising next generation memories and has drawn considerable research attention.[1–3] STT-RAM is a magnetic memory utilizing spin-polarized current to write magnetic bits. It is non-volatile and has the potential to be scaled down below 10 nm. The most important part in a STT-RAM device is the magnetic tunnel junction (MTJ) stack where the spin transfer torque happens and where the data are stored.[4,5] The main components in a MTJ stack are two ultra-thin (2-3 nm) ferromagnetic layers isolated by a insulating tunnel barrier layer (1-2 nm). Single element transition metals, such as Co and Fe, metal alloys like CoFe and CoFeB, and composite electrode, such as Co/Pt and Co/Pd have been proposed to work as the ferromagnetic materials.[6–15] MgO, Al_2O_3, and high-k dielectrics like HfO_2 and $SrTiO_3$ have been explored as the insulating tunnel barrier materials.[7–9,12–14,16–19]

Cobalt metal is a classic ferromagnetic material and has been studied extensively.[7–10,18–21] Giant tunneling magnetoresistance up to 410% at room temperature has been realized in the Co/MgO/Co MTJ stack.[9] The magnetic properties of Co films can be tuned to meet specific requirements. Various factors, such as film crystallinity, thickness, grain size, crystalline imperfections, thermal annealing, substrate roughness, and interactions with underlayer or overlayer, can influence the magnetic properties of

Co films like Curie temperature, coercivity, and magnetic anisotropy.[7,9,18–31] Physical vapor deposition (PVD) methods, such as evaporation, sputtering, and molecular beam epitaxy, are the dominant approaches to depositing ultrathin Co films for the MTJ stack.[9,15,20] There are very limited reports exploring the deposition of Co films by chemical deposition methods.[31–35] Mantovan *et al.*grew MTJ Co films on Al_2O_3 by chemical vapor deposition (CVD) using a di-cobalt octacarbonyl precursor but there was severe carbon contamination in the CVD Co films.[32] Deo *et al.* deposited ferromagnetic Co films on oxidized Si(100) substrates by CVD at 450 °C using a cobalt tricarbonyl nitrosyl precursor but the thin Co films looked porous.[31] Impurity-free cobalt metal growth has been demonstrated using low temperature thermal atomic layer deposition (ALD) by Chabal and Winter groups, but these processes cannot grow Co films on tunnel oxide substrates due to the selective nucleation behavior of the precursors toward metal substrates.[33–35]

In Chapter 3, we reported a method combining low temperature thermal ALD and low temperature reduction processes to producing carbon-free, continuous and ferromagnetic Co films on oxide substrates. We noticed the reduction conditions affected the microstructure and the magnetic properties of the resulting Co films. In order to gain the capability of tuning magnetic properties of Co films and realize specific properties for various applications, elucidation of the process-structure-magnetic property relationship is studied in this chapter.

4.2 EXPERIMENTAL DETAILS

Four-inch wafers of SiO_2/Si(001) were prepared by a thermal oxidation method, which produced an amorphous 300 nm-thick SiO_2 layer on Si(001) substrates. The 0.5 mm-thick wafers were then cut into 20 × 20 mm^2 pieces. MgO(001) substrates of 10 mm × 10 mm × 0.5 mm were purchased from MTI corporation. Al_2O_3(36 nm)/SiO_2/Si(001) substrates were prepared by depositing 300 cycle Al_2O_3 at ~180 °C by ALD using trimethylalumimum (Sigma-Aldrich, 97%) and deionized water as co-reactants. The substrates were ultrasonically cleaned with acetone, isopropyl alcohol, and deionized water for 5 min each, followed by UV/ozone treatment for 15 min to remove residual carbon contamination. The substrates were loaded into the UHV system and then *in-situ* transferred to the ALD chamber for CoO deposition. The ALD system is a custom-built, hot-wall stainless steel rectangular 20 cm long chamber, with a reactor volume of 460 cm^3. Ultrahigh purity argon was used as a purge/carrier gas. The substrate temperature was monitored with a reference thermocouple in the ALD chamber that was previously calibrated against an instrumented wafer.

Bis(N-tert butyl, N'-ethylpropionamidinato) cobalt (II) (Strem, 98%) and deionized water were used as co-reactants for the ALD growth of CoO. During CoO growth, the Co precursor and water were held at 80 °C and room temperature (25 °C), respectively, while the substrate was maintained at a temperature range of 170–180 °C. The water dosing was regulated using an in-line needle valve. Each cycle of CoO growth consisted of a 2-sec dose of Co, a 20-sec purge of Ar, a 1-sec dose of H_2O, and a 20-sec purge of Ar. The deuterium atom reduction was conducted in a custom-built vacuum

chamber. Atomic D was generated by a 400-W Osram Xenophot bulb, which had part of the glass enclosure removed to expose the tungsten filament. A current of 5.2 A was supplied by a DC power supply (KEPCO, MSK10-10M) to the tungsten filament and the filament temperature was ~1800 K, as measured by a pyrometer. At this temperature, the tungsten filament can crack molecular deuterium to generate atomic deuterium.[36] The deuterium gas (Matheson, 99.999%) pressure was controlled by a leak valve. We report the D_2 gas pressure over the filament in the text below. The sample was positioned approximately 4 cm above, and faced toward the tungsten filament. A pyrolytic boron nitride heater from Momentive was 2 cm above the sample. The sample temperature was monitored with a reference thermocouple in the vacuum chamber that was previously calibrated against an instrumented wafer. The deposition of Al metal on reduced Co films as a capping layer was performed in a customized DCA 600 MBE system with a base pressure of 5×10^{-9} Torr.[37]

An *in-situ* VG Scienta R3000 X-ray photoelectron spectroscopy (XPS) system with a monochromated Al Kα source at 1486.6 eV was used to determine film stoichiometry and composition, and the oxidation states of cobalt. The absolute energy scale of the analyzer on the XPS system is calibrated using a two-point measurement such that the Ag $3d_{5/2}$ core level at 368.26 eV and the Fermi edge of Ag at 0.0 eV. An *ex-situ* Veeco Icon atomic force microscopy (AFM) system is used to characterize the film morphology with tapping mode with Bruker TESPA AFM tips. The AFM images were imported into Image J software and the average grain size in every image was measured. *Ex-situ* magnetic property measurements were carried out with a Quantum Design

physical property measurement system (PPMS) combined with vibrating sample magnetometry (VSM) option. Magnetization hysteresis loops were measured with the magnetic field applied parallel to the plane of the thin films. For all the measurements, the samples were at room temperature (25 °C).

4.3 RESULTS AND DISCUSSION

A series of atomic deuterium reductions of 4.5 nm-thick CoO grown on SiO_2/Si(001), MgO(001) and Al_2O_3(36 nm)/SiO_2/Si(001) substrates by ALD was conducted at various experimental conditions. Then the samples were characterized by *in-situ* XPS and it was confirmed that every sample had been completely reduced. Figure 4.1 depicts the Co 2*p* photoelectron (XP) spectrum of one sample on a SiO_2/Si substrate reduced at 220 °C with a partial pressure of deuterium gas at 10^{-5} torr for 60 min. The Co 2*p* XP spectra of all other reduced samples were the same. The binding energies of the main peaks are 778.1 eV and 793.2 eV for the Co $2p_{3/2}$ and Co $2p_{1/2}$ levels, and there is no shoulder peak at 780.5 eV, which means 100% of the CoO has been reduced to Co metal.[38]

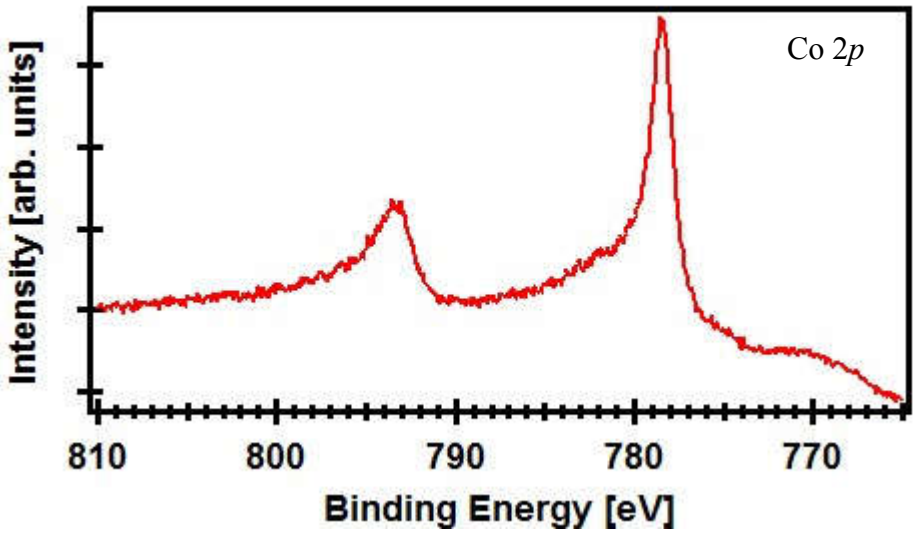

Figure 4.1. Co 2*p* XP spectrum of a 4.5 nm-thick CoO film on a SiO_2/Si(001) substrate reduced at 220 °C with a partial pressure of deuterium gas at 10^{-5} torr for 60 min.

Then 2-nm MBE Al was deposited on the reduced samples as a capping layer for *ex-situ* AFM and VSM characterization. Upon exposure to ambient environment, the Al layer oxidized to form an Al_2O_3 capping layer, which protects the Co films from reoxidization (Chapter 3). Therefore the Co films stayed at Co^0 status during the AFM and VSM characterization. It is reasonable to assume the thickness of the reduced Co films as 3 nm (Chapter 3). The first process parameter under investigation is the reduction time. Three 4.5 nm-thick CoO films on SiO_2/Si(001) substrates were reduced at 220 °C with a partial pressure of deuterium gas at 10^{-5} torr for 30 min, 60 min, and 90 min, respectively. Figure 4.2 shows the AFM and VSM results of the three samples. Figure 4.2a and Figure 4.2b are the AFM image and the hysteresis loop of the sample on the SiO_2/Si(001) substrate reduced at 220 °C with a partial pressure of deuterium gas at

10^{-5} torr for 30 min, respectively. The RMS roughness is 0.86 nm and the average grain size is ~ 15 nm. Its saturated moment is 9.2×10^{-5} emu and saturation magnetization is 1533 emu/cm^3. The coercivity is 90 Oe. Figure 4.2c and Figure 4.2d are the AFM image and the hysteresis loop of the sample on SiO_2/Si(001) substrate reduced at 220 °C with a partial pressure of deuterium gas at 10^{-5} torr for 60 min, respectively. The RMS roughness is 2.09 nm and the average grain size is ~ 25 nm. Its saturated moment is 1.95×10^{-4} emu and saturation magnetization is 2167 emu/cm^3. The coercivity is 460 Oe. Figure 4.2e and Figure 4.2f are the AFM image and the hysteresis loop of the sample on the SiO_2/Si(001) substrate reduced at 220 °C with a partial pressure of deuterium gas at 10^{-5} torr for 90 min, respectively. The RMS roughness is 2.64 nm and the average grain size is ~ 30 nm. Its saturated moment is 2.5×10^{-4} emu and saturation magnetization is 3086 emu/cm^3. The coercivity is 690 Oe. The RMS roughness, average grain size, coercivity and saturation magnetization increase as the reduction time increases. Longer reduction time applies more thermal energy into the Co/SiO_2 system and facilitates dewetting process, which leads to larger RMS roughness and average grain size of the Co films.

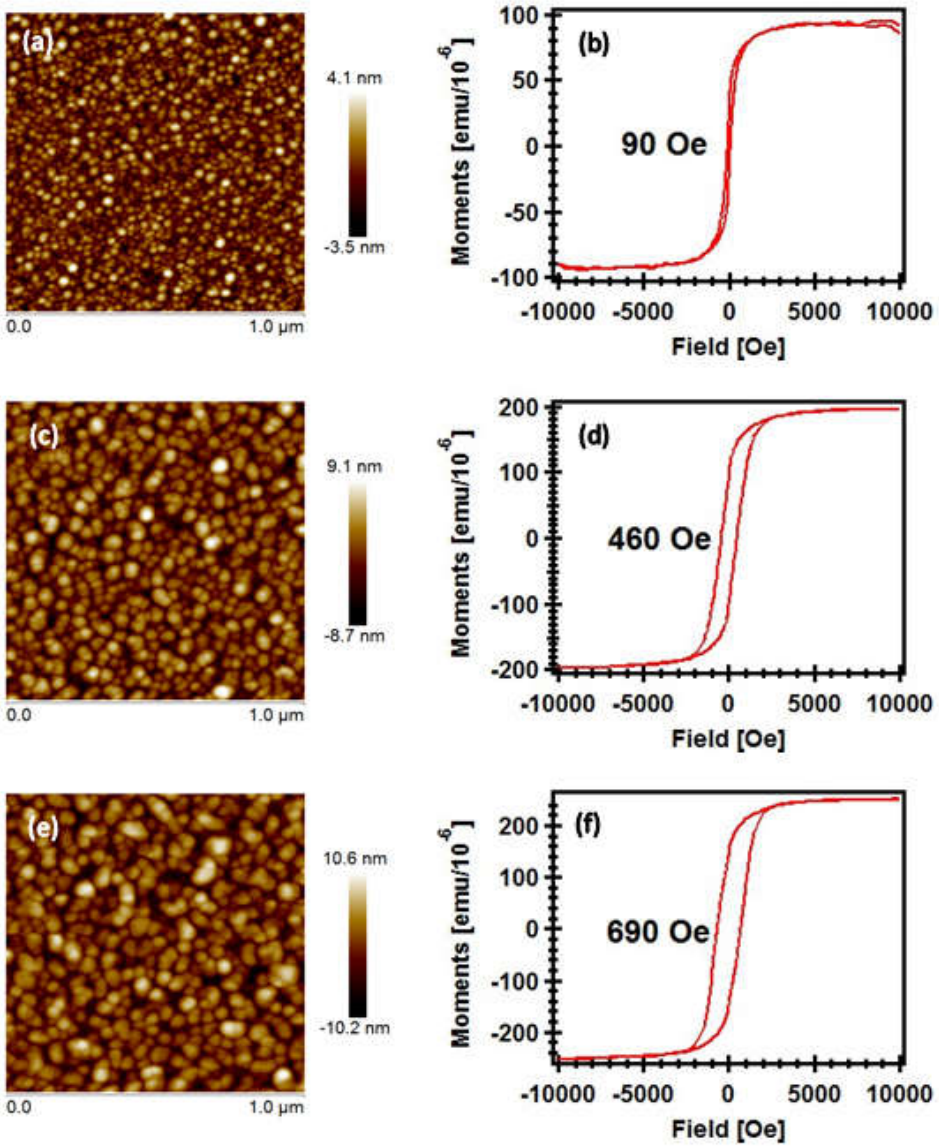

Figure 4.2. (a) and (b) are the AFM image and the hysteresis loop of the sample on SiO_2/Si(001) reduced at 220 °C with a partial pressure of deuterium gas at 10^{-5} torr for 30 min, respectively. (c) and (d) are the AFM image and the hysteresis loop of the sample on SiO_2/Si(001) reduced at 220 °C with a partial pressure of deuterium gas at 10^{-5} torr for 60 min, respectively. (a) and (b) are the AFM image and the hysteresis loop of the sample on SiO_2/Si(001) reduced at 220 °C with a partial pressure of deuterium gas at 10^{-5} torr for 90 min, respectively. All the data have been corrected with the cancellation of the base signal of substrates and capping layers.

The second process parameter under investigation is the reduction temperature. Three 4.5 nm-thick CoO films on SiO_2/Si(001) substrates were reduced with a partial pressure of deuterium gas at 10^{-5} torr for 60 min at 220 °C, 270 °C, and 320 °C, respectively. Figure 4.3 shows the AFM and VSM results of the three samples. Figure 4.3a and Figure 4.3b are the AFM image and the hysteresis loop of the sample on the SiO_2/Si(001) substrate reduced at 220 °C with a partial pressure of deuterium gas at 10^{-5} torr for 60 min, respectively. The RMS roughness is 2.09 nm and the average grain size is ~ 25 nm. Its saturated moment is 1.95×10^{-4} emu and saturation magnetization is 2167 emu/cm^3. The coercivity is 460 Oe. Figure 4.3c and Figure 4.3d are the AFM image and the hysteresis loop of the sample on the SiO_2/Si(001) substrate reduced at 270 °C with a partial pressure of deuterium gas at 10^{-5} torr for 60 min, respectively. The RMS roughness is 2.50 nm and the average grain size is ~ 28 nm. Its saturated moment is 1.22×10^{-4} emu and saturation magnetization is 2582 emu/cm^3. The coercivity is 590 Oe. Figure 4.3e and Figure 4.3f are the AFM image and the hysteresis loop of the sample on the SiO_2/Si(001) substrate reduced at 320 °C with a partial pressure of deuterium gas at 10^{-5} torr for 60 min, respectively. The RMS roughness is 2.99 nm and the average grain size is ~ 34 nm. Its saturated moment is 2.88×10^{-4} emu and saturation magnetization is 3368 emu/cm^3. The coercivity is 760 Oe. The RMS roughness, average grain size, coercivity and saturation magnetization increase as the reduction temperature increases. Higher reduction temperature applies more thermal energy into the Co/SiO_2 system and facilitates dewetting process, which leads to larger RMS roughness and average grain size of the Co films.

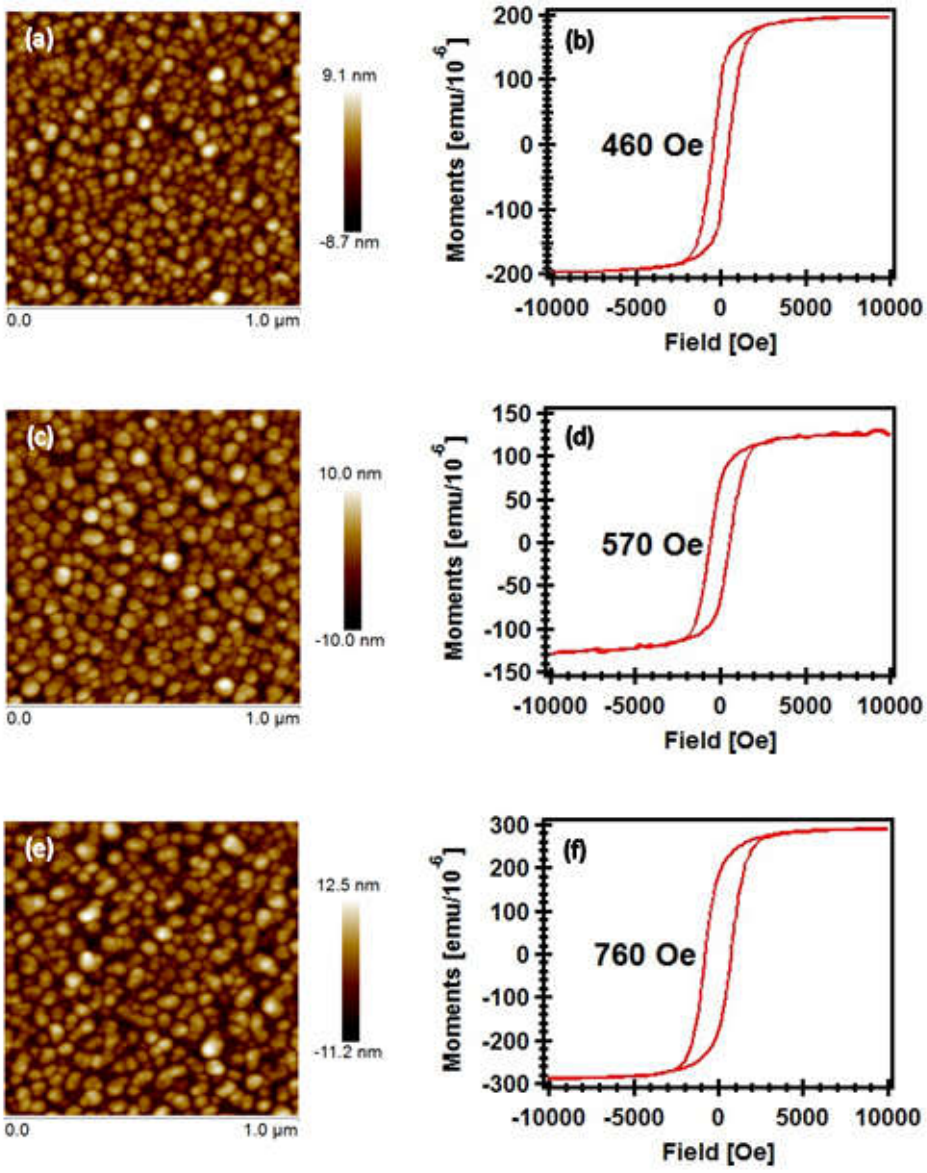

Figure 4.3. (a) and (b) are the AFM image and the hysteresis loop of the sample on SiO_2/Si(001) reduced at 220 °C with a partial pressure of deuterium gas at 10^{-5} torr for 60 min, respectively. (c) and (d) are the AFM image and the hysteresis loop of the sample on SiO_2/Si(001) reduced at 270 °C with a partial pressure of deuterium gas at 10^{-5} torr for 60 min, respectively. (a) and (b) are the AFM image and the hysteresis loop of the sample on SiO_2/Si(001) reduced at 320 °C with a partial pressure of deuterium gas at 10^{-5} torr for 60 min, respectively. All the data have been corrected with the cancellation of the base signal of substrates and capping layers.

The third process parameter under investigation is the partial pressure of deuterium gas. Three 4.5 nm-thick CoO films on SiO_2/Si(001) substrates were reduced at 220 °C for 60 min with a partial pressure of deuterium gas at 10^{-6} torr, 10^{-5} torr, and 10^{-4} torr, respectively. Figure 4.4 shows the AFM and VSM results of the three samples. Figure 4.4a and Figure 4.4b are the AFM image and the hysteresis loop of the sample on the SiO_2/Si(001) substrate reduced at 220 °C with a partial pressure of deuterium gas at 10^{-6} torr for 60 min, respectively. The RMS roughness is 0.98 nm and the average grain size is ~ 19 nm. Its saturated moment is 1.39×10^{-4} emu and saturation magnetization is 1030 emu/cm^3. The coercivity is 170 Oe. Figure 4.4c and Figure 4.4d are the AFM image and the hysteresis loop of the sample on the SiO_2/Si(001) substrate reduced at 220 °C with a partial pressure of deuterium gas at 10^{-5} torr for 60 min, respectively. The RMS roughness is 2.09 nm and the average grain size is ~ 25 nm. Its saturated moment is 1.95×10^{-4} emu and saturation magnetization is 2167 emu/cm^3. The coercivity is 460 Oe. Figure 4.4e and Figure 4.4f are the AFM image and the hysteresis loop of the sample on the SiO_2/Si(001) substrate reduced at 220 °C with a partial pressure of deuterium gas at 10^{-4} torr for 60 min, respectively. The RMS roughness is 3.04 nm and the average grain size is ~ 33 nm. Its saturated moment is 2.85×10^{-4} emu and saturation magnetization is 2857 emu/cm^3. The coercivity is 710 Oe. The RMS roughness, average grain size, coercivity and saturation magnetization increase as the partial pressure of deuterium gas increases. The same influence of the partial pressure of hydrogen gas on the nanoparticle size was observed in the reduction of Ni films on a SiO_2/Si substrate.[39] This was explained by the facilitated formation of Ni_xH_y which increased the free energy of

Ni/SiO_2 system at higher hydrogen pressure. The increased free energy facilitated dewetting and resulted in rougher films.[39]

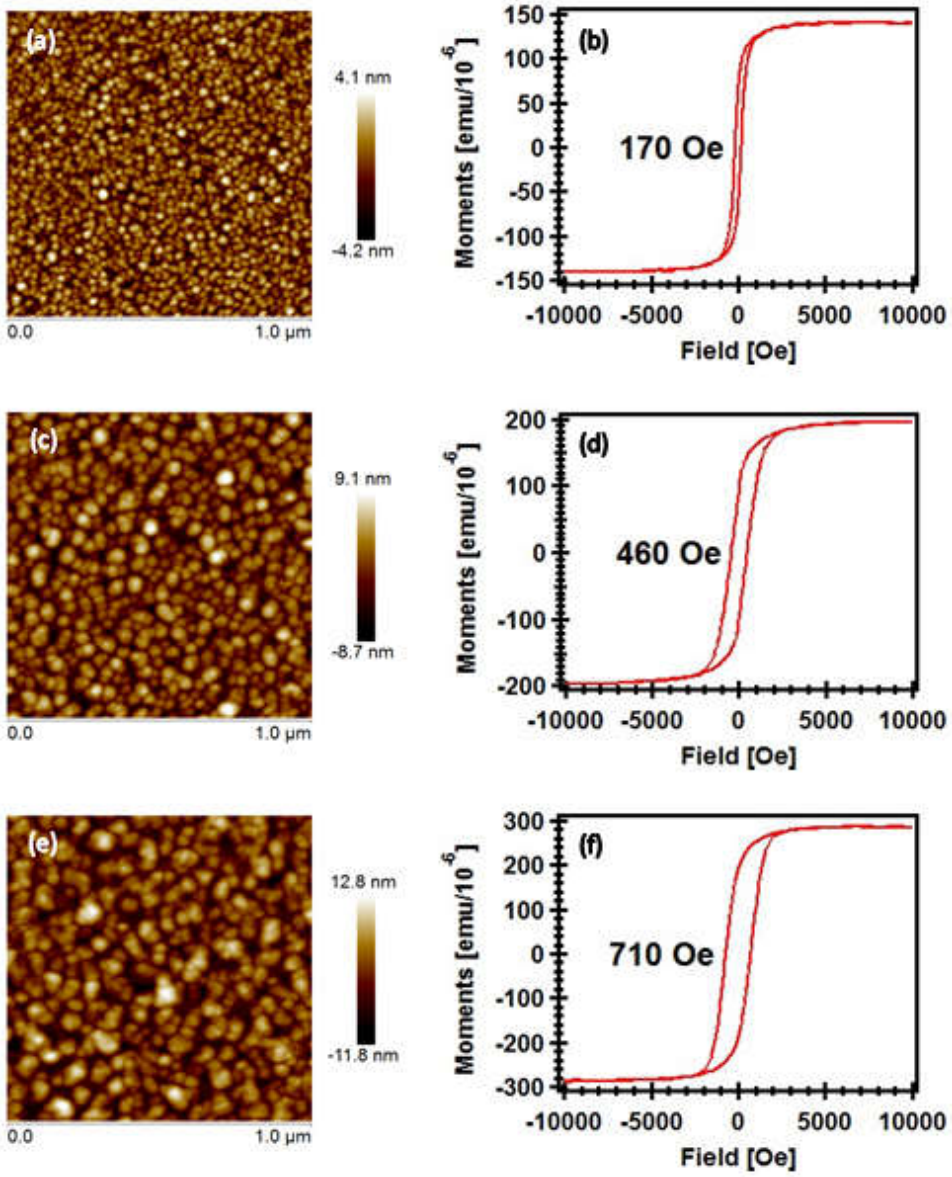

Figure 4.4. (a) and (b) are the AFM image and the hysteresis loop of the sample on SiO_2/Si(001) reduced at 220 °C with a partial pressure of deuterium gas at 10^{-6} torr for 60 min, respectively. (c) and (d) are the AFM image and the hysteresis loop of the sample on SiO_2/Si(001) reduced at 220 °C with a partial pressure of deuterium gas at 10^{-5} torr for 60 min, respectively. (a) and (b) are the AFM image and the hysteresis loop of the sample on SiO_2/Si(001) reduced at 220 °C with a partial pressure of deuterium gas at 10^{-4} torr for 60 min, respectively. All the data have been corrected with the cancellation of the base signal of substrates and capping layers.

The final process parameter under investigation is the substrate underneath the CoO films. Three 4.5 nm-thick CoO films on SiO_2/Si(001), Al_2O_3(36 nm)/SiO_2/Si(001), and MgO(001) substrates were reduced at 220 °C with a partial pressure of deuterium gas at 10^{-5} torr for 60 min, respectively. Figure 4.5 shows the AFM and VSM results of the three samples. Figure 4.5a and Figure 4.5b are the AFM image and the hysteresis loop of the sample on the SiO_2/Si(001) substrate reduced at 220 °C with a partial pressure of deuterium gas at 10^{-5} torr for 60 min, respectively. The RMS roughness is 2.09 nm and the average grain size is ~ 25 nm. Its saturated moment is 1.95×10^{-4} emu and saturation magnetization is 2167 emu/cm^3. The coercivity is 460 Oe. Figure 4.5c and Figure 4.5d are the AFM image and the hysteresis loop of the sample on the Al_2O_3(36 nm)/SiO_2/Si(001) substrate reduced at 220 °C with a partial pressure of deuterium gas at 10^{-5} torr for 60 min, respectively. The RMS roughness is 1.30 nm and the average grain size is ~ 22 nm. Its saturated moment is 1.42×10^{-4} emu and saturation magnetization is 1753 emu/cm^3. The coercivity is 310 Oe. Figure 4.5e and Figure 4.5f are the AFM image and the hysteresis loop of the sample on the MgO(001) substrate reduced at 220 °C with a partial pressure of deuterium gas at 10^{-5} torr for 60 min, respectively. The RMS roughness is 1.19 nm and the average grain size is ~ 21 nm. Its saturated moment is 1.88×10^{-4} emu and saturation magnetization is 1253 emu/cm^3. The coercivity is 290 Oe. The larger RMS roughness and average grain size of the Co films on SiO_2/Si(001) substrate than that of the Co films on Al_2O_3(36 nm)/SiO_2/Si(001) and MgO(001) substrates may be explained by the higher degree of dewetting tendency of the Co/SiO_2 system than that of the Co/Al_2O_3 system and the Co/MgO system. A higher degree of

dewetting tendency facilitates dewetting process, which results in larger roughness and grain size. A rough calculation is conducted to compare the systems' degree of dewetting tendency as follows. The wetting condition is:

$$\gamma_{v/ox} > \gamma_{v/m} + \gamma_{m/ox} \qquad (1)$$

Where $\gamma_{v/ox}$ is the surface energy of the oxide substrate in vacuum, $\gamma_{v/m}$ is the surface energy of the metal film in vacuum, and $\gamma_{m/ox}$ is the interfacial energy between the oxide substrate and the metal film.

$$\gamma_{m/ox} = \gamma_{v/m} + \gamma_{v/ox} - E_{adh} \qquad (2)$$

Where E_{adh} is the adhesion energy between the oxide substrate and the metal film.

Rearranging Equation (1) leads to a

$$\beta = \frac{\gamma_{v/m} + \gamma_{m/ox}}{\gamma_{v/ox}} \qquad (3)$$

When $\beta > 1$ the film has a tendency to dewet and when $\beta < 1$ the film should be stable.

Citing the Co/SiO_2 data from Sangiorgi *et al.*'s work and the Co/Al_2O_3 data from Chatain *et al.*'s work,[40,41] the calculation is listed below.

For Co/SiO_2, $\gamma_{v/m}$ = 1857 mJ/m^2, $\gamma_{v/ox}$ = 450 mJ/m^2, E_{adh} = 901 mJ/m^2, so $\gamma_{m/ox}$ = 1406 mJ/m^2 and β = 7.3.[40] For Co/Al_2O_3, $\gamma_{v/m}$ = 1870 mJ/m^2, $\gamma_{v/ox}$ = 800 mJ/m^2, E_{adh} = 1140 mJ/m^2, so $\gamma_{m/ox}$ = 1530 mJ/m^2 and β = 4.3.[41] These values are listed in Table 4.1. The interaction of Co with MgO is estimated by assuming $\gamma_{v/m}$ = 1870 mJ/m^2 and E_{adh} = 1000 mJ/m^2. The surface energy $\gamma_{v/ox}$ for MgO(001) in vacuum is reported as 1300 mJ/m^2.[42] This allows us to estimate $\gamma_{m/ox}$ as 2170 mJ/m^2 and β as 3.1.

	$\gamma_{v/m}$	$\gamma_{v/ox}$	E_{adh}	$\gamma_{m/ox}$	β
Co/SiO_2	1857	450	901	1406	7.3
Co/Al_2O_3	1870	800	1140	1530	4.3
Co/MgO	1870	1300	1000	2170	3.1

Table 4.1. Summary of data calculation of the degree of dewetting tendency.

Based on this rough calculation, it is demonstrated that the degree of dewetting tendency of the Co/SiO_2 system is larger than that of the Co/Al_2O_3 system and the Co/MgO system, which may explain the larger RMS roughness and average grain size of the Co films on SiO_2/Si(001) substrates than that of the Co films on Al_2O_3 and MgO(001) substrates.

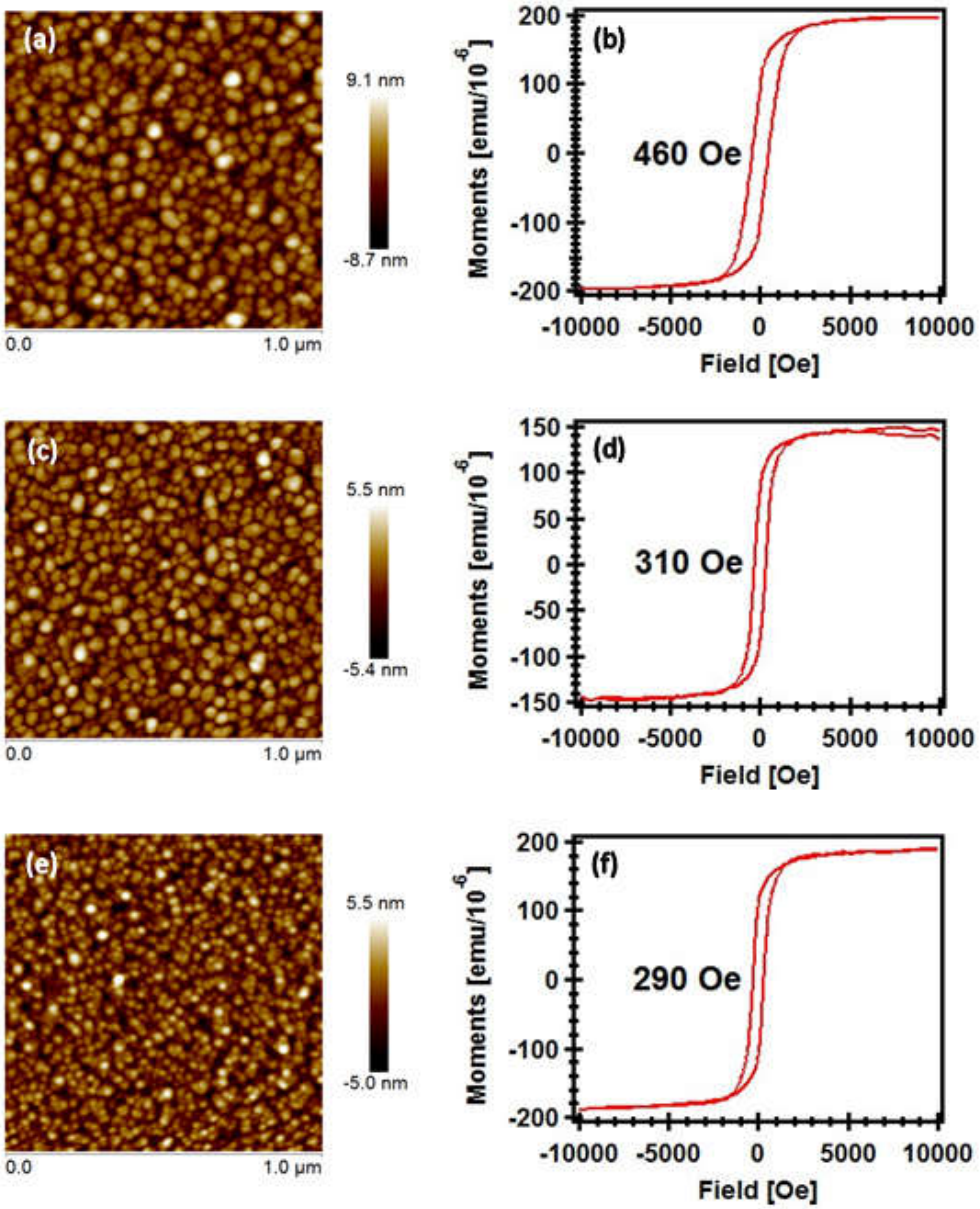

Figure 4.5. (a) and (b) are the AFM image and the hysteresis loop of the sample on SiO_2/Si(001) reduced at 220 °C with a partial pressure of deuterium gas at 10^{-5} torr for 60 min, respectively. (c) and (d) are the AFM image and the hysteresis loop of the sample on Al_2O_3(36 nm)/SiO_2/Si(001) reduced at 220 °C with a partial pressure of deuterium gas at 10^{-5} torr for 60 min, respectively. (a) and (b) are the AFM image and the hysteresis loop of the sample on MgO(001) reduced at 220 °C with a partial pressure of deuterium gas at 10^{-5} torr for 60 min, respectively.

The results of the samples reduced at various experimental conditions are summarized in Table 4.2. Figure 4.6 plots the relationship between average grain size of the reduced Co films and the corresponding coercivity. It is observed that the coercivity is approximately proportional to the average grain size of the reduced Co films. This may be explained by the number of potential defects in the films. When the films are rougher with larger grain size, there may be a larger number of defects (such as voids) in the films, which impedes the hysteresis reversal. The similar influence of grain size on coercivity was reported in $Fe_{74.5-x}Cu_xNb_3Si_{13.5}B_9$ ferromagnets.[43]

Reduction condition	RMS roughness (nm)	Average grain size (nm)	Coercivity (Oe)	Saturation magnetization (emu/cm^3)
T = 220 °C, $P_{D2} = 10^{-5}$ torr, t = 30 min, on SiO_2/Si(001)	0.86	15	90	1533
T = 220 °C, $P_{D2} = 10^{-5}$ torr, t = 60 min, on SiO_2/Si(001)	2.09	25	460	2167
T = 220 °C, $P_{D2} = 10^{-5}$ torr, t = 90 min, on SiO_2/Si(001)	2.64	30	690	3086
T = 270 °C, $P_{D2} = 10^{-5}$ torr, t = 60 min, on SiO_2/Si(001)	2.50	28	570	2582
T = 320 °C, $P_{D2} = 10^{-5}$ torr, t = 60 min, on SiO_2/Si(001)	2.99	34	760	3368
T = 220 °C, $P_{D2} = 10^{-6}$ torr, t = 60 min, on SiO_2/Si(001)	0.98	19	170	1030
T = 220 °C, $P_{D2} = 10^{-4}$ torr, t = 60 min, on SiO_2/Si(001)	3.04	33	710	2857
T = 220 °C, $P_{D2} = 10^{-5}$ torr, t = 60 min, on Al_2O_3(36 nm)/SiO_2/Si(001)	1.30	22	310	1753
T = 220 °C, $P_{D2} = 10^{-5}$ torr, t = 60 min, on MgO(001)	1.19	21	290	1253

Table 4.2. Summary of the results of the samples reduced at various experimental conditions.

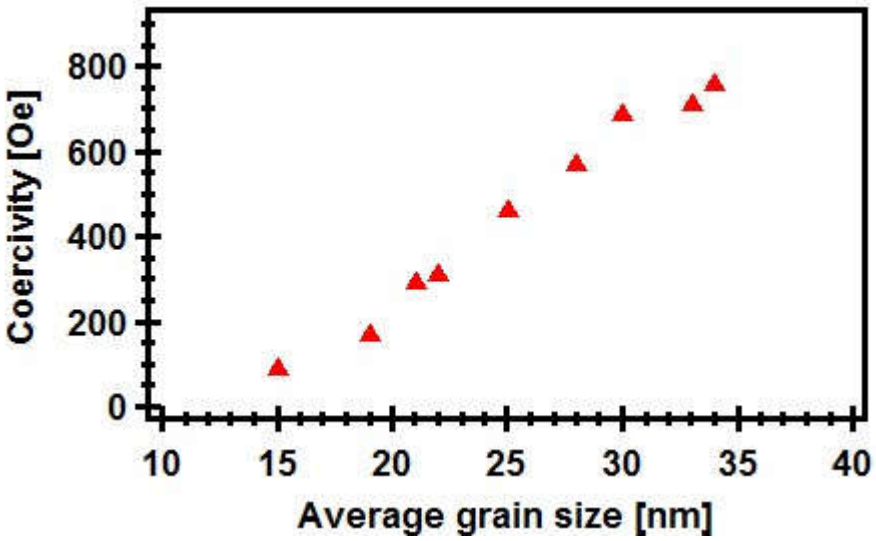

Figure 4.6. A plot of coercivity versus average grain size of the data points collected in this work. Each triangle marker corresponds to each data point.

4.4 CONCLUSIONS

Reduction conditions affected the microstructure and the magnetic properties of the resulting Co films. A series of atomic deuterium reduction of CoO at various reaction time, reaction temperature, partial pressure of deuterium gas, and underlying substrates were conducted to elucidate the process-structure-magnetic property relationship. The increase of reaction time, reaction temperature, and partial pressure of deuterium gas increases the average grain size and the roughness of the Co films. Co films with larger average grain size show higher coercivity. Co films that are grown on substrates with lower degree of dewetting tendency, such as MgO and Al_2O_3, show smaller average grain size and smaller coercivity. Film coercivity from tens to hundreds Oersted can be achieved by tuning the process parameters in this report. This work pushes progress

toward gaining the capability of tuning magnetic properties of Co films and realizing specific properties for various applications.

4.5 REFERENCES

1. Wang, K. L., Alzate, J. G. & Amiri, P. K. Low-power non-volatile spintronic memory: STT-RAM and beyond. *J. Phys. Appl. Phys.* **46,** 74003 (2013).
2. Kawahara, T., Ito, K., Takemura, R. & Ohno, H. Spin-transfer torque RAM technology: Review and prospect. *Microelectron. Reliab.* **52,** 613–627 (2012).
3. Chen, E. *et al.* Advances and Future Prospects of Spin-Transfer Torque Random Access Memory. *IEEE Trans. Magn.* **46,** 1873–1878 (2010).
4. Ikeda, S. *et al.* Magnetic Tunnel Junctions for Spintronic Memories and Beyond. *IEEE Trans. Electron Devices* **54,** 991–1002 (2007).
5. Driskill-Smith, A. *et al.* Latest Advances and Roadmap for In-Plane and Perpendicular STT-RAM. in *2011 3rd IEEE International Memory Workshop (IMW)* 1–3 (2011). doi:10.1109/IMW.2011.5873205
6. Gregg, J. F. *et al.* Giant Magnetoresistive Effects in a Single Element Magnetic Thin Film. *Phys. Rev. Lett.* **77,** 1580–1583 (1996).
7. Oleinik, I. I., Tsymbal, E. Y. & Pettifor, D. G. Structural and electronic properties of Co/Al2O3/Co magnetic tunnel junction from first principles. *Phys. Rev. B* **62,** 3952–3959 (2000).
8. Yuasa, S. *et al.* Giant tunneling magnetoresistance in fully epitaxial body-centered-cubic Co/MgO/Fe magnetic tunnel junctions. *Appl. Phys. Lett.* **87,** 222508 (2005).
9. Yuasa, S., Fukushima, A., Kubota, H., Suzuki, Y. & Ando, K. Giant tunneling magnetoresistance up to 410% at room temperature in fully epitaxial Co/MgO/Co magnetic tunnel junctions with bcc Co(001) electrodes. *Appl. Phys. Lett.* **89,** 42505 (2006).
10. Carvello, B. *et al.* Sizable room-temperature magnetoresistance in cobalt based magnetic tunnel junctions with out-of-plane anisotropy. *Appl. Phys. Lett.* **92,** 102508 (2008).
11. Yuasa, S., Nagahama, T., Fukushima, A., Suzuki, Y. & Ando, K. Giant room-temperature magnetoresistance in single-crystal Fe/MgO/Fe magnetic tunnel junctions. *Nat. Mater.* **3,** 868–871 (2004).
12. Yang, H., Yang, S.-H. & Parkin, S. The role of Mg interface layer in MgO magnetic tunnel junctions with CoFe and CoFeB electrodes. *AIP Adv.* **2,** 12150 (2012).

13. Peng, S. *et al.* Giant interfacial perpendicular magnetic anisotropy in MgO/CoFe/capping layer structures. *Appl. Phys. Lett.* **110,** 72403 (2017).

14. Ikeda, S. *et al.* A perpendicular-anisotropy CoFeB–MgO magnetic tunnel junction. *Nat. Mater.* **9,** 721–724 (2010).

15. Nistor, L. E., Rodmacq, B., Auffret, S. & Dieny, B. Pt/Co/oxide and oxide/Co/Pt electrodes for perpendicular magnetic tunnel junctions. *Appl. Phys. Lett.* **94,** 12512 (2009).

16. Vermeulen, B. F. *et al.* Perpendicular magnetic anisotropy of CoFeB\Ta bilayers on ALD HfO2. *AIP Adv.* **7,** 55933 (2017).

17. Miyazaki, T. & Tezuka, N. Giant magnetic tunneling effect in Fe/Al2O3/Fe junction. *J. Magn. Magn. Mater.* **139,** L231–L234 (1995).

18. Oleinik, I. I., Tsymbal, E. Y. & Pettifor, D. G. Atomic and electronic structure of Co/SrTiO3/Co magnetic tunnel junctions. *Phys. Rev. B* **65,** 20401 (2001).

19. Velev, J. P. *et al.* Negative Spin Polarization and Large Tunneling Magnetoresistance in Epitaxial Co/SrTiO3/Co Magnetic Tunnel Junctions. *Phys. Rev. Lett.* **95,** 216601 (2005).

20. Chappert, C. & Bruno, P. Magnetic anisotropy in metallic ultrathin films and related experiments on cobalt films (invited). *J. Appl. Phys.* **64,** 5736–5741 (1988).

21. Teresa, J. M. D. *et al.* Role of Metal-Oxide Interface in Determining the Spin Polarization of Magnetic Tunnel Junctions. *Science* **286,** 507–509 (1999).

22. Berger, A., Linke, U. & Oepen, H. P. Symmetry-induced uniaxial anisotropy in ultrathin epitaxial cobalt films grown on Cu(1 1 13). *Phys. Rev. Lett.* **68,** 839–842 (1992).

23. Chuang, C. *et al.* Thickness dependent reactivity and coercivity for ultrathin Co/Si(111) films. *Thin Solid Films* **519,** 8371–8374 (2011).

24. de Miguel, J. J. *et al.* Influence of the growth conditions on the magnetic properties of fcc cobalt films: from monolayers to superlattices. *J. Magn. Magn. Mater.* **93,** 1–9 (1991).

25. Hehn, M., Padovani, S., Ounadjela, K. & Bucher, J. P. Nanoscale magnetic domain structures in epitaxial cobalt films. *Phys. Rev. B* **54,** 3428–3433 (1996).

26. Kief, M. T., Mankey, G. J. & Willis, R. F. Micromagnetic properties of ultrathin cobalt films. *J. Appl. Phys.* **69,** 5000–5002 (1991).

27. Kisielewski, M. *et al.* Magnetic ordering in ultrathin cobalt film covered by an overlayer of noble metals. *J. Appl. Phys.* **93,** 7628–7630 (2003).

28. Kisielewski, M., Maziewski, A., Tekielak, M., Wawro, A. & Baczewski, L. T. New Possibilities for Tuning Ultrathin Cobalt Film Magnetic Properties by a Noble Metal Overlayer. *Phys. Rev. Lett.* **89,** 87203 (2002).

29. Schneider, C. M. *et al.* Curie temperature of ultrathin films of fcc-cobalt epitaxially grown on atomically flat Cu(100) surfaces. *Phys. Rev. Lett.* **64,** 1059–1062 (1990).

30. Speckmann, M., Oepen, H. P. & Ibach, H. Magnetic Domain Structures in Ultrathin Co/Au(111): On the Influence of Film Morphology. *Phys. Rev. Lett.* **75,** 2035–2038 (1995).

31. Deo, N., Bain, M. F., Montgomery, J. H. & Gamble, H. S. Study of magnetic properties of thin cobalt films deposited by chemical vapour deposition. *J. Mater. Sci. Mater. Electron.* **16,** 387–392 (2005).

32. Mantovan, R. *et al.* Atomic Layer Deposition of Magnetic Thin Films. *Acta Phys. Pol. A* **6,** 1271–1280 (2007).

33. Kwon, J., Saly, M., Halls, M. D., Kanjolia, R. K. & Chabal, Y. J. Substrate Selectivity of (tBu-Allyl)Co(CO)3 during Thermal Atomic Layer Deposition of Cobalt. *Chem. Mater.* **24,** 1025–1030 (2012).

34. Kalutarage, L. C., Martin, P. D., Heeg, M. J. & Winter, C. H. Volatile and Thermally Stable Mid to Late Transition Metal Complexes Containing α-Imino Alkoxide Ligands, a New Strongly Reducing Coreagent, and Thermal Atomic Layer Deposition of Ni, Co, Fe, and Cr Metal Films. *J. Am. Chem. Soc.* **135,** 12588–12591 (2013).

35. Klesko, J. P., Kerrigan, M. M. & Winter, C. H. Low Temperature Thermal Atomic Layer Deposition of Cobalt Metal Films. *Chem. Mater.* **28,** 700–703 (2016).

36. Bischler, U. & Bertel, E. Simple source of atomic hydrogen for ultrahigh vacuum applications. *J. Vac. Sci. Technol. A* **11,** 458–460 (1993).

37. McDaniel, M. D. *et al.* Growth of epitaxial oxides on silicon using atomic layer deposition: Crystallization and annealing of TiO2 on SrTiO3-buffered Si(001). *J. Vac. Sci. Technol. B* **30,** 04E111 (2012).

38. Biesinger, M. C. *et al.* Resolving surface chemical states in XPS analysis of first row transition metals, oxides and hydroxides: Cr, Mn, Fe, Co and Ni. *Appl. Surf. Sci.* **257,** 2717–2730 (2011).

39. Geissler, A., He, M., Benoit, J.-M. & Petit, P. Effect of Hydrogen Pressure on the Size of Nickel Nanoparticles Formed during Dewetting and Reduction of Thin Nickel Films. *J. Phys. Chem. C* **114,** 89–92 (2010).

40. Sangiorgi, R., Muolo, M. L., Chatain, D. & Eustathopoulos, N. Wettability and Work of Adhesion of Nonreactive Liquid Metals on Silica. *J. Am. Ceram. Soc.* **71,** 742–748

41. Chatain, D., Rivollet, I. & Eustathopoulos, N. Adhésion thermodynamique dans les systèmes non-réactifs métal liquide-alumine. *J. Chim. Phys.* **83,** 561–567 (1986).

42. Gutshall, P. L. & Gross, G. E. Cleavage Surface Energy of NaCl and MgO in Vacuum. *J. Appl. Phys.* **36,** 2459–2460 (1965).

43. Herzer, G. Grain size dependence of coercivity and permeability in average ferromagnets. *IEEE Trans. Magn.* **26,** 1397–1402 (1990).

Chapter 5: Area-Selective Atomic Layer Deposition of Cobalt Oxide and Cobalt Metal by Using Polystyrene as a Passivation Material

5.1 INTRODUCTION

As the critical dimension of electronics approach sub-10 nm scales, current patterning techniques enabled by lithographic and etch processes are experiencing more and more challenges.[1–4] The development of advanced lithographic processes, such as extreme ultraviolet lithography, and advanced etch processes, such as multiple patterning, are progressing the further scale-down of chips.[5–10] A disadvantage with these advanced technologies is their high cost.[11] At the same time the development of alternate pattering techniques, like bottom-up patterning, are drawing increased attention. Bottom-up patterning utilizes interactions between molecules to assemble nanostructures, which imparts the low-cost advantage.[12–14] A typical example of bottom-up patterning that is being explored extensively is area-selective deposition (ASD).[15–19] Based on the principle that film nucleation and growth only happen at reactive sites rather than inert sites, ASD employs specific surface chemistries to deposit material on desired regions of substrates selectively.[20] The selectivity offers ASD the potential of self-alignment and the reduction of lithography and post-deposition etch steps.[16]

Atomic layer deposition (ALD) is a self-limiting chemical reaction process, in which individual reactants saturate and are purged out of the reactor in sequence.[21] Due to the self-limiting behavior, ALD can produce highly uniform and conformal films over three-dimensional structures with precise thickness control, which meets well the demands of sub-10 nm node fabrication.[21] Therefore, ALD is an excellent approach to

achieve ASD and there have been increasing reports working on area-selective atomic layer deposition (AS-ALD).[15–17,19,22] In the practice of AS-ALD, there are regions of different reactivities toward ALD precursors on pre-patterned substrates. ALD precursors absorb on the reactive regions and films grow there. Area-activation and area-deactivation are the two common ways to create regions of different reactivities toward ALD precursors on substrates.[23] Area-activation means desired regions of non-reactive substrates are functionalized by reactive groups while area-deactivation means desired regions of reactive substrates are passivated by non-reactive groups.[24,25]

The selection and patterning of passivation materials is the key to AS-ALD enabled by area-deactivation.[23] Self-assembled monolayers, such as octadecyltrichlorosilane, are the most-widely used passivation materials in current ASD studies due to their excellent passivation effects and self-alignment behavior to certain surface sites .[26–31] But SAMs have their limitations. First, to produce a defect-free SAM layer that can block nucleation and growth well, extended SAM deposition time as long as 24 h is required for many SAMs.[29,32] Besides, SAMs are just monolayers and if a thick ALD film is grown, it can grow up and beyond the feature boundary. SAMs have the potential to be degraded or even damaged and so lose their passivation capabilities after a long deposition time, which leads to SAM failure in ASD of thick films.[33,34] Additionally, SAM patterning approaches have not been fully developed. While micro-patterns can be generated by methods like microcontact printing, nano-patterning of SAMs is still difficult.[24,27]

To overcome these limitations of SAMs and target the applications that SAMs cannot meet, considerable research attention has focused on another group of passivation materials—polymer films.[19,35–39] Defect-free polymer films can be coated onto substrates within a few minutes and polymer film thickness can be easily tuned from nanometers to micrometers. So using polymer films as passivation materials can work in ASD of thick films. Another important advantage is that there have been many developed patterning approaches for polymer films to produce both micro-patterns and nano-patterns, such as photolithography and directed self-assembly.[40] A number of polymers have been identified as effective growth inhibitors to certain materials, such as polyimide and polymethacrylamide to platinum deposition,[25,39] poly(vinyl pyrrolidone) to noble metal deposition,[38] and poly(methylmethacrylate) to TiO_2 deposition.[19] However, there is no report exploring the feasibility of using polystyrene as passivation material. There are only C and H elements in PS so the materials whose nucleation and growth rely on hydroxyl groups cannot grow on PS film in principle. PS films possess no glass transition temperature after UV-induced crosslinking,[41] which means PS films can work over a wide temperature window (< 240 °C). Besides, as a photosensitive polymer and a common component of copolymers, PS can be patterned easily by photolithography and direct self-assembly. These strengths make PS film a promising passivation material candidate.

Due to their various properties, cobalt oxides and cobalt metal find applications in many fields. With a band gap of 2.4 eV, cobalt (II) oxide has been used for photoelectrochemical water oxidation.[42] Cobalt spinel has a band gap of 1.6 eV and has

been applied in sensors, spintronics, and catalysis.[43–47] Due to its superior wetting behavior on copper, cobalt metal has been studied as a Cu electromigration barrier and a next-generation liner material in the back end of line (BEOL) process.[48,49] As ferromagnetic materials, Co and Co alloys like CoFe and CoFeB have been studied as the fixed and free layer for magnetic tunneling junction (MTJ) devices.[50–54]

In Chapter 3, we demonstrated a low temperature ALD approach to growing carbon-free CoO film and the methods for transforming CoO to Co_3O_4 and Co films. The ALD growth temperature for CoO is 170–180 °C and polystyrene films can work over this condition. In this work, we report the area-selective deposition of cobalt (II) oxide and the further reduction to cobalt metal by using polystyrene as a passivation material. The polystyrene is patterned using UV-crosslinking and using self-assembly of polystyrene-polymethylmethacrylate (PS-PMMA).

5.2 EXPERIMENTAL DETAILS

Four-inch wafers of SiO_2/Si(001) were prepared by a thermal oxidation method, which produced an amorphous 300 nm-thick SiO_2 layer on Si substrate. The 0.5 mm-thick wafers were then cut into 20 × 20 mm^2 pieces. MgO(001) substrates of 10 mm × 10 mm × 0.5 mm are purchased from MTI corporation. The substrates were ultrasonically cleaned with acetone, isopropyl alcohol, and deionized water for 5 min each, followed by UV/ozone treatment for 15 min to remove residual carbon contamination.

Polystyrene (purchased from Aldrich with average Mw = 200000) was dissolved in propylene glycol methyl ether acetate (Sigma-Aldrich, 99.5%) to prepare a 2 wt% polystyrene solution. The 2 wt% polystyrene solution was spincoated onto the cleaned

SiO_2/Si or MgO(001) substrates to form a 40 nm-thick polystyrene film on the substrates. The PS/SiO_2/Si or PS/MgO(001) samples were then exposed by 185 nm and 254 nm ultraviolet light in an ambient or a N_2 environment with a shadow mask on the top of samples. The shadow mask used in this work was a slim-bar 1000 mesh copper TEM grid with pitch of 25 μm, bar width of 6 μm and hole width of 19 μm. The PS regions that were not shadowed by the mask were exposed to deep UV-light and crosslinked while the PS regions that were shadowed by the mask were not exposed to deep UV-light and not crosslinked. After UV-light exposure, the samples were rinsed by toluene (Fisher Chemical, 99.9%) and cleaned by deionized (DI) water, in which the PS regions that were not crosslinked were removed and PS micro-patterns formed on substrates.

PS nano-patterns were formed by using self-assembled PMMA-PS diblock copolymers. Random copolymer poly(styrene-co-methyl methacrylate) with α- hydroxyl-ω-tempo moiety terminated was purchased from Polymer Source. The Mn of the random copolymer was 6400 with 59.5 mol% styrene. The random copolymer was dissolved in toluene to prepare a 1 wt% random copolymer solution. Poly(styrene-b-methyl methacrylate) diblock copolymer was also purchased from Polymer Source. The Mn of styrene was 55000 and the Mn of methyl methacrylate was 22000. The diblock copolymer was dissolved in toluene to prepare a 1 wt% diblock copolymer solution. The 1 wt% random copolymer solution was first spincoated onto the cleaned SiO_2/Si or MgO(001) substrates to form a 50 nm-thick polymer layer. Then the samples were heated on a hot plate at 230 °C for 10 min, in which about 3 nm-thick brush layer was end-grafted onto substrates. After rinsing the samples by toluene to get rid of the non-grafted

random copolymer, only the 3 nm-thick end-grafted brush layer remained on the substrates. The 1 wt% diblock copolymer solution was then spincoated onto the brush-layer-coated substrates to form a 50 nm-thick polymer layer. The samples were heated on a hot plate at 230 °C for 5 min during which PMMA formed cylinders aligned perpendicular to the substrate and PS formed a continuous matrix. The PMMA cylinders and underlying brush layer were removed by plasma etching to generate nano-patterns of PS with 20-30 nm holes and 40-50 nm pitch on the substrates.

After pre-treatment, the substrates were loaded into the UHV system and then *in-situ* transferred to the ALD chamber for CoO deposition. The ALD system is a custom-built, hot-wall stainless steel rectangular 20 cm long chamber, with a reactor volume of 460 cm^3. Ultrahigh purity argon was used as a purge/carrier gas. The substrate temperature was monitored with a reference thermocouple in the ALD chamber that was previously calibrated against an instrumented wafer. Bis(N-tert butyl, N'-ethylpropionamidinato) cobalt (II) and water were used as co-reactants for the ALD growth. During CoO growth, the Co precursor and water were held at 80 °C and room temperature (25 °C), respectively, while the substrate was maintained at a temperature between 170–180 °C. The water dosing was regulated using an in-line needle valve. Each cycle of CoO growth consisted of a 2-sec dose of Co, a 20-sec purge of Ar, a 1-sec dose of H_2O, and a 20-sec purge of Ar. After CoO growth, the samples were unloaded and O_2 plasma etching was employed to remove all the PS on the samples.

The deposition of Al metal was performed on some samples in a customized DCA 600 MBE system with a base pressure of 5×10^{-9} Torr. Al reacted with air after unloading

samples to atmosphere to form Al_2O_3 as a capping layer of metallic cobalt films for *ex-situ* characterization. The deuterium atom reduction of CoO were conducted in a custom-built vacuum chamber. Atomic D was generated by a 400-W Osram Xenophot bulb, which had part of the glass enclosure removed to expose the tungsten filament. A current of 5.2 A was supplied by a DC power supply (KEPCO, MSK10-10M) to the tungsten filament and the filament temperature was ~1800 K, as measured by a pyrometer. At this temperature, the tungsten filament can crack molecular deuterium to generate atomic deuterium.[55] The deuterium gas (Matheson, 99.999%) pressure was controlled by a leak valve. The sample was positioned approximately 4 cm above, and faced toward the tungsten filament. A pyrolytic boron nitride heater from Momentive was 2 cm above the sample. The sample temperature was monitored with a reference thermocouple in the vacuum chamber that was previously calibrated against an instrumented wafer.

An *in-situ* VG Scienta R3000 XPS system with a monochromated Al Kα source at 1486.6 eV was used to determine film stoichiometry and composition, and the oxidation states of cobalt. The absolute energy scale of the analyzer of the XPS system is calibrated using a two-point measurement such that the Ag $3d_{5/2}$ core level is at 368.26 eV and the Fermi edge of Ag is at 0.0 eV. *Ex-situ* scanning electron microscope (SEM) and atomic force microscope (AFM) were used to characterize the metal oxide and metal patterns. SEM was conducted by a ZEISS Neon 40 SEM equipped with Bruker EDS. AFM was conducted by a Veeco Icon AFM system at tapping mode with Bruker TESPA AFM tips.

Magnetic property measurements were carried out with a Quantum Design physical property measurement system (PPMS) combined with the vibrating sample

magnetometry (VSM) option. Magnetization hysteresis loops were measured with the magnetic field applied parallel to the plane of the thin films. For all the measurements, the samples were at room temperature (25 °C).

5.3 RESULTS AND DISCUSSION

In order to determine the passivation capability of polystyrene for inhibiting the nucleation and film growth of CoO on oxide substrates, 40 nm-thick PS film was spincoated onto SiO_2/Si(001) and MgO(001) substrates, and then 300 cycle CoO ALD was conducted on both PS/SiO_2/Si and PS/MgO samples. The black color in Figure 5.1 shows the Co 2*p* X-ray photoelectron (XP) spectrum of the PS/SiO_2/Si sample after 300 cycle CoO ALD and there is no Co signal at all. 300 CoO ALD cycles should lead to 9 nm CoO on SiO_2 (Chapter 3). To further examine the passivation capability of UV-induced crosslinked PS, one PS/SiO_2/Si sample was exposed to mercury UV-light for 1 h in a N_2 environment. After the UV-light exposure the sample was rinsed with toluene and there was no thickness decrease of the PS film after the toluene rinse while the as-coated PS film dissolved completely in the toluene rinse. This indicates the 1 h UV-light exposure successfully crosslinked the PS film and imparted its resistance to the toluene solvent. Then 300 cycle CoO ALD was conducted on the crosslinked PS/SiO_2/Si sample and the green color in Figure 5.1 shows its Co 2*p* XP spectrum after CoO deposition. Compared to the untreated PS (black color) there is very noisy signal as shown in the insert of Figure 5.1. This noisy signal may come from a small amount ALD precursor adsorbed on the crosslinked PS surface. These results demonstrate both as-coated PS and

crosslinked PS are very effective in blocking CoO ALD on oxide substrates. In order to determine whether the surface of the oxide substrates were damaged by PS coating and PS removal, another as-coated PS/SiO_2/Si sample was rinsed with toluene to remove all the PS, and then was subjected to 300 CoO ALD cycles. The red color in Figure 5.1 shows its Co 2*p* XP spectrum after the CoO deposition. The binding energies of the main peaks are at 780.5 eV and 796.5 eV for Co $2p_{3/2}$ and Co $2p_{1/2}$ levels, respectively, and at 786.4 eV and 803.0 eV for the Co $2p_{3/2}$ and Co $2p_{1/2}$ for satellite peaks, respectively. The 2*p* binding energy position in conjunction with the very strong satellite at ~ 6 eV higher binding energy is consistent with Co being in the +2 valence state with high spin.[56] The resulting film thickness is about 9 nm, which is the same with the thickness of 300 cycle CoO film grown on clean SiO_2/Si substrates. These results indicate the hydroxyl sites of the oxide surface that favor the nucleation and film growth of CoO are free of damage after PS coating and PS removal with toluene.

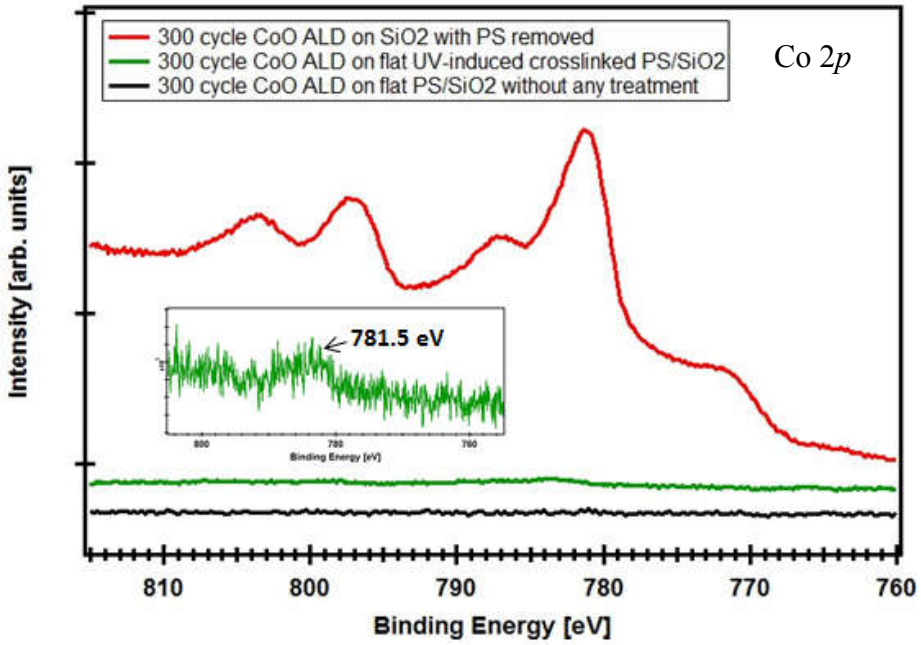

Figure 5.1. Co 2*p* XP spectrum of the samples after 300 cycle CoO ALD at ~ 180 °C (black color refers to the as-coated PS/SiO_2/Si sample, green color refers to the UV-induced crosslinked PS/SiO_2/Si sample, and the red color refers to the PS/SiO_2/Si with PS removed sample, respectively).

Micro-patterns and nano-patterns of polystyrene were prepared to demonstrate the area-selective deposition of CoO on oxide substrates. PS micro-patterns were created by photolithography. PS is sensitive to deep UV-light and can work like a photoresist. Figure 5.2a shows the shadow mask used in this work. It is a slim-bar 1000 mesh copper TEM grid with pitch of 25 µm, bar width of 6 µm and hole width of 19 µm. During UV-light exposure, the PS regions that were not shadowed by the mask were exposed to deep UV-light and crosslinked. The PS regions that were shadowed by the mask were not exposed to deep UV-light and not crosslinked. After UV-light exposure the samples were rinse with toluene to remove the non-crosslinked PS. A key parameter determing the

quality of PS patterns is the crosslinking environment. Figure 5.2b and 5.2c represents the AFM images of PS patterns on SiO_2/Si substrate created by exposing to deep UV-light for 1 h in an ambient environment and in a N_2 environment, respectively, followed by the toluene rinse. The squares are PS and the bars among the squares are the underlying SiO_2/Si substrate. The PS patterns exposed in an ambient environment exhibited severe damage and the PS squares featured sharp edges and hollow centers. While the PS patterns exposed in a N_2 environment are uniform squares. The difference came from the existence of O_2 during the UV-light exposure. With the existence of O_2, there were side scission reactions happening along with the crosslink reaction and the side scission reaction could damage PS film, as shown in Illustration 5.1.[57] At the same time, O_2 could be converted to O_3 by UV-light exposure and O_3 could damage PS. Therefore, in order to produce high-quality crosslinked PS without side film components and without pattern degradation, the UV-light exposure should be conducted in oxygen-free environment. The existence of side film components is a possible reason why there is a small amount precursor adsorbed on the UV-induced crosslinked PS film in Figure 5.1 because it cannot be guaranteed that there was a completely oxygen-free environment of our experimental apparatus even under a N_2 purge.

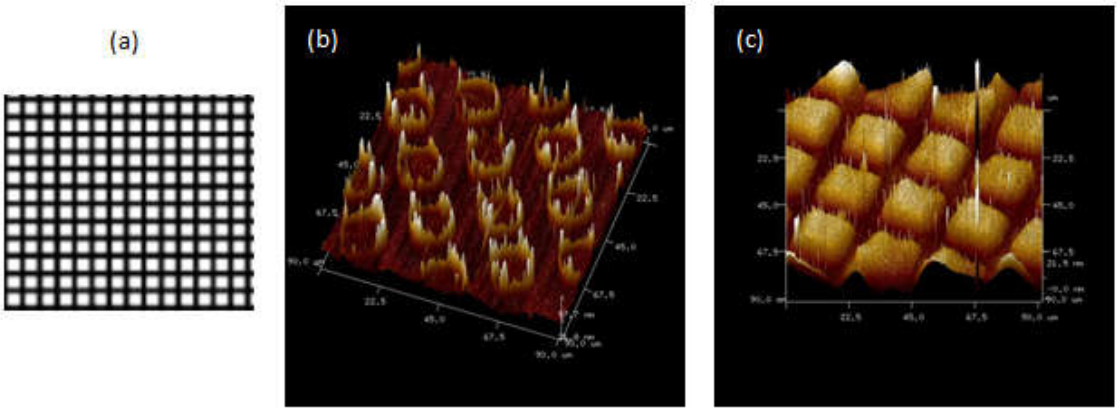

Figure 5.2. (a) A schematic of the shadow mask used in UV-light exposure experiments. (b) AFM image of the PS patterns on SiO_2/Si substrate created by exposing to deep UV-light for 1 h in an ambient environment followed by the toluene rinse. (c) AFM image of the PS patterns on SiO_2/Si substrate created by exposing to deep UV-light for 1 h in a N_2 environment followed by the toluene rinse.

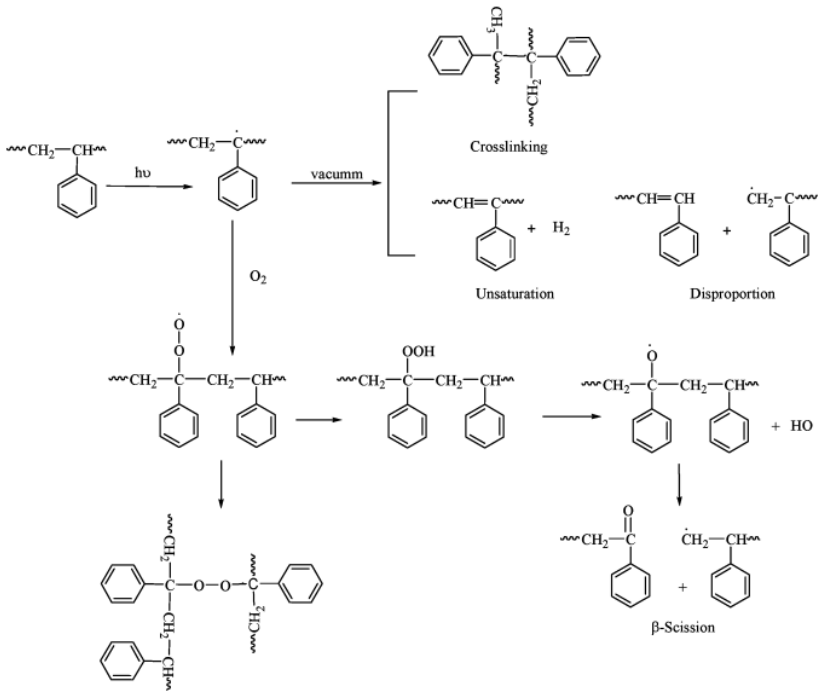

Illustration 5.1. Reactions accomplished by PS upon irradiation with UV-light.[57]

Figure 5.3 shows the SEM and AFM images of the PS micro-patterns used in this work to guide the AS-ALD of CoO. 12 nm-thick CoO was grown on the PS template/SiO_2/Si by ALD at ~180 °C and then the PS template was removed by O_2 plasma etching. In Figure 5.3a, the relatively dark regions are the PS squares while the relatively bright regions are the SiO_2/Si substrate because SiO_2/Si is more conductive than PS. In Figure 5.3b, the relatively bright regions are the PS squares while the relatively dark regions belong to SiO_2/Si substrate, which means the PS squares are higher than the SiO_2/Si substrate. Figure 5.4a and 5.4b show the SEM and AFM images of the CoO patterns on SiO_2/Si substrate after the PS template was removed. In Figure 5.4a, the relatively dark regions are the CoO bars while the relatively bright regions belong to the SiO_2/Si substrate. In Figure 5.4b, the relatively bright regions are the CoO bars while the relatively dark regions belong to the SiO_2/Si substrate, which means the CoO bars are higher the SiO_2/Si substrate. The CoO only grew on the bar regions that were not covered by the PS squares. The CoO bar patterns are uniform across the patterned area and their feature size (~6.5 μm wide) is close to the original feature size (6 μm wide) of the shadow mask. The CoO patterns were confirmed by elemental analysis results as shown in Figure 5.5. Figure 5.5a and 5.5b are the elemental map and line analysis of the CoO patterns, respectively, in which Co element was scanned. Both indicate the Co element is only present on the bar regions.

The CoO was further reduced to metallic Co by 2 h atomic deuterium reduction at 220 °C followed by 2-nm MBE Al capping layer deposited on top. Upon exposure to the

ambient environment, the Al layer oxidized to form an Al_2O_3 capping layer protecting metallic Co from reoxidizing. Figure 5.4c and 5.4d show the SEM and AFM images of the Al_2O_3 capped Co patterns on SiO_2/Si substrate. In Figure 5.4c, the relatively dark regions are the Al_2O_3 capped Co bars while the relatively bright regions belong to the Al_2O_3-capped SiO_2/Si substrate. In Figure 5.4d, the relatively bright regions are the Al_2O_3-capped Co bars while the relatively dark regions belong to the Al_2O_3-capped SiO_2/Si substrate. The Co patterns are almost the same with the CoO patterns in the x- and y-directions and there is no deformation caused by reduction. The difference in the z-direction comes from the thickness contraction from CoO to Co, which has been discussed in Chapter 3. Figure 5.5 presents the magnetization hysteresis loops of the reduced Co patterns on the SiO_2/Si substrate. The hysteresis loops were measured by VSM with the magnetic field applied parallel to the plane of the thin films at room temperature (25 °C). The reduced Co patterns are ferromagnetic and the coercivity is 440 Oe.

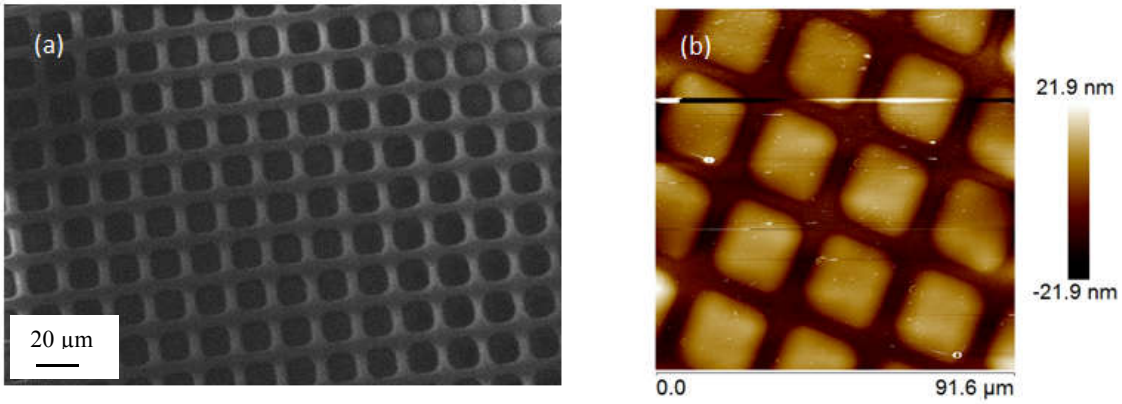

Figure 5.3. (a) and (b) are SEM and AFM images of the as-prepared PS micro-patterns, respectively. In Figure 5.3a, the relatively dark regions are the PS squares while the relatively bright regions belong to the SiO_2/Si substrate. In Figure 5.3b, the relatively bright regions are the PS squares while the relatively dark regions belong to the SiO_2/Si substrate.

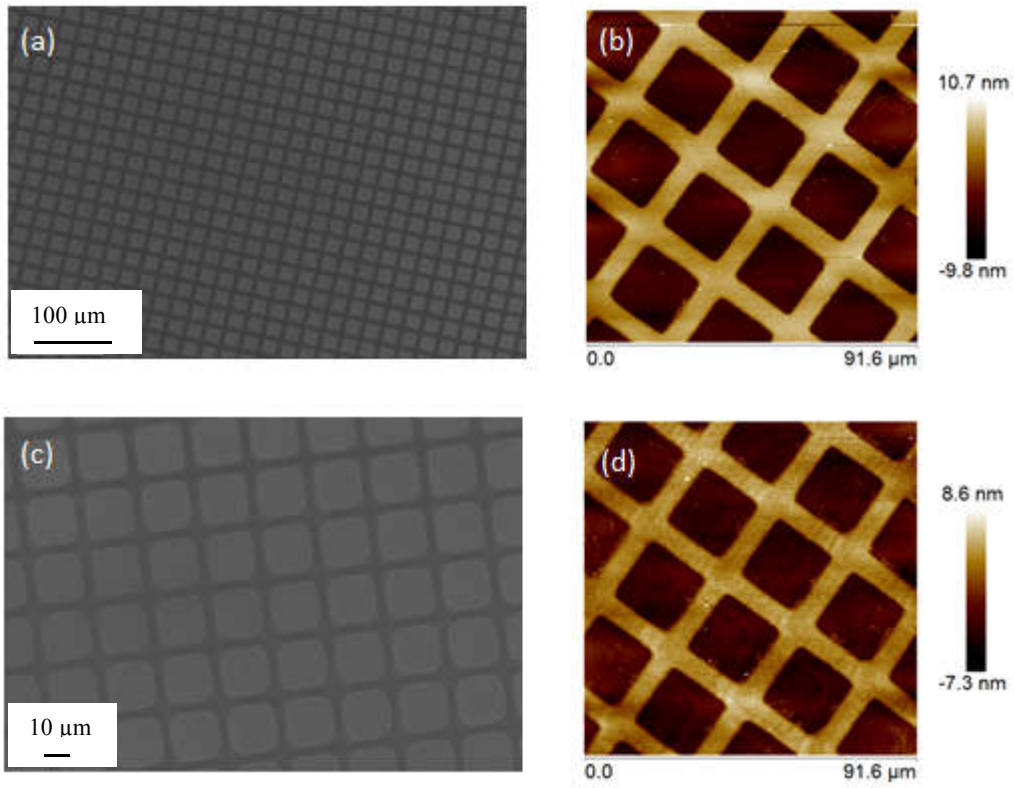

Figure 5.4. (a) and (b) are SEM and AFM images of 12 nm-thick CoO patterns on SiO_2/Si substrate grown by AS-ALD, respectively. (c) and (d) are SEM and AFM images of the Co patterns on SiO_2/Si substrate after atomic deuterium reduction of CoO followed by 2 nm MBE Al capping layer deposited on top, respectively.

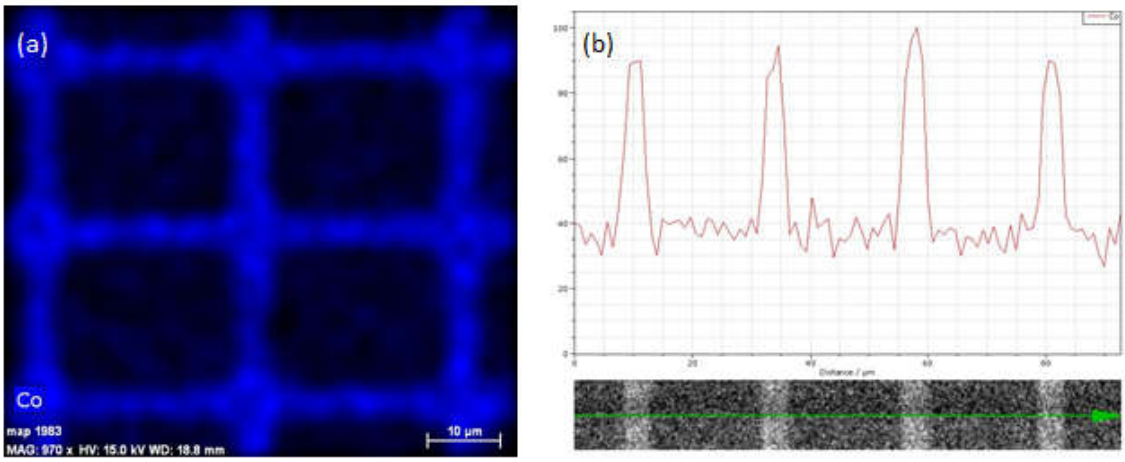

Figure 5.5. (a) and (b) are elemental mapping and line analysis of the CoO patterns on SiO_2/Si substrate shown in Figure 5.4, respectively, in which Co element was scanned.

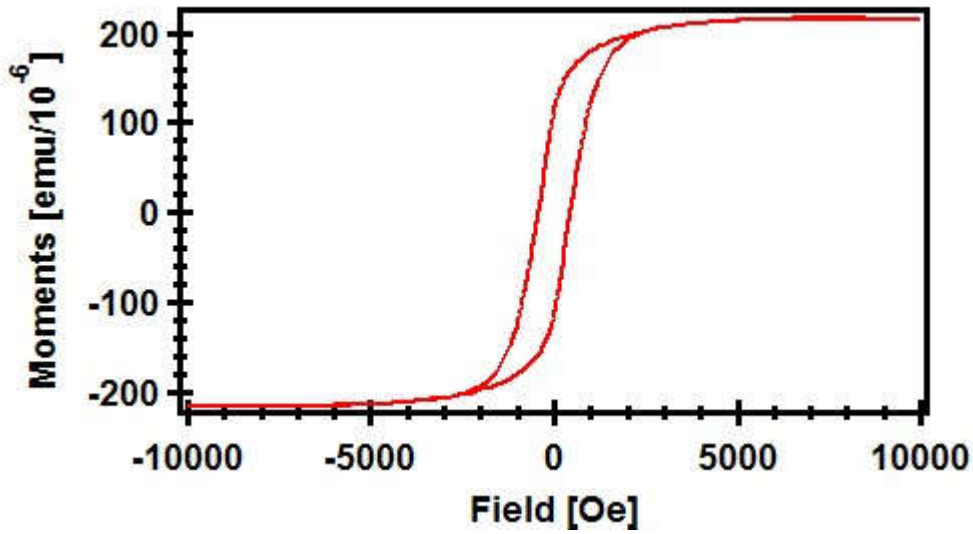

Figure 5.6. The magnetization hysteresis loop of the Al_2O_3-capped Co patterns produced from the atomic deuterium reduction of 12 nm-thick CoO patterns on SiO_2/Si substrate. The data has been corrected with the cancellation of the base signal of the substrate and the capping layer.

Similar results of AS-ALD of CoO and Co patterns were also realized on MgO(001) substrate. 18 nm-thick CoO was grown on the PS template/MgO(001) by ALD at ~180 °C and then the PS template was removed by O_2 plasma etching. Figure 5.7a and 5.7b show the SEM and AFM images of the CoO patterns on the MgO(001) substrate after the PS template was removed, respectively. In Figure 5.7a, the relatively dark regions are the CoO bars while the relatively bright regions belong to the MgO(001) substrate. In Figure 5.7b, the relatively bright regions are the CoO bars while the relatively dark regions belong to the MgO(001) substrate, which means the CoO bars are higher the SiO_2/Si substrate. The CoO only grew on the bar regions that were not covered by the PS squares. The CoO bar patterns are uniform across the patterned area and their feature size (~6 μm wide) is very close to the original feature size (6 μm wide) of shadow mask. The CoO patterns were confirmed by elemental analysis results as shown in Figure 5.8. Figure 5.8a and 5.8b show the elemental mapping and line analysis of the CoO patterns, respectively, in which Co element was scanned. Both of them indicate the Co element is only present on the bar regions. The CoO was further reduced to metallic Co by 2 h atomic deuterium reduction at 220 °C and the Co layer was not covered by Al capping layer in this experiment. Due to the lack of Al capping layer, the Co were reoxidized to CoO during *ex-situ* SEM and AFM characterization. There should not be much difference between the morphology of Co films and reoxidized CoO films based on the results of Chapter 3. Figure 5.7c and 5.7d show the SEM and AFM images of the Co patterns (actually reoxidized CoO) on the MgO(001) substrate. In Figure 5.7c, the relatively bright regions are the Co bars (actually reoxidized CoO) while the relatively

dark regions belong to the MgO(001) substrate. In Figure 5.7d, the relatively bright regions are the Co bars (actually reoxidized CoO) while the relatively dark regions belong to the MgO(001) substrate. The Co patterns (actually reoxidized CoO) are almost the same with the CoO patterns in the x- and y-directions and there is no deformation caused by reduction and reoxidation. The difference in the z-direction comes from the thickness contraction from CoO to Co.

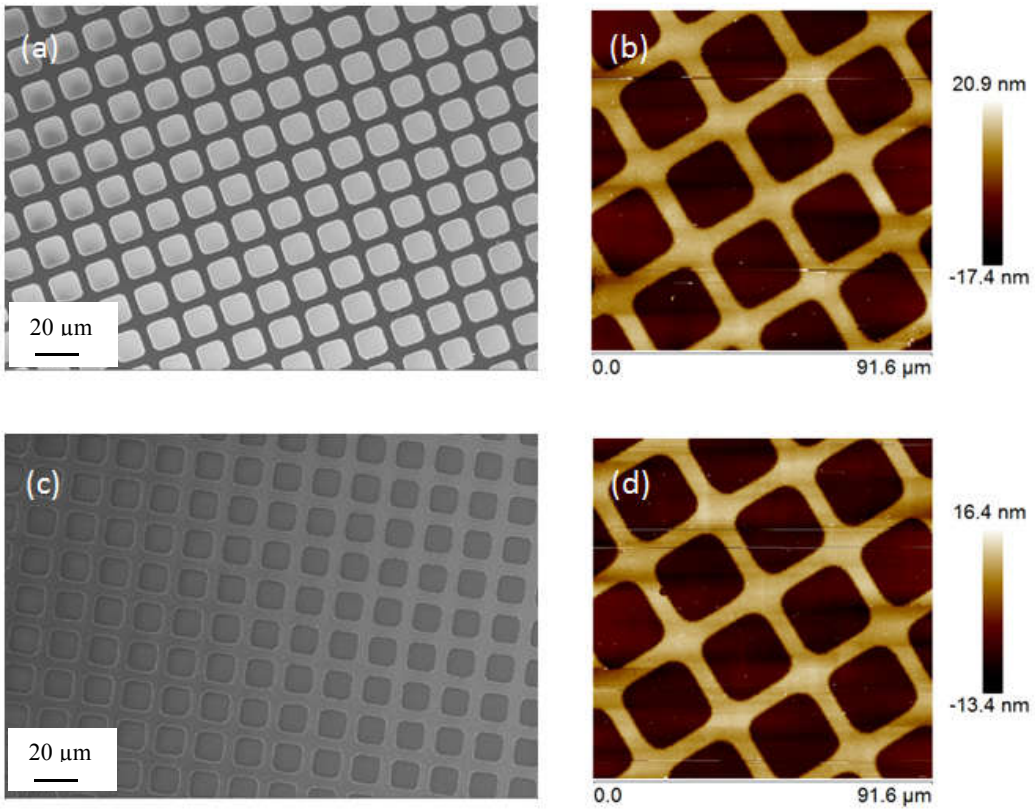

Figure 5.7. (a) and (b) are SEM and AFM images of 18 nm-thick CoO patterns on MgO(001) substrate grown by AS-ALD, respectively. (c) and (d) are SEM and AFM images of the Co patterns on MgO(001) substrate after atomic deuterium reduction of CoO, respectively.

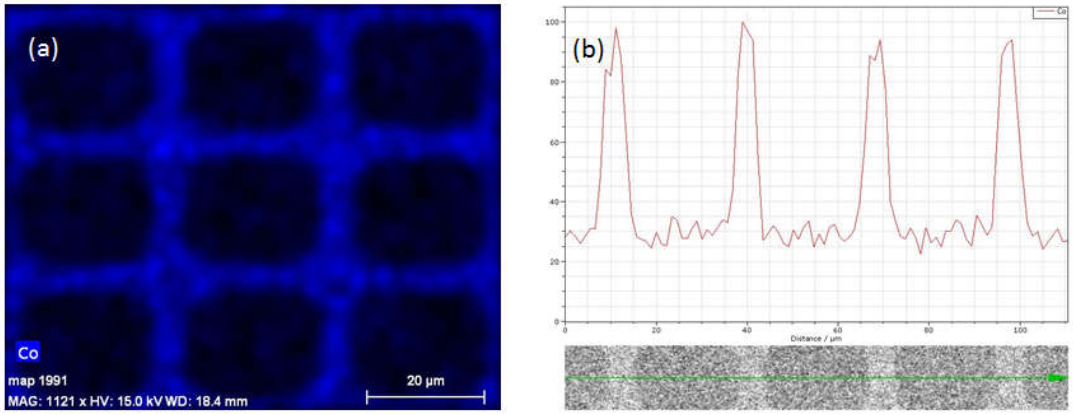

Figure 5.8. (a) and (b) are the elemental mapping and line analysis of the CoO patterns on MgO(001) substrate shown in Figure 5.7, respectively, in which Co element was scanned.

PS nano-patterns were created by directed self-assembly of PMMA-PS diblock copolymer. 50 nm-thick PMMA formed cylinders aligned perpendicular to the SiO_2/Si substrate and PS formed a matrix. There was a 3 nm-thick brush layer (PMMA-PS random copolymer) between the diblock copolymer film and the SiO_2/Si substrate to neutralize the substrate. The PMMA cylinders and underlying brush layer were removed by CO_2/Ar plasma etching to generate nano-patterns of PS with 20-30 nm holes and 40-50 nm pitch on the substrate, as shown in Figure 5.9. Figure 5.9a and 5.9b are top-down and cross-section SEM images of the as-prepared PS hole-patterns, respectively. The relatively bright regions belong to the PS matrix and the relatively dark regions are the empty holes. The critical requirement for CoO ALD is a starting surface that features hydroxyl groups favoring the nucleation and growth of CoO. Therefore the complete removal of PMMA cylinders and underlying brush layer by plasma etching is the key to the successful AS-ALD of CoO within the holes. When the holes were not cleaned enough, the residues of

PMMA or the brush layer blocked the nucleation and film growth of CoO and there was nothing left after 400 CoO ALD cycles (sufficient to deposit 12-nm of CoO) and polymer removal, as shown in Figure 5.9c. On the other hand, when the holes were cleaned too much, the PS matrix was also etched too much and the remaining PS matrix was very thin and low. In this case, there was lateral overgrowth of CoO over the top the PS matrix after 400 CoO ALD cycles and polymer removal, as shown in Figure 5.9d. When the etch was controlled within a proper window, clean holes were generated without damaging the PS matrix too much. Figure 5.9e shows the top-down SEM image of the CoO dots grown on holes after 400 CoO ALD cycles. The holes were filled with materials compared to empty holes of as-prepared PS patterns shown in Figure 5.9a. Then after removing the PS matrix, there were CoO dots remaining on the SiO_2/Si substrate, as shown in Figure 5.9f.

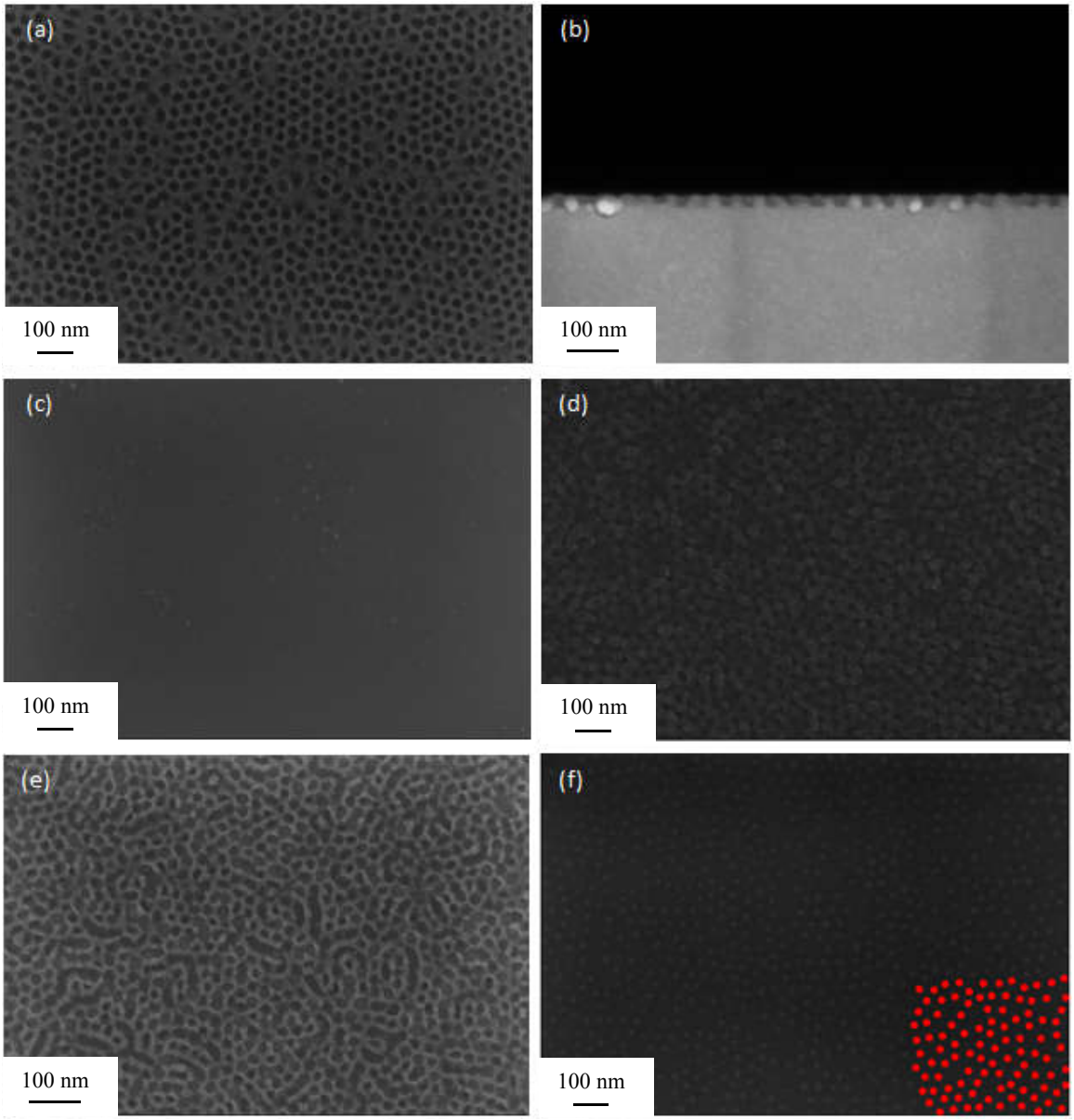

Figure 5.9. (a) and (b) are top-down and cross-section SEM images of the as-prepared PS hole-patterns, respectively. (c) SEM image of the under-etched PS hole-patterns after 400 CoO ALD cycles and polymer removal. (d) SEM image of the over-etched PS hole-patterns after 400 CoO ALD cycles and polymer removal. (e) SEM image of the properly-etched PS hole-patterns after 400 CoO ALD cycles. (f) SEM image of the properly-etched PS hole-patterns after 400 CoO ALD cycles and polymer removal. The CoO dots have been colored red in the lower-right region to help see the pattern.

5.4 CONCLUSIONS

We report the area-selective deposition of cobalt (II) oxide on polystyrene-patterned SiO_2/Si and MgO(001) substrates at a temperature of 170–180 °C by atomic layer deposition. The resulting CoO patterns are carbon-free and smooth. And the CoO patterns can be further reduced to produce metallic Co patterns without deformation by using atomic deuterium reduction at 220 °C. The critical requirement for metal oxide ALD is a starting surface that features hydroxyl groups favoring the nucleation and growth of metal oxides. Consisting of only C and H elements, polystyrene is very effective in inhibiting the nucleation of film growth of CoO. The polystyrene was patterned using UV-crosslinked 40-nm PS films or using self-assembled 50-nm polystyrene-polymethylmethacrylate films. The unexposed PS in UV-crosslinked PS films was dissolved away with toluene or the PMMA component in self-assembled PS-PMMA films was removed by plasma etching to expose the underlying oxide surface.

5.5 REFERENCES

1. Neisser, M. & Wurm, S. ITRS lithography roadmap: 2015 challenges. *Adv. Opt. Technol.* **4,** 235–240 (2015).
2. Boullart, W. *et al.* STT MRAM patterning challenges. in *Advanced Etch Technology for Nanopatterning II* **8685,** 86850F (International Society for Optics and Photonics, 2013).
3. Chawla, J. S. *et al.* Patterning challenges in the fabrication of 12 nm half-pitch dual damascene copper ultra low-k interconnects. in *Advanced Etch Technology for Nanopatterning III* **9054,** 905404 (International Society for Optics and Photonics, 2014).
4. Eom, T.-S. *et al.* Patterning challenges of EUV lithography for 1X-nm node DRAM and beyond. in *Extreme Ultraviolet (EUV) Lithography IV* **8679,** 86791J (International Society for Optics and Photonics, 2013).
5. Hontake, K. *et al.* Coater/developer based techniques to improve high-resolution EUV patterning defectivity. in *International Conference on Extreme Ultraviolet*

Lithography 2017 **10450,** 104501U (International Society for Optics and Photonics, 2017).

6. Burkhardt, M. Investigation of alternate mask absorbers in EUV lithography. in *Extreme Ultraviolet (EUV) Lithography VIII* **10143,** 1014312 (International Society for Optics and Photonics, 2017).

7. Bakshi, V., Mizoguchi, H., Liang, T., Grenville, A. & Benschop, J. P. Special Section Guest Editorial: EUV Lithography for the 3-nm Node and Beyond. *J. MicroNanolithography MEMS MOEMS* **16,** 41001 (2017).

8. Metz, A. W. *et al.* Overcoming etch challenges related to EUV based patterning. in *Advanced Etch Technology for Nanopatterning VI* **10149,** 1014906 (International Society for Optics and Photonics, 2017).

9. M. F. Shieh, C. M Lai, K. H Hsieh, R. G. Liu & S. M. Chang. Self aligned patterning with multiple resist layers. (2017).

10. C. W. Lu, C. J. Lee & S. L. Shue. Method of forming multiple patterning spacer structures. (2017).

11. Mallik, A. *et al.* The need for EUV lithography at advanced technology for sustainable wafer cost. in *Extreme Ultraviolet (EUV) Lithography IV* **8679,** 86792Y (International Society for Optics and Photonics, 2013).

12. Lu, W. & Lieber, C. M. Nanoelectronics from the bottom up. *Nat. Mater.* **6,** 841–850 (2007).

13. Xia, Y., Rogers, J. A., Paul, K. E. & Whitesides, G. M. Unconventional Methods for Fabricating and Patterning Nanostructures. *Chem. Rev.* **99,** 1823–1848 (1999).

14. Ozin, G. A. *et al.* Nanofabrication by self-assembly. *Mater. Today* **12,** 12–23 (2009).

15. Dong, W. *et al.* Application of three-dimensionally area-selective atomic layer deposition for selectively coating the vertical surfaces of standing nanopillars. *Sci. Rep.* **4,** 4458 (2014).

16. Fang, M. & Ho, J. C. Area-Selective Atomic Layer Deposition: Conformal Coating, Subnanometer Thickness Control, and Smart Positioning. *ACS Nano* **9,** 8651–8654 (2015).

17. Thissen, N. F. W. *et al.* Graphene devices with bottom-up contacts by area-selective atomic layer deposition. *2D Mater.* **4,** 25046 (2017).

18. Yan, K. *et al.* Selective deposition and stable encapsulation of lithium through heterogeneous seeded growth. *Nat. Energy* **1,** 16010 (2016).

19. Haider, A., Yilmaz, M., Deminskyi, P., Eren, H. & Biyikli, N. Nanoscale selective area atomic layer deposition of TiO 2 using e-beam patterned polymers. *RSC Adv.* **6,** 106109–106119 (2016).

20. Mameli, A. *et al.* Area-Selective Atomic Layer Deposition: Role of Surface Chemistry. *ECS Trans.* **80,** 39–48 (2017).

21. George, S. M. Atomic Layer Deposition: An Overview. *Chem. Rev.* **110,** 111–131 (2010).

22. Kim, W.-H. *et al.* Atomic Layer Deposition of Ni Thin Films and Application to Area-Selective Deposition. *J. Electrochem. Soc.* **158,** D1–D5 (2011).

23. Mackus, A. J. M., Bol, A. A. & Kessels, W. M. M. The use of atomic layer deposition in advanced nanopatterning. *Nanoscale* **6,** 10941–10960 (2014).

24. Mameli, A. *et al.* Area-Selective Atomic Layer Deposition of In2O3:H Using a μ-Plasma Printer for Local Area Activation. *Chem. Mater.* **29,** 921–925 (2017).

25. Vervuurt, R. H. J., Sharma, A., Jiao, Y., Kessels, W. (Erwin) M. M. & Bol, A. A. Area-selective atomic layer deposition of platinum using photosensitive polyimide. *Nanotechnology* **27,** 405302 (2016).

26. Hoeppener, S. *et al.* Metal Nanoparticles, Nanowires, and Contact Electrodes Self-Assembled on Patterned Monolayer Templates—A Bottom-up Chemical Approach. *Adv. Mater.* **14,** 1036–1041 (2002).

27. Park, M. H., Jang, Y. J., Sung-Suh, H. M. & Sung, M. M. Selective Atomic Layer Deposition of Titanium Oxide on Patterned Self-Assembled Monolayers Formed by Microcontact Printing. *Langmuir* **20,** 2257–2260 (2004).

28. Chen, R., Kim, H., McIntyre, P. C., Porter, D. W. & Bent, S. F. Achieving area-selective atomic layer deposition on patterned substrates by selective surface modification. *Appl. Phys. Lett.* **86,** 191910 (2005).

29. Chen, R., Kim, H., McIntyre, P. C. & Bent, S. F. Self-assembled monolayer resist for atomic layer deposition of HfO2 and ZrO2 high-κ gate dielectrics. *Appl. Phys. Lett.* **84,** 4017–4019 (2004).

30. Jiang, X. & Bent, S. F. Area-Selective Atomic Layer Deposition of Platinum on YSZ Substrates Using Microcontact Printed SAMs. *J. Electrochem. Soc.* **154,** D648–D656 (2007).

31. Minaye Hashemi, F. S., Prasittichai, C. & Bent, S. F. Self-Correcting Process for High Quality Patterning by Atomic Layer Deposition. *ACS Nano* **9,** 8710–8717 (2015).

32. Hashemi, F. S. M., Prasittichai, C. & Bent, S. F. A New Resist for Area Selective Atomic and Molecular Layer Deposition on Metal–Dielectric Patterns. *J. Phys. Chem. C* **118,** 10957–10962 (2014).

33. Chopra, S. N., Zhang, Z., Kaihlanen, C. & Ekerdt, J. G. Selective Growth of Titanium Nitride on HfO2 across Nanolines and Nanopillars. *Chem. Mater.* **28,** 4928–4934 (2016).

34. Hashemi, F. S. M. & Bent, S. F. Sequential Regeneration of Self-Assembled Monolayers for Highly Selective Atomic Layer Deposition. *Adv. Mater. Interfaces* **3,** 1600464 (2016).

35. Sinha, A., Hess, D. W. & Henderson, C. L. Area selective atomic layer deposition of titanium dioxide: Effect of precursor chemistry. *J. Vac. Sci. Technol. B Microelectron. Nanometer Struct. Process. Meas. Phenom.* **24,** 2523–2532 (2006).

36. Hua, Y., King, W. P. & Henderson, C. L. Nanopatterning materials using area selective atomic layer deposition in conjunction with thermochemical surface modification via heated AFM cantilever probe lithography. *Microelectron. Eng.* **85,** 934–936 (2008).

37. Ellinger, C. R. & Nelson, S. F. Selective Area Spatial Atomic Layer Deposition of ZnO, Al2O3, and Aluminum-Doped ZnO Using Poly(vinyl pyrrolidone). *Chem. Mater.* **26,** 1514–1522 (2014).

38. Färm, E., Kemell, M., Santala, E., Ritala, M. & Leskelä, M. Selective-Area Atomic Layer Deposition Using Poly(vinyl pyrrolidone) as a Passivation Layer. *J. Electrochem. Soc.* **157,** K10–K14 (2010).

39. Mullings, M. N. *et al.* Area Selective Atomic Layer Deposition by Microcontact Printing with a Water-Soluble Polymer. *J. Electrochem. Soc.* **157,** D600–D604 (2010).

40. Nie, Z. & Kumacheva, E. Patterning surfaces with functional polymers. *Nat. Mater.* **7,** 277–290 (2008).

41. Bui, V.-T., Lee, H. S., Choi, J.-H. & Choi, H.-S. Data from crosslinked PS honeycomb thin film by deep UV irradiation. *Data Brief* **5,** 990–994 (2015).

42. Ngo, T. Q. *et al.* Atomic layer deposition of photoactive CoO/SrTiO3 and CoO/TiO2 on Si(001) for visible light driven photoelectrochemical water oxidation. *J. Appl. Phys.* **114,** 84901 (2013).

43. Li, W. Y., Xu, L. N. & Chen, J. Co3O4 Nanomaterials in Lithium-Ion Batteries and Gas Sensors. *Adv. Funct. Mater.* **15,** 851–857 (2005).

44. Hou, C., Xu, Q., Yin, L. & Hu, X. Metal–organic framework templated synthesis of Co3O4 nanoparticles for direct glucose and H2O2 detection. *Analyst* **137,** 5803–5808 (2012).

45. Liang, Y. *et al.* Co_3O_4 nanocrystals on graphene as a synergistic catalyst for oxygen reduction reaction. *Nat. Mater.* **10,** 780–786 (2011).

46. Natile, M. M. & Glisenti, A. Study of Surface Reactivity of Cobalt Oxides: Interaction with Methanol. *Chem. Mater.* **14,** 3090–3099 (2002).

47. Yu, X.-Y. *et al.* Facet-dependent electrochemical properties of Co_3O_4 nanocrystals toward heavy metal ions. *Sci. Rep.* **3,** 2886 (2013).

48. Kohn, A., Eizenberg, M. & Shacham-Diamand, Y. Copper grain boundary diffusion in electroless deposited cobalt based films and its influence on diffusion barrier integrity for copper metallization. *J. Appl. Phys.* **94,** 3015–3024 (2003).

49. Kokaze, Y. *et al.* Performance of Integrated Cu Gap-Filling Process with Chemical Vapor Deposition Cobalt Liner. *Jpn. J. Appl. Phys.* **52,** 05FA01 (2013).

50. Yuasa, S. & Djayaprawira, D. D. Giant tunnel magnetoresistance in magnetic tunnel junctions with a crystalline MgO(0 0 1) barrier. *J. Phys. Appl. Phys.* **40,** R337 (2007).

51. Ikeda, S. *et al.* A perpendicular-anisotropy CoFeB–MgO magnetic tunnel junction. *Nat. Mater.* **9,** 721–724 (2010).

52. K. M. Wu, K. W. Cheng, C. Y. Tsai & C. S. Tsai. Magnetoresistive random access memory cell and fabricating the same. (2015).

53. Parkin, S. *et al.* Magnetically engineered spintronic sensors and memory. *Proc. IEEE* **91,** 661–680 (2003).

54. Carvello, B. *et al.* Sizable room-temperature magnetoresistance in cobalt based magnetic tunnel junctions with out-of-plane anisotropy. *Appl. Phys. Lett.* **92,** 102508 (2008).

55. Bischler, U. & Bertel, E. Simple source of atomic hydrogen for ultrahigh vacuum applications. *J. Vac. Sci. Technol. A* **11,** 458–460 (1993).

56. Chuang, T. J., Brundle, C. R. & Rice, D. W. Interpretation of the x-ray photoemission spectra of cobalt oxides and cobalt oxide surfaces. *Surf. Sci.* **59,** 413–429 (1976).

57. Palacios, M., García, O. & Rodríguez-Hernández, J. Constructing Robust and Functional Micropatterns on Polystyrene Surfaces by Using Deep UV Irradiation. *Langmuir* **29,** 2756–2763 (2013).

Chapter 6: Research Summary

6.1 SUMMARY

This research focuses on process development to realize the area-selective deposition of ferromagnetic cobalt films on insulating tunnel oxides as a step toward fabrication of a magnetic tunnel junction.

Ultrathin CoO films were deposited on MgO(001) and SiO_2/Si(001) substrates at ~180 °C by atomic layer deposition using bis(N-*tert* butyl, N'-ethylpropionamidinato) cobalt (II) and deionized water as co-reactants. The CoO films grown on amorphous SiO_2/Si(001) substrates are polycrystalline while the CoO films grown on crystalline MgO(001) substrates are single-crystalline. High temperature (~400 °C) thermal reduction of CoO films caused dewetting problem and led to formation of disconnected Co islands. In order to suppress dewetting, two low temperature (~200 °C) reduction methods were studied including atomic deuterium reduction and the use of metallic Al as an O scavenger layer. Being effective in suppressing dewetting, the two low temperature reduction methods produced smooth and continuous Co films. The Co films are carbon-free and ferromagnetic. The Co films produced by high temperature reduction exhibit higher coercivity than the Co films produced by low temperature reduction due to there are much more voids in the former Co films impeding the magnetic reversal.

It was noticed that reduction conditions affected the microstructure and the magnetic properties of the resulting Co films. In order to gain the capability of tuning magnetic properties of Co films and realize specific properties for various applications, the process-structure-magnetic property relationship was elucidated. A series of atomic

deuterium reductions of CoO at various reaction temperature, reaction pressure, reaction time and underlying substrates were conducted. The film composition, microstructure, and magnetic property of the resulting Co films were characterized by X-ray photoelectron spectroscopy, atomic force microscopy, and vibrating sample magnetometry, respectively. The increase of reaction temperature, partial pressure of deuterium, and reaction time increases the average grain size and the roughness of the Co films. Co films with larger average grain size show higher coercivity. Co films that are grown on substrates with lower degree of dewetting tendency, such as MgO and Al_2O_3, show smaller average grain size and smaller coercivity. Film coercivity from tens to hundreds Oersted can be achieved by tuning the process parameters.

Polystyrene (PS) films were investigated to work as the passivation material and guide the area-selective deposition of CoO and Co films on MgO(001) and SiO_2/Si(001) substrates. Consisting only C and H elements, PS was proved to be effective in inhibiting the nucleation and film growth of CoO which rely on reactive hydroxyl sites of the substrate surface. The polystyrene was patterned using UV-crosslinked 40-nm PS films or using self-assembled 50-nm polystyrene-polymethylmethacrylate (PS-PMMA) films. The unexposed PS in UV-crosslinked PS films was dissolved away with toluene or the PMMA component in self-assembled PS-PMMA films was removed by a CO_2/Ar plasma etching to expose the underlying oxide surface. Then the substrates pre-patterned with PS were exposed to CoO ALD cycles at ~180 °C using bis(N-*tert* butyl, N'-ethylpropionamidinato) cobalt (II) and deionized water as co-reactants. As confirmed by scanning electron microscopy, atomic force microscopy, and energy dispersive X-ray

spectroscopy, CoO patterns only grew on the regions that were not covered by PS. And the CoO patterns can be further reduced to produce Co patterns without deformation by using atomic deuterium reduction at 220 °C.

6.2 RECOMMENDATIONS FOR FUTURE WORK

Cobalt is a classic ferromagnetic material but it is a little bit old-fashioned. Metal alloys, such as CoFe and NiFe, exhibit exciting magnetic and catalytic properties and draw increasing research attention.[1–16] There are rare reports of the growth of metal alloy films by ALD. We have successfully deposited FeO and NiO films on oxide substrates by low temperature thermal ALD using bis(N,N'-di-t-butylacetamidinato) iron(II) and bis(N,N'-di-t-butylacetamidinato) nickel(II) precursors, respectively. Based on this experience, $Co_xFe_yO_z$ and $Ni_xFe_yO_z$ ternary compounds could be deposited by ALD and the component ratio could be tuned by tuning the cycle ratio of each component. Then the general atomic deuterium reduction method could be employed to produce Co_xFe_y and Ni_xFe_y films by reducing $Co_xFe_yO_z$ and $Ni_xFe_yO_z$, respectively. With the tuning of component ratio and reduction condition, metal alloy films with a broad range of magnetic properties could be expected.

In addition to the ferromagnetic layers, the ultrathin insulating tunnel barrier layer could be deposited by ALD, too. Due to its self-limiting behavior of the sequential process, ALD has the advantages of monolayer-level thickness control and excellent conformity. The minimum thickness of ALD grown pinhole-free Al_2O_3 is smaller than that of sputtered pinhole-free Al_2O_3.[17] The low temperature ALD processes of both MgO

and Al_2O_3 films are available and minor changes to the recipes may be needed to deposit ultrathin pinhole-free single-crystal tunnel oxide films meeting the requirements of MTJ application.[18–21] Then an entire MTJ stack like Co/MgO/Co could be deposited by ALD and its device performance could be compared with the sputtered MTJ stack.

Dewetting of metal films on metal oxide substrates is unwanted when continuous metal films are required. In addition to the method of lowering process temperature employed in this work, other methods suppressing dewetting include the use of a capping layer, the use of an adsorbate layer, and the use of an additive to facilitate the wetting of metal films over metal oxide substrates. Our recent experiments have confirmed that the existence of an Al_2O_3 capping layer on the top of CoO during reduction process lowered the resulting Co film roughness effectively. It is reported that NH_3 gas helps to wet substrates.[22] A reduction study of CoO using ammonia gas as the reducing agent should be helpful. Combining the effective methods together may give us the best solution to suppressing dewetting.

Polystyrene has been proved to be effective in inhibiting the nucleation and film growth of CoO on oxide substrates. We expect to confirm PS can work as a universal platform for selective deposition of metal oxide films. Our recent experiments have showed PS worked well for the selective deposition of $BaTiO_3$ and SnO_2 on oxide substrates. Another useful study is to explore the limits of the PS passivation, such as the maximum ALD cycles it could stand before failure and the reaction conditions leading to its failure. Optimization of the PS patterning processes including photolithography and directed self-assembly is expected to conduct to improve the uniformity of patterns and

the fidelity of the pattern transfer. The optimization could focus on the UV-light exposure process and the plasma etching process to prepare clean regions of substrates for film growth. Other PS patterning methods could also be explored to realize patterns of various sizes and shapes.

6.3 REFERENCES

1. Peng, S. *et al.* Giant interfacial perpendicular magnetic anisotropy in MgO/CoFe/capping layer structures. *Appl. Phys. Lett.* **110,** 72403 (2017).
2. Yang, H., Yang, S.-H. & Parkin, S. The role of Mg interface layer in MgO magnetic tunnel junctions with CoFe and CoFeB electrodes. *AIP Adv.* **2,** 12150 (2012).
3. Anderson, G., Huai, Y. & Miloslawsky, L. CoFe/IrMn exchange biased top, bottom, and dual spin valves. *J. Appl. Phys.* **87,** 6989–6991 (2000).
4. Mizunuma, K. *et al.* MgO barrier-perpendicular magnetic tunnel junctions with CoFe/Pd multilayers and ferromagnetic insertion layers. *Appl. Phys. Lett.* **95,** 232516 (2009).
5. Monso, S. *et al.* Crossover from in-plane to perpendicular anisotropy in Pt/CoFe/AlOx sandwiches as a function of Al oxidation: A very accurate control of the oxidation of tunnel barriers. *Appl. Phys. Lett.* **80,** 4157–4159 (2002).
6. Osaka, T., Yokoshima, T., Shiga, D., Imai, K. & Takashima, K. A High Moment CoFe Soft Magnetic Thin Film Prepared by Electrodeposition. *Electrochem. Solid-State Lett.* **6,** C53–C55 (2003).
7. Pakala, M., Huai, Y., Anderson, G. & Miloslavsky, L. Effect of underlayer roughness, grain size, and crystal texture on exchange coupled IrMn/CoFe thin films. *J. Appl. Phys.* **87,** 6653–6655 (2000).
8. Sun, M., Medina, J. A., Sasaki, K. Y. & Jiang, M. Method and system for providing high magnetic flux saturation CoFe films. (2014).
9. Wang, W., Sukegawa, H., Shan, R., Mitani, S. & Inomata, K. Giant tunneling magnetoresistance up to 330% at room temperature in sputter deposited Co2FeAl/MgO/CoFe magnetic tunnel junctions. *Appl. Phys. Lett.* **95,** 182502 (2009).
10. Zhou, X. W., Johnson, R. A. & Wadley, H. N. G. Misfit-energy-increasing dislocations in vapor-deposited CoFe/NiFe multilayers. *Phys. Rev. B* **69,** 144113 (2004).

11. Hylton, T. L., Coffey, K. R., Parker, M. A. & Howard, J. K. Giant Magnetoresistance at Low Fields in Discontinuous NiFe-Ag Multilayer Thin Films. *Science* **261,** 1021–1024 (1993).

12. Li, J., Zhao, C., Feng, C., Zhou, Z. & Yu, G. Impact of interface manipulation of oxide on electrical transport properties and low-frequency noise in MgO/NiFe/MgO heterojunctions. *AIP Adv.* **5,** 87139 (2015).

13. Nan, T. *et al.* Comparison of spin-orbit torques and spin pumping across NiFe/Pt and NiFe/Cu/Pt interfaces. *Phys. Rev. B* **91,** 214416 (2015).

14. Sitthisa, S., An, W. & Resasco, D. E. Selective conversion of furfural to methylfuran over silica-supported NiFe bimetallic catalysts. *J. Catal.* **284,** 90–101 (2011).

15. Dionigi, F. & Strasser, P. NiFe-Based (Oxy)hydroxide Catalysts for Oxygen Evolution Reaction in Non-Acidic Electrolytes. *Adv. Energy Mater.* **6,** 1600621 (2016).

16. Gong, M. & Dai, H. A mini review of NiFe-based materials as highly active oxygen evolution reaction electrocatalysts. *Nano Res.* **8,** 23–39 (2015).

17. Martin, M.-B. *et al.* Sub-nanometer Atomic Layer Deposition for Spintronics in Magnetic Tunnel Junctions Based on Graphene Spin-Filtering Membranes. *ACS Nano* **8,** 7890–7895 (2014).

18. Burton, B. B., Goldstein, D. N. & George, S. M. Atomic Layer Deposition of MgO Using Bis(ethylcyclopentadienyl)magnesium and H2O. *J. Phys. Chem. C* **113,** 1939–1946 (2009).

19. Ryu, S. W., Song, J.-G., Kim, H. G., Kim, H. & Lee, H.-B.-R. Interlayer-assisted atomic layer deposition of MgO as a magnetic tunneling junction insulators. *J. Alloys Compd.* **747,** 505–510 (2018).

20. Groner, M. D., Fabreguette, F. H., Elam, J. W. & George, S. M. Low-Temperature Al2O3 Atomic Layer Deposition. *Chem. Mater.* **16,** 639–645 (2004).

21. Groner, M. D., Elam, J. W., Fabreguette, F. H. & George, S. M. Electrical characterization of thin Al2O3 films grown by atomic layer deposition on silicon and various metal substrates. *Thin Solid Films* **413,** 186–197 (2002).

22. Liao, W. & Ekerdt, J. G. Ru nucleation and thin film smoothness improvement with ammonia during chemical vapor deposition. *J. Vac. Sci. Technol. A* **34,** 31508 (2016).

Bibliography

1. Waldrop, M. M. The chips are down for Moore's law. *Nat. News* **530,** 144 (2016).
2. Kawahara, T., Ito, K., Takemura, R. & Ohno, H. Spin-transfer torque RAM technology: Review and prospect. *Microelectron. Reliab.* **52,** 613–627 (2012).
3. Chen, E. *et al.* Advances and Future Prospects of Spin-Transfer Torque Random Access Memory. *IEEE Trans. Magn.* **46,** 1873–1878 (2010).
4. Wang, K. L., Alzate, J. G. & Amiri, P. K. Low-power non-volatile spintronic memory: STT-RAM and beyond. *J. Phys. Appl. Phys.* **46,** 74003 (2013).
5. Zhang, Y., Zhang, L., Wen, W., Sun, G. & Chen, Y. Multi-level cell STT-RAM: Is it realistic or just a dream? in *2012 IEEE/ACM International Conference on Computer-Aided Design (ICCAD)* 526–532 (2012).
6. Ikeda, S. *et al.* Magnetic Tunnel Junctions for Spintronic Memories and Beyond. *IEEE Trans. Electron Devices* **54,** 991–1002 (2007).
7. Driskill-Smith, A. *et al.* Latest Advances and Roadmap for In-Plane and Perpendicular STT-RAM. in *2011 3rd IEEE International Memory Workshop (IMW)* 1–3 (2011). doi:10.1109/IMW.2011.5873205
8. Telepinsky, Y. *et al.* Towards a six-state magnetic memory element. *Appl. Phys. Lett.* **108,** 182401 (2016).
9. Pramanik, T., Roy, U., Register, L. F. & Banerjee, S. K. Proposal of a Multistate Memory Using Voltage Controlled Magnetic Anisotropy of a Cross-Shaped Ferromagnet. *IEEE Trans. Nanotechnol.* **14,** 883–888 (2015).
10. Gates, B. D. *et al.* New Approaches to Nanofabrication: Molding, Printing, and Other Techniques. *Chem. Rev.* **105,** 1171–1196 (2005).
11. Xue, L. *et al.* A Self-Aligned Two-Step Reactive Ion Etching Process for Nanopatterning Magnetic Tunnel Junctions on 300 mm Wafers. *IEEE Trans. Magn.* **50,** 1–3 (2014).
12. Gajek, M. *et al.* Spin torque switching of 20 nm magnetic tunnel junctions with perpendicular anisotropy. *Appl. Phys. Lett.* **100,** 132408 (2012).
13. Neisser, M. & Wurm, S. ITRS lithography roadmap: 2015 challenges. *Adv. Opt. Technol.* **4,** 235–240 (2015).
14. Boullart, W. *et al.* STT MRAM patterning challenges. in *Advanced Etch Technology for Nanopatterning II* **8685,** 86850F (International Society for Optics and Photonics, 2013).
15. Chawla, J. S. *et al.* Patterning challenges in the fabrication of 12 nm half-pitch dual damascene copper ultra low-k interconnects. in *Advanced Etch Technology for Nanopatterning III* **9054,** 905404 (International Society for Optics and

Photonics, 2014).

16. Eom, T.-S. *et al.* Patterning challenges of EUV lithography for 1X-nm node DRAM and beyond. in *Extreme Ultraviolet (EUV) Lithography IV* **8679,** 86791J (International Society for Optics and Photonics, 2013).

17. Hontake, K. *et al.* Coater/developer based techniques to improve high-resolution EUV patterning defectivity. in *International Conference on Extreme Ultraviolet Lithography 2017* **10450,** 104501U (International Society for Optics and Photonics, 2017).

18. Burkhardt, M. Investigation of alternate mask absorbers in EUV lithography. in *Extreme Ultraviolet (EUV) Lithography VIII* **10143,** 1014312 (International Society for Optics and Photonics, 2017).

19. Bakshi, V., Mizoguchi, H., Liang, T., Grenville, A. & Benschop, J. P. Special Section Guest Editorial: EUV Lithography for the 3-nm Node and Beyond. *J. MicroNanolithography MEMS MOEMS* **16,** 41001 (2017).

20. Metz, A. W. *et al.* Overcoming etch challenges related to EUV based patterning. in *Advanced Etch Technology for Nanopatterning VI* **10149,** 1014906 (International Society for Optics and Photonics, 2017).

21. M. F. Shieh, C. M Lai, K. H Hsieh, R. G. Liu & S. M. Chang. Self aligned patterning with multiple resist layers. (2017).

22. C. W. Lu, C. J. Lee & S. L. Shue. Method of forming multiple patterning spacer structures. (2017).

23. Mallik, A. *et al.* The need for EUV lithography at advanced technology for sustainable wafer cost. in *Extreme Ultraviolet (EUV) Lithography IV* **8679,** 86792Y (International Society for Optics and Photonics, 2013).

24. Lu, W. & Lieber, C. M. Nanoelectronics from the bottom up. *Nat. Mater.* **6,** 841–850 (2007).

25. Xia, Y., Rogers, J. A., Paul, K. E. & Whitesides, G. M. Unconventional Methods for Fabricating and Patterning Nanostructures. *Chem. Rev.* **99,** 1823–1848 (1999).

26. Ozin, G. A. *et al.* Nanofabrication by self-assembly. *Mater. Today* **12,** 12–23 (2009).

27. Dong, W. *et al.* Application of three-dimensionally area-selective atomic layer deposition for selectively coating the vertical surfaces of standing nanopillars. *Sci. Rep.* **4,** 4458 (2014).

28. Fang, M. & Ho, J. C. Area-Selective Atomic Layer Deposition: Conformal Coating, Subnanometer Thickness Control, and Smart Positioning. *ACS Nano* **9,** 8651–8654 (2015).

29. Thissen, N. F. W. *et al.* Graphene devices with bottom-up contacts by area-

selective atomic layer deposition. *2D Mater.* **4,** 25046 (2017).

30. Yan, K. *et al.* Selective deposition and stable encapsulation of lithium through heterogeneous seeded growth. *Nat. Energy* **1,** 16010 (2016).

31. Haider, A., Yilmaz, M., Deminskyi, P., Eren, H. & Biyikli, N. Nanoscale selective area atomic layer deposition of TiO 2 using e-beam patterned polymers. *RSC Adv.* **6,** 106109–106119 (2016).

32. Mameli, A. *et al.* Area-Selective Atomic Layer Deposition: Role of Surface Chemistry. *ECS Trans.* **80,** 39–48 (2017).

33. George, S. M. Atomic Layer Deposition: An Overview. *Chem. Rev.* **110,** 111–131 (2010).

34. Miikkulainen, V., Leskelä, M., Ritala, M. & Puurunen, R. L. Crystallinity of inorganic films grown by atomic layer deposition: Overview and general trends. *J. Appl. Phys.* **113,** 21301 (2013).

35. Kim, W.-H. *et al.* Atomic Layer Deposition of Ni Thin Films and Application to Area-Selective Deposition. *J. Electrochem. Soc.* **158,** D1–D5 (2011).

36. Mackus, A. J. M., Bol, A. A. & Kessels, W. M. M. The use of atomic layer deposition in advanced nanopatterning. *Nanoscale* **6,** 10941–10960 (2014).

37. Mameli, A. *et al.* Area-Selective Atomic Layer Deposition of In2O3:H Using a μ-Plasma Printer for Local Area Activation. *Chem. Mater.* **29,** 921–925 (2017).

38. Vervuurt, R. H. J., Sharma, A., Jiao, Y., Kessels, W. (Erwin) M. M. & Bol, A. A. Area-selective atomic layer deposition of platinum using photosensitive polyimide. *Nanotechnology* **27,** 405302 (2016).

39. Hoeppener, S. *et al.* Metal Nanoparticles, Nanowires, and Contact Electrodes Self-Assembled on Patterned Monolayer Templates—A Bottom-up Chemical Approach. *Adv. Mater.* **14,** 1036–1041 (2002).

40. Park, M. H., Jang, Y. J., Sung-Suh, H. M. & Sung, M. M. Selective Atomic Layer Deposition of Titanium Oxide on Patterned Self-Assembled Monolayers Formed by Microcontact Printing. *Langmuir* **20,** 2257–2260 (2004).

41. Chen, R., Kim, H., McIntyre, P. C., Porter, D. W. & Bent, S. F. Achieving area-selective atomic layer deposition on patterned substrates by selective surface modification. *Appl. Phys. Lett.* **86,** 191910 (2005).

42. Chen, R., Kim, H., McIntyre, P. C. & Bent, S. F. Self-assembled monolayer resist for atomic layer deposition of HfO2 and ZrO2 high-κ gate dielectrics. *Appl. Phys. Lett.* **84,** 4017–4019 (2004).

43. Jiang, X. & Bent, S. F. Area-Selective Atomic Layer Deposition of Platinum on YSZ Substrates Using Microcontact Printed SAMs. *J. Electrochem. Soc.* **154,** D648–D656 (2007).

44. Minaye Hashemi, F. S., Prasittichai, C. & Bent, S. F. Self-Correcting Process for High Quality Patterning by Atomic Layer Deposition. *ACS Nano* **9,** 8710–8717 (2015).

45. Hashemi, F. S. M., Prasittichai, C. & Bent, S. F. A New Resist for Area Selective Atomic and Molecular Layer Deposition on Metal–Dielectric Patterns. *J. Phys. Chem. C* **118,** 10957–10962 (2014).

46. Chopra, S. N., Zhang, Z., Kaihlanen, C. & Ekerdt, J. G. Selective Growth of Titanium Nitride on HfO2 across Nanolines and Nanopillars. *Chem. Mater.* **28,** 4928–4934 (2016).

47. Hashemi, F. S. M. & Bent, S. F. Sequential Regeneration of Self-Assembled Monolayers for Highly Selective Atomic Layer Deposition. *Adv. Mater. Interfaces* **3,** 1600464 (2016).

48. Sinha, A., Hess, D. W. & Henderson, C. L. Area selective atomic layer deposition of titanium dioxide: Effect of precursor chemistry. *J. Vac. Sci. Technol. B Microelectron. Nanometer Struct. Process. Meas. Phenom.* **24,** 2523–2532 (2006).

49. Hua, Y., King, W. P. & Henderson, C. L. Nanopatterning materials using area selective atomic layer deposition in conjunction with thermochemical surface modification via heated AFM cantilever probe lithography. *Microelectron. Eng.* **85,** 934–936 (2008).

50. Ellinger, C. R. & Nelson, S. F. Selective Area Spatial Atomic Layer Deposition of ZnO, Al2O3, and Aluminum-Doped ZnO Using Poly(vinyl pyrrolidone). *Chem. Mater.* **26,** 1514–1522 (2014).

51. Färm, E., Kemell, M., Santala, E., Ritala, M. & Leskelä, M. Selective-Area Atomic Layer Deposition Using Poly(vinyl pyrrolidone) as a Passivation Layer. *J. Electrochem. Soc.* **157,** K10–K14 (2010).

52. Mullings, M. N. *et al.* Area Selective Atomic Layer Deposition by Microcontact Printing with a Water-Soluble Polymer. *J. Electrochem. Soc.* **157,** D600–D604 (2010).

53. Nie, Z. & Kumacheva, E. Patterning surfaces with functional polymers. *Nat. Mater.* **7,** 277–290 (2008).

54. Bui, V.-T., Lee, H. S., Choi, J.-H. & Choi, H.-S. Data from crosslinked PS honeycomb thin film by deep UV irradiation. *Data Brief* **5,** 990–994 (2015).

55. Swann, J. M. G. & Topham, P. D. Design and Application of Nanoscale Actuators Using Block-Copolymers. *Polymers* **2,** 454–469 (2010).

56. Ruiz, R. *et al.* Density Multiplication and Improved Lithography by Directed Block Copolymer Assembly. *Science* **321,** 936–939 (2008).

57. Thurn-Albrecht, T. *et al.* Nanoscopic Templates from Oriented Block Copolymer Films. *Adv. Mater.* **12,** 787–791

58. Xu, T. *et al.* The influence of molecular weight on nanoporous polymer films. *Polymer* **42,** 9091–9095 (2001).

59. Kim, K. *et al.* Comparison of Co Films Deposited by Remote Plasma Atomic Layer Deposition Method with Cyclopentadienylcobalt Dicarbonyl [CpCo(CO)2] and Dicobalt Octacarbonyl [Co2(CO)8]. *Jpn. J. Appl. Phys.* **46,** L173 (2007).

60. Yoon, J. *et al.* Atomic Layer Deposition of Co Using N2/H2 Plasma as a Reactant. *J. Electrochem. Soc.* **158,** H1179–H1182 (2011).

61. Park, J. *et al.* Plasma-enhanced atomic layer deposition of Co using Co(MeCp)2 precursor. *J. Energy Chem.* **22,** 403–407 (2013).

62. Lee, H.-B.-R. *et al.* High Quality Area-Selective Atomic Layer Deposition Co Using Ammonia Gas as a Reactant. *J. Electrochem. Soc.* **157,** D10–D15 (2010).

63. Elko-Hansen, T. D.-M., Dolocan, A. & Ekerdt, J. G. Atomic Interdiffusion and Diffusive Stabilization of Cobalt by Copper During Atomic Layer Deposition from Bis(N-tert-butyl-N′-ethylpropionamidinato) Cobalt(II). *J. Phys. Chem. Lett.* **5,** 1091–1095 (2014).

64. Elko-Hansen, T. D.-M. & Ekerdt, J. G. XPS Investigation of the Atomic Layer Deposition Half Reactions of Bis(N-tert-butyl-N′-ethylpropionamidinato) Cobalt(II). *Chem. Mater.* **26,** 2642–2646 (2014).

65. Kwon, J., Saly, M., Halls, M. D., Kanjolia, R. K. & Chabal, Y. J. Substrate Selectivity of (tBu-Allyl)Co(CO)3 during Thermal Atomic Layer Deposition of Cobalt. *Chem. Mater.* **24,** 1025–1030 (2012).

66. Kalutarage, L. C., Martin, P. D., Heeg, M. J. & Winter, C. H. Volatile and Thermally Stable Mid to Late Transition Metal Complexes Containing α-Imino Alkoxide Ligands, a New Strongly Reducing Coreagent, and Thermal Atomic Layer Deposition of Ni, Co, Fe, and Cr Metal Films. *J. Am. Chem. Soc.* **135,** 12588–12591 (2013).

67. Klesko, J. P., Kerrigan, M. M. & Winter, C. H. Low Temperature Thermal Atomic Layer Deposition of Cobalt Metal Films. *Chem. Mater.* **28,** 700–703 (2016).

68. Thompson, C. V. Solid-State Dewetting of Thin Films. *Annu. Rev. Mater. Res.* **42,** 399–434 (2012).

69. Lee, J.-M. & Kim, B.-I. Thermal dewetting of Pt thin film: Etch-masks for the fabrication of semiconductor nanostructures. *Mater. Sci. Eng. A* **449–451,** 769–773 (2007).

70. Müller, C. M. & Spolenak, R. Microstructure evolution during dewetting in thin

Au films. *Acta Mater.* **58,** 6035–6045 (2010).

71. Ye, J. & Thompson, C. V. Mechanisms of complex morphological evolution during solid-state dewetting of single-crystal nickel thin films. *Appl. Phys. Lett.* **97,** 71904 (2010).

72. McDaniel, M. D., Posadas, A., Wang, T., Demkov, A. A. & Ekerdt, J. G. Growth and characterization of epitaxial anatase TiO2(001) on SrTiO3-buffered Si(001) using atomic layer deposition. *Thin Solid Films* **520,** 6525–6530 (2012).

73. Bischler, U. & Bertel, E. Simple source of atomic hydrogen for ultrahigh vacuum applications. *J. Vac. Sci. Technol. A* **11,** 458–460 (1993).

74. McCrate, J. M. & Ekerdt, J. G. Detection of Low-Density Surface Sites on Silica: Experimental Evidence of Intrinsic Oxygen-Vacancy Defects. *Chem. Mater.* **26,** 2166–2171 (2014).

75. Shen Hu. PhD dissertation. (2017).

76. Biesinger, M. C. *et al.* Resolving surface chemical states in XPS analysis of first row transition metals, oxides and hydroxides: Cr, Mn, Fe, Co and Ni. *Appl. Surf. Sci.* **257,** 2717–2730 (2011).

77. Pietsch, U., Holy, V. & Baumbach, T. *High-Resolution X-Ray Scattering: From Thin Films to Lateral Nanostructures*. (Springer Science & Business Media, 2013).

78. Ling, T. *et al.* Engineering surface atomic structure of single-crystal cobalt (II) oxide nanorods for superior electrocatalysis. *Nat. Commun.* **7,** 12876 (2016).

79. Ngo, T. Q. *et al.* Atomic layer deposition of photoactive CoO/SrTiO3 and CoO/TiO2 on Si(001) for visible light driven photoelectrochemical water oxidation. *J. Appl. Phys.* **114,** 84901 (2013).

80. Yang, J. *et al.* Efficient and Sustained Photoelectrochemical Water Oxidation by Cobalt Oxide/Silicon Photoanodes with Nanotextured Interfaces. *J. Am. Chem. Soc.* **136,** 6191–6194 (2014).

81. Li, W. Y., Xu, L. N. & Chen, J. Co3O4 Nanomaterials in Lithium-Ion Batteries and Gas Sensors. *Adv. Funct. Mater.* **15,** 851–857 (2005).

82. Yu, X.-Y. *et al.* Facet-dependent electrochemical properties of Co_3O_4 nanocrystals toward heavy metal ions. *Sci. Rep.* **3,** 2886 (2013).

83. Liang, Y. *et al.* Co_3O_4 nanocrystals on graphene as a synergistic catalyst for oxygen reduction reaction. *Nat. Mater.* **10,** 780–786 (2011).

84. Natile, M. M. & Glisenti, A. Study of Surface Reactivity of Cobalt Oxides: Interaction with Methanol. *Chem. Mater.* **14,** 3090–3099 (2002).

85. Kormondy, K. J. *et al.* Epitaxy of polar semiconductor Co3O4 (110): Growth, structure, and characterization. *J. Appl. Phys.* **115,** 243708 (2014).

86. Vaz, C. A. F. *et al.* Interface and electronic characterization of thin epitaxial Co3O4 films. *Surf. Sci.* **603,** 291–297 (2009).

87. Vaz, C. A. F., Altman, E. I. & Henrich, V. E. Exchange bias and interface electronic structure in Ni/Co3O4 (011). *Phys. Rev. B* **81,** 104428 (2010).

88. Qiao, L. *et al.* Nature of the band gap and origin of the electro-/photo-activity of Co3O4. *J. Mater. Chem. C* **1,** 4628–4633 (2013).

89. Kennedy, R. J. The growth of iron oxide, nickel oxide and cobalt oxide thin films by laser ablation from metal targets. *IEEE Trans. Magn.* **31,** 3829–3831 (1995).

90. Shalini, K., Mane, A. U., Shivashankar, S. A., Rajeswari, M. & Choopun, S. Epitaxial growth of Co3O4 films by low temperature, low pressure chemical vapour deposition. *J. Cryst. Growth* **231,** 242–247 (2001).

91. Fujii, E., Torii, H., Tomozawa, A., Takayama, R. & Hirao, T. Preparation of cobalt oxide films by plasma-enhanced metalorganic chemical vapour deposition. *J. Mater. Sci.* **30,** 6013–6018 (1995).

92. Mane, A. U., Shalini, K., Wohlfart, A., Devi, A. & Shivashankar, S. A. Strongly oriented thin films of Co3O4 deposited on single-crystal MgO(100) by low-pressure, low-temperature MOCVD. *J. Cryst. Growth* **240,** 157–163 (2002).

93. Klepper, K. B., Nilsen, O. & Fjellvåg, H. Growth of thin films of Co3O4 by atomic layer deposition. *Thin Solid Films* **515,** 7772–7781 (2007).

94. Donders, M. E., Knoops, H. C. M., Van, M. C. M., Kessels, W. M. M. & Notten, P. H. L. Remote Plasma Atomic Layer Deposition of Co3O4 Thin Films. *J. Electrochem. Soc.* **158,** G92–G96 (2011).

95. Klepper, K. B., Nilsen, O. & Fjellvåg, H. Epitaxial growth of cobalt oxide by atomic layer deposition. *J. Cryst. Growth* **307,** 457–465 (2007).

96. Diskus, M., Nilsen, O. & Fjellvåg, H. Thin Films of Cobalt Oxide Deposited on High Aspect Ratio Supports by Atomic Layer Deposition. *Chem. Vap. Depos.* **17,** 135–140 (2011).

97. Kokaze, Y. *et al.* Performance of Integrated Cu Gap-Filling Process with Chemical Vapor Deposition Cobalt Liner. *Jpn. J. Appl. Phys.* **52,** 05FA01 (2013).

98. Kohn, A., Eizenberg, M. & Shacham-Diamand, Y. Copper grain boundary diffusion in electroless deposited cobalt based films and its influence on diffusion barrier integrity for copper metallization. *J. Appl. Phys.* **94,** 3015–3024 (2003).

99. R. G. Gordon, H. Kim & H. Bhandari. Cobalt nitride layers for copper interconnects and methods for forming them. (2011).

100. Aubel, O. *et al.* Backend-of-line reliability improvement options for 28nm node technologies and beyond. in *2011 IEEE International Interconnect Technology Conference* 1–3 (2011).

101. Barraud, C. *et al.* Unidirectional Spin-Dependent Molecule-Ferromagnet Hybridized States Anisotropy in Cobalt Phthalocyanine Based Magnetic Tunnel Junctions. *Phys. Rev. Lett.* **114,** 206603 (2015).

102. Kim, W., Kim, K., Parkin, S. S. P., Jeong, J. & Samant, M. G. Magnetic memory device having cobalt-iron-beryllium magnetic layers. (2017).

103. Yuasa, S. & Djayaprawira, D. D. Giant tunnel magnetoresistance in magnetic tunnel junctions with a crystalline MgO(0 0 1) barrier. *J. Phys. Appl. Phys.* **40,** R337 (2007).

104. Ikeda, S. *et al.* A perpendicular-anisotropy CoFeB–MgO magnetic tunnel junction. *Nat. Mater.* **9,** 721–724 (2010).

105. K. M. Wu, K. W. Cheng, C. Y. Tsai & C. S. Tsai. Magnetoresistive random access memory cell and fabricating the same. (2015).

106. Wang, Z. *et al.* Atomic-Scale Structure and Local Chemistry of CoFeB–MgO Magnetic Tunnel Junctions. *Nano Lett.* **16,** 1530–1536 (2016).

107. Schmidt, D. *et al.* Optical, structural, and magnetic properties of cobalt nanostructure thin films. *J. Appl. Phys.* **105,** 113508 (2009).

108. Bergenti, I. *et al.* Magnetic properties of Cobalt thin films deposited on soft organic layers. *J. Magn. Magn. Mater.* **316,** e987–e989 (2007).

109. Presa, B. *et al.* Morphological and magnetic properties of Co nanoparticle thin films grown on Si3N4. *J. Appl. Phys.* **102,** 53901 (2007).

110. Zimmermann, C. G. *et al.* Burrowing of Co Nanoparticles on Clean Cu and Ag Surfaces. *Phys. Rev. Lett.* **83,** 1163–1166 (1999).

111. Tang, F. *et al.* Magnetic properties of Co nanocolumns fabricated by oblique-angle deposition. *J. Appl. Phys.* **93,** 4194–4200 (2003).

112. Deo, N., Bain, M. F., Montgomery, J. H. & Gamble, H. S. Study of magnetic properties of thin cobalt films deposited by chemical vapour deposition. *J. Mater. Sci. Mater. Electron.* **16,** 387–392 (2005).

113. Lee, H.-B.-R. & Kim, H. High-Quality Cobalt Thin Films by Plasma-Enhanced Atomic Layer Deposition. *Electrochem. Solid-State Lett.* **9,** G323–G325 (2006).

114. Lee, H.-B.-R. & Kim, H. Area Selective Atomic Layer Deposition of Cobalt Thin Films. *ECS Trans.* **16,** 219–225 (2008).

115. McDaniel, M. D. *et al.* Growth of epitaxial oxides on silicon using atomic layer deposition: Crystallization and annealing of TiO2 on SrTiO3-buffered Si(001). *J. Vac. Sci. Technol. B* **30,** 04E111 (2012).

116. Chuang, T. J., Brundle, C. R. & Rice, D. W. Interpretation of the x-ray photoemission spectra of cobalt oxides and cobalt oxide surfaces. *Surf. Sci.* **59,** 413–429 (1976).

117. Petitto, S. C. & Langell, M. A. Surface composition and structure of Co3O4(110) and the effect of impurity segregation. *J. Vac. Sci. Technol. Vac. Surf. Films* **22,** 1690–1696 (2004).

118. Bredow, T. & Gerson, A. R. Effect of exchange and correlation on bulk properties of MgO, NiO, and CoO. *Phys. Rev. B* **61,** 5194–5201 (2000).

119. Walsh, A. *et al.* Structural, magnetic, and electronic properties of the Co-Fe-Al oxide spinel system: Density-functional theory calculations. *Phys. Rev. B* **76,** 165119 (2007).

120. Sabat, K. C., Paramguru, R. K., Pradhan, S. & Mishra, B. K. Reduction of Cobalt Oxide (Co3O4) by Low Temperature Hydrogen Plasma. *Plasma Chem. Plasma Process.* **35,** 387–399 (2015).

121. Lide, D. R. Standard thermodynamic properties of chemical substances. *CRC Handb. Chem. Phys.* (1992).

122. Verdier, S. *et al.* XPS Study on Al2O3- and AlPO4-Coated LiCoO2 Cathode Material for High-Capacity Li Ion Batteries. *J. Electrochem. Soc.* **154,** A1088–A1099 (2007).

123. Moulder, J. F. *Handbook of X-ray Photoelectron Spectroscopy: A Reference Book of Standard Spectra for Identification and Interpretation of XPS Data*. (Physical Electronics Division, Perkin-Elmer Corporation, 1992).

124. Raïssi, M. *et al.* Interfacial solid phase reactions in cobalt/aluminum oxide/silicon(001) system. *Thin Solid Films* **518,** 5992–5994 (2010).

125. D. Jiles. Introduction to Magnetism and Magnetic Materials, Third Edition. *CRC Press* (2015).

126. Glijer, P., Sin, K., Sivertsen, J. M. & Judy, J. H. Correlation of structural defects and magnetic properties in CoCrPt/Cr and CoCrTaPt/Cr thin films for ultra high density magnetic recording media. *Scr. Metall. Mater.* **33,** 1585–1592 (1995).

127. Si, W. *et al.* Deterioration of the coercivity due to the diffusion induced interface layer in hard/soft multilayers. *Sci. Rep.* **5,** 16212 (2015).

128. Gregg, J. F. *et al.* Giant Magnetoresistive Effects in a Single Element Magnetic Thin Film. *Phys. Rev. Lett.* **77,** 1580–1583 (1996).

129. Oleinik, I. I., Tsymbal, E. Y. & Pettifor, D. G. Structural and electronic properties of Co/Al2O3/Co magnetic tunnel junction from first principles. *Phys. Rev. B* **62,** 3952–3959 (2000).

130. Yuasa, S. *et al.* Giant tunneling magnetoresistance in fully epitaxial body-centered-cubic Co/MgO/Fe magnetic tunnel junctions. *Appl. Phys. Lett.* **87,** 222508 (2005).

131. Yuasa, S., Fukushima, A., Kubota, H., Suzuki, Y. & Ando, K. Giant tunneling

magnetoresistance up to 410% at room temperature in fully epitaxial Co⁄MgO⁄Co magnetic tunnel junctions with bcc Co(001) electrodes. *Appl. Phys. Lett.* **89,** 42505 (2006).

132. Carvello, B. *et al.* Sizable room-temperature magnetoresistance in cobalt based magnetic tunnel junctions with out-of-plane anisotropy. *Appl. Phys. Lett.* **92,** 102508 (2008).

133. Yuasa, S., Nagahama, T., Fukushima, A., Suzuki, Y. & Ando, K. Giant room-temperature magnetoresistance in single-crystal Fe/MgO/Fe magnetic tunnel junctions. *Nat. Mater.* **3,** 868–871 (2004).

134. Yang, H., Yang, S.-H. & Parkin, S. The role of Mg interface layer in MgO magnetic tunnel junctions with CoFe and CoFeB electrodes. *AIP Adv.* **2,** 12150 (2012).

135. Peng, S. *et al.* Giant interfacial perpendicular magnetic anisotropy in MgO/CoFe/capping layer structures. *Appl. Phys. Lett.* **110,** 72403 (2017).

136. Nistor, L. E., Rodmacq, B., Auffret, S. & Dieny, B. Pt/Co/oxide and oxide/Co/Pt electrodes for perpendicular magnetic tunnel junctions. *Appl. Phys. Lett.* **94,** 12512 (2009).

137. Vermeulen, B. F. *et al.* Perpendicular magnetic anisotropy of CoFeB\Ta bilayers on ALD HfO2. *AIP Adv.* **7,** 55933 (2017).

138. Miyazaki, T. & Tezuka, N. Giant magnetic tunneling effect in Fe/Al2O3/Fe junction. *J. Magn. Magn. Mater.* **139,** L231–L234 (1995).

139. Oleinik, I. I., Tsymbal, E. Y. & Pettifor, D. G. Atomic and electronic structure of Co/SrTiO3/Co magnetic tunnel junctions. *Phys. Rev. B* **65,** 20401 (2001).

140. Velev, J. P. *et al.* Negative Spin Polarization and Large Tunneling Magnetoresistance in Epitaxial Co/SrTiO3/Co Magnetic Tunnel Junctions. *Phys. Rev. Lett.* **95,** 216601 (2005).

141. Chappert, C. & Bruno, P. Magnetic anisotropy in metallic ultrathin films and related experiments on cobalt films (invited). *J. Appl. Phys.* **64,** 5736–5741 (1988).

142. Teresa, J. M. D. *et al.* Role of Metal-Oxide Interface in Determining the Spin Polarization of Magnetic Tunnel Junctions. *Science* **286,** 507–509 (1999).

143. Berger, A., Linke, U. & Oepen, H. P. Symmetry-induced uniaxial anisotropy in ultrathin epitaxial cobalt films grown on Cu(1 1 13). *Phys. Rev. Lett.* **68,** 839–842 (1992).

144. Chuang, C. *et al.* Thickness dependent reactivity and coercivity for ultrathin Co/Si(111) films. *Thin Solid Films* **519,** 8371–8374 (2011).

145. de Miguel, J. J. *et al.* Influence of the growth conditions on the magnetic

properties of fcc cobalt films: from monolayers to superlattices. *J. Magn. Magn. Mater.* **93,** 1–9 (1991).

146. Hehn, M., Padovani, S., Ounadjela, K. & Bucher, J. P. Nanoscale magnetic domain structures in epitaxial cobalt films. *Phys. Rev. B* **54,** 3428–3433 (1996).

147. Kief, M. T., Mankey, G. J. & Willis, R. F. Micromagnetic properties of ultrathin cobalt films. *J. Appl. Phys.* **69,** 5000–5002 (1991).

148. Kisielewski, M. *et al.* Magnetic ordering in ultrathin cobalt film covered by an overlayer of noble metals. *J. Appl. Phys.* **93,** 7628–7630 (2003).

149. Kisielewski, M., Maziewski, A., Tekielak, M., Wawro, A. & Baczewski, L. T. New Possibilities for Tuning Ultrathin Cobalt Film Magnetic Properties by a Noble Metal Overlayer. *Phys. Rev. Lett.* **89,** 87203 (2002).

150. Schneider, C. M. *et al.* Curie temperature of ultrathin films of fcc-cobalt epitaxially grown on atomically flat Cu(100) surfaces. *Phys. Rev. Lett.* **64,** 1059–1062 (1990).

151. Speckmann, M., Oepen, H. P. & Ibach, H. Magnetic Domain Structures in Ultrathin Co/Au(111): On the Influence of Film Morphology. *Phys. Rev. Lett.* **75,** 2035–2038 (1995).

152. Mantovan, R. *et al.* Atomic Layer Deposition of Magnetic Thin Films. *Acta Phys. Pol. A* **6,** 1271–1280 (2007).

153. Geissler, A., He, M., Benoit, J.-M. & Petit, P. Effect of Hydrogen Pressure on the Size of Nickel Nanoparticles Formed during Dewetting and Reduction of Thin Nickel Films. *J. Phys. Chem. C* **114,** 89–92 (2010).

154. Sangiorgi, R., Muolo, M. L., Chatain, D. & Eustathopoulos, N. Wettability and Work of Adhesion of Nonreactive Liquid Metals on Silica. *J. Am. Ceram. Soc.* **71,** 742–748

155. Chatain, D., Rivollet, I. & Eustathopoulos, N. Adhésion thermodynamique dans les systèmes non-réactifs métal liquide-alumine. *J. Chim. Phys.* **83,** 561–567 (1986).

156. Gutshall, P. L. & Gross, G. E. Cleavage Surface Energy of NaCl and MgO in Vacuum. *J. Appl. Phys.* **36,** 2459–2460 (1965).

157. Herzer, G. Grain size dependence of coercivity and permeability in average ferromagnets. *IEEE Trans. Magn.* **26,** 1397–1402 (1990).

158. Hou, C., Xu, Q., Yin, L. & Hu, X. Metal–organic framework templated synthesis of Co3O4 nanoparticles for direct glucose and H2O2 detection. *Analyst* **137,** 5803–5808 (2012).

159. Parkin, S. *et al.* Magnetically engineered spintronic sensors and memory. *Proc. IEEE* **91,** 661–680 (2003).

160. Palacios, M., García, O. & Rodríguez-Hernández, J. Constructing Robust and Functional Micropatterns on Polystyrene Surfaces by Using Deep UV Irradiation. *Langmuir* **29,** 2756–2763 (2013).

161. Anderson, G., Huai, Y. & Miloslawsky, L. CoFe/IrMn exchange biased top, bottom, and dual spin valves. *J. Appl. Phys.* **87,** 6989–6991 (2000).

162. Mizunuma, K. *et al.* MgO barrier-perpendicular magnetic tunnel junctions with CoFe/Pd multilayers and ferromagnetic insertion layers. *Appl. Phys. Lett.* **95,** 232516 (2009).

163. Monso, S. *et al.* Crossover from in-plane to perpendicular anisotropy in Pt/CoFe/AlOx sandwiches as a function of Al oxidation: A very accurate control of the oxidation of tunnel barriers. *Appl. Phys. Lett.* **80,** 4157–4159 (2002).

164. Osaka, T., Yokoshima, T., Shiga, D., Imai, K. & Takashima, K. A High Moment CoFe Soft Magnetic Thin Film Prepared by Electrodeposition. *Electrochem. Solid-State Lett.* **6,** C53–C55 (2003).

165. Pakala, M., Huai, Y., Anderson, G. & Miloslavsky, L. Effect of underlayer roughness, grain size, and crystal texture on exchange coupled IrMn/CoFe thin films. *J. Appl. Phys.* **87,** 6653–6655 (2000).

166. Sun, M., Medina, J. A., Sasaki, K. Y. & Jiang, M. Method and system for providing high magnetic flux saturation CoFe films. (2014).

167. Wang, W., Sukegawa, H., Shan, R., Mitani, S. & Inomata, K. Giant tunneling magnetoresistance up to 330% at room temperature in sputter deposited Co2FeAl/MgO/CoFe magnetic tunnel junctions. *Appl. Phys. Lett.* **95,** 182502 (2009).

168. Zhou, X. W., Johnson, R. A. & Wadley, H. N. G. Misfit-energy-increasing dislocations in vapor-deposited CoFe/NiFe multilayers. *Phys. Rev. B* **69,** 144113 (2004).

169. Hylton, T. L., Coffey, K. R., Parker, M. A. & Howard, J. K. Giant Magnetoresistance at Low Fields in Discontinuous NiFe-Ag Multilayer Thin Films. *Science* **261,** 1021–1024 (1993).

170. Li, J., Zhao, C., Feng, C., Zhou, Z. & Yu, G. Impact of interface manipulation of oxide on electrical transport properties and low-frequency noise in MgO/NiFe/MgO heterojunctions. *AIP Adv.* **5,** 87139 (2015).

171. Nan, T. *et al.* Comparison of spin-orbit torques and spin pumping across NiFe/Pt and NiFe/Cu/Pt interfaces. *Phys. Rev. B* **91,** 214416 (2015).

172. Sitthisa, S., An, W. & Resasco, D. E. Selective conversion of furfural to methylfuran over silica-supported NiFe bimetallic catalysts. *J. Catal.* **284,** 90–101 (2011).

173. Dionigi, F. & Strasser, P. NiFe-Based (Oxy)hydroxide Catalysts for Oxygen Evolution Reaction in Non-Acidic Electrolytes. *Adv. Energy Mater.* **6,** 1600621 (2016).

174. Gong, M. & Dai, H. A mini review of NiFe-based materials as highly active oxygen evolution reaction electrocatalysts. *Nano Res.* **8,** 23–39 (2015).

175. Martin, M.-B. *et al.* Sub-nanometer Atomic Layer Deposition for Spintronics in Magnetic Tunnel Junctions Based on Graphene Spin-Filtering Membranes. *ACS Nano* **8,** 7890–7895 (2014).

176. Burton, B. B., Goldstein, D. N. & George, S. M. Atomic Layer Deposition of MgO Using Bis(ethylcyclopentadienyl)magnesium and H2O. *J. Phys. Chem. C* **113,** 1939–1946 (2009).

177. Ryu, S. W., Song, J.-G., Kim, H. G., Kim, H. & Lee, H.-B.-R. Interlayer-assisted atomic layer deposition of MgO as a magnetic tunneling junction insulators. *J. Alloys Compd.* **747,** 505–510 (2018).

178. Groner, M. D., Fabreguette, F. H., Elam, J. W. & George, S. M. Low-Temperature Al2O3 Atomic Layer Deposition. *Chem. Mater.* **16,** 639–645 (2004).

179. Groner, M. D., Elam, J. W., Fabreguette, F. H. & George, S. M. Electrical characterization of thin Al2O3 films grown by atomic layer deposition on silicon and various metal substrates. *Thin Solid Films* **413,** 186–197 (2002).

180. Liao, W. & Ekerdt, J. G. Ru nucleation and thin film smoothness improvement with ammonia during chemical vapor deposition. *J. Vac. Sci. Technol. A* **34,** 31508 (2016).